A study of electron Bernstein wave for diagnosis and heating of spherical tokamak plasmas

Syun'ichi SHIRAIWA

A dissertation submitted in partial fulfillment of the

requirement for the degree of

Doctor of Philosophy

ii

Abstract

The electron Bernstein wave (EBW) is an electrostatic plasma wave that is considered as a promising candidate for diagnosis, heating, and current drive of overdense ($\omega_{\mathrm{pe}} \geq \Omega_{\mathrm{ce}}$) spherical tokamak (ST) plasmas, where ω_{pe} is the electron plasma angular frequency and Ω_{ce} is the electron cyclotron angular frequency. Two major achievements in EBW research, one for plasma temperature measurement and the other for plasma heating, are reported in this thesis. The experiments were performed on a newly constructed spherical tokamak, TST-2. Significant improvements on plasma parameters were achieved on TST-2, compared to the previous device TST-M. Plasmas with plasma current $I_{\mathrm{p}} \sim 100\,\mathrm{kA}$, electron temperature $T_{\mathrm{e}} = 200\text{–}400\,\mathrm{eV}$, ion temperature $T_{\mathrm{i}} \sim 100\,\mathrm{eV}$, line-averaged electron density $\bar{n}_{\mathrm{e}} \sim 1 \times 10^{19}\,\mathrm{m}^{-3}$, and energy confinement time $\tau_{\mathrm{e}} = 1.5\text{–}3\,\mathrm{ms}$ were produced routinely, enabling radio-frequency (RF) wave experiments including EBW research. In order to excite or detect the electrostatic EBW using an antenna located outside the plasma, mode-conversion (MC) between the EBW and an electromagnetic wave is necessary. The MC scenario used in these experiments is the X-mode injection (or detection) propagating perpendicularly to the magnetic surface on the low magnetic field side (outboard side of the torus). In an ST plasma, the upper hybrid resonance (UHR), where the electromagnetic X-mode connects to the EBW, forms a cutoff-resonance-cutoff triplet, and nearly 100% MC is predicted if a suitable density scale length L_{n} is formed near the UHR layer. A novel T_{e} diagnostic, the radio-reflectometer, was developed. The radio-reflectometer measures the density profile in the MC region and the profile of radiation temperature, T_{rad}, simultaneously. The radiation temperature is the intensity of emission expressed by the equivalent black body temperature. The T_{rad} profile was obtained using emission in the frequency range of $5 - 16\,\mathrm{GHz}$, corresponding to the fundamental to the 3rd harmonic EBW emission. T_{e} was evaluated from T_{rad} using a theoretical MC efficiency calculated using the measured density profile. A central T_{e} of $200 - 300\,\mathrm{eV}$ and a monotonic T_{e} profile were obtained. The measured core T_{e} was consistent with the results obtained from other diagnostics, demonstrating

the radio-reflectometer as a "stand-alone" T_e diagnostic. In order to conduct EBW heating experiments, TST-2 was temporarily moved to Kasuga Campus of Kyushu University, where 200 kW microwave power at 8.2 GHz was available. A local limiter was used to control the density profile in the MC region. A fairly good antenna-plasma coupling was observed, and up to 140 kW of microwave power was injected successfully. A clear increase of the stored energy at RF turn-on was observed, and a heating efficiency of over 50 % was achieved in a high density discharge. An increase of X-ray emission in the energy range of $h\nu \geq 1$ keV was observed, indicating generation of high energy electrons by EBW. Soft X-ray emission profile measurements by PIN diode cameras showed that the soft X-ray emission increase was concentrated in the plasma core region, where EBW is expected to be absorbed based on a ray-tracing analysis. In lower density discharges, the heating efficiency was lower, indicating a poorer MC efficiency. A 1-D full-wave calculation of MC showed that the decrease of the MC efficiency can be explained by the radial stretch of the cutoff-resonance-cutoff triplet. These results are consistent with the picture that the EBW generated by MC at the triplet propagates towards the plasma core region and is absorbed by electron cyclotron damping.

Acknowledgment

Many hard working individuals including researchers, technical stuffs, graduate students, and support stuffs have supported TST-2 and TST-2@K experiments. I would like to acknowledge all the people who helped me in conducting this thesis research, and I apologize that I do not have sufficient space to mention all of them here.

I am grateful to Prof. Y. Takase for his overall guide in conducting this thesis research. Building a new plasma device from scratch gave me a chance to learn both scientific and engineering aspects those are usually out of sights of fusion researchers. His expertise in RF waves in plasmas was helpful to develop a convincing explanation of the experimental results. Prof. K. Hanada at Kyushu University provided an opportunity to perform the EBW heating experiment. Without his initiative for relocating TST-2 to Kyushu University, which we first discussed at the annual meeting of JPSF of 2002, it would been impossible to conceive the conduct of the heating experiment. I am grateful to Dr. G. Taylor, Dr. P. Efthimion, and Dr. B. Jones for opportunity of participating the EBW receiving experiments carried out on CDX-U.

I would like to thank Prof. H. Zushi, Prof. K. Nakamura, Prof. K. Sato, Associate Prof. Sakamoto, Associate Prof. Idei, and Dr. M. Hasegawa at Kyushu University for their help in conducting the EBW heating experiments. I would like to thank Prof. N. Nishino at Hiroshima University for fast camera observation and to Prof. O. Mitarai for useful discussion on plasma start-up. Member of Takase Laboratory are all, more or less, involved the construction of TST-2 and the EBW research. In particular, I appreciate Associated Prof. A. Ejiri's contribution to the construction TST-2 and the preparation of interferometers. I am grateful to Dr. Y. Nagashima for his collaboration in radio-reflectometer experiments and to Dr. T. Yamada and Dr. H. Kasahara for their efforts in preparing TST-2 control systems and diagnostics.

I would like to thank peoples who have paved the load towards the present thesis. Retired Prof. H. Toyama provided me fundamentals that are required

Contents

Chapter 1

Thesis guideline and goal

The Spherical Tokamak (ST) [1] is a tokamak with low aspect ratio (R/a, where R and a are the major and the minor radii, respectively). ST has been attracting coniderable attention during the past decade. This is largely because ST has an advantage of achieving stable high β (defined as the ratio of plasma pressure to magnetic pressure) plasmas compared to conventional aspect ratio tokamaks and stellarators. This is an attractive property for realizing an economically competitive fusion reactor.

A unique feature of ST plasmas is that they are highly overdense in general, namely, $\omega_{\mathrm{pe}}^2/\Omega_{\mathrm{ce}}^2 = 10 \sim 100$, while $\omega_{\mathrm{pe}}^2/\Omega_{\mathrm{ce}}^2 \leq 1$ in conventional tokamak and stellarator plasmas, where ω_{pe} and Ω_{ce} are electron plasma and cyclotron angular frequencies, respectively. In overdense plasmas, waves behave quite differently from those in underdense plasmas. Waves commonly used for diagnosis, heating, and current drive of fusion plasmas, such as the electron cyclotron wave and the lower hybrid wave have poor accessibility to the core of overdense plasmas. Inevitably, alternative techniques that rely on waves which are not so frequently used before must be developed. The electron Bernstein wave (EBW) [2] and the high harmonic fast wave (HHFW) [3] are such alternatives. The EBW is anticipated to play a similar role to the electron cyclotron wave used in underdense plasmas [4, 5, 6]. Its emission is considered blackbody and is suitable for a local electron temperature measurement. If the EBW could be excited by an external microwave source, it can provide efficient methods of plasma heating and current drive.

The EBW is not so attractive in underdense plasmas, and only a limited number of experiments has been conducted. Because of the following relationship,

$$k^2 \rho_{\mathrm{e}}^2 = \frac{\omega_{\mathrm{pe}}^2}{\Omega_{\mathrm{ce}}^2} k^2 \lambda_{\mathrm{D}}^2, \tag{1.1}$$

where k is the wave vector, λ_{D} is the Debye length, and ρ_{e} is the Larmor

radius of thermal electrons and $k^2\lambda_\mathrm{D}^2 \ll 1$, the region where the short wave-length EBW can exist is very restricted in underdense plasmas.

It is difficult to excite the EBW directly by external injection of an electromagnetic wave, since the EBW is an electrostatic wave and its wave vector is parallel to its electric field. Hence, a mode-conversion (MC) from the X-mode to the EBW that occurs near the upper hybrid resonance (UHR) layer is used to excite the EBW. In fusion plasma research, two MC scenarios have been proposed and demonstrated in plasmas with $\omega_\mathrm{pe}^2/\omega_\mathrm{ce}^2 \sim 1$. Heating and current drive by the high magnetic field side X-mode launch (X-B) MC has been demonstrated in conventional tokamaks [7, 8]. The second MC scenario (O-X-B) was first demonstrated on the Wendelstein 7-AS stellarator [9, 10]. However, the X-B scenario from the high field side (small major radius side) is not usable in ST because a cutoff layer, called the left-hand cutoff, appears on the high field side, when $\omega_\mathrm{pe}^2/\omega_\mathrm{ce}^2$ exceeds unity significantly. The O-X-B scenario seems to be applicable in ST, but is more difficult than in a stellarator, since the magnetic field configuration is not determined by external coils alone.

Using the EBW in ST plasmas is, to the author's knowledge, first proposed for a diagnostic purpose by Efthimion [11] in 1998. Efthimion's paper pointed out an important new MC scenario suitable for ST, a possiblity of MC between the EBW and the X-mode propagating perpendicularly to the magnetic field on the low field side (large major radius side). In a highly overdense plasma, the X-mode electromagnetic wave launched from the low magnetic field side of the torus encounters a triplet consisting of left-hand cutoff, UHR, and right-hand cutoff. The existence of a cutoff layer on the high density side of the resonance changes the MC efficiency drastically from the case of a doublet consisting of UHR and right-hand cutoff. Though MC through this process was investigated in the 1980's [12, 13], a corrected calculation of the MC efficiency was not performed and the mode-converted EBW was reported to be absorbed near the UHR layer, probably because of the low temperature. The enhancement of the MC efficiency for the case of triplet was first pointed out in an analysis of an ion cyclotron heating experiment [14]. If a specific condition for the density scale length near the UHR layer is satisfied, a nearly 100% MC efficiency is predicted. The present thesis is largely motivated by questions arising for such a scenario, including

- Can the condition for the density scale length be achieved easily? What happens if the condition is not satisfied completely?

- Can the reverse process be used for plasma heating and current drive?

To address these issues experimentally, a series of experiments were con-

ducted to receive the EBW and to heat ST plasmas by the EBW. However, the road to these experiments was not paved well at the beginning. The ST device at the University of Tokyo at that time was TST-M (Tokyo Spherical Tokamak - Modified) [15] whose plasma parameters were not sufficient for either diagnostic development or plasma heating. Furthermore, a high power microwave generator to be used in a heating experiment did not exist. The activity of replacing TST-M by a new device named TST-2 [16, 17], which can produce a suitable plasma for radio-frequency wave experiments, was initiated. The design and construction of TST-2, and the development of operating scenarios occupy the first half of the thesis.

A low power EBW receiving experiment was carried out first. A novel diagnostic tool named radio-reflectometer was developed to measure the MC efficiency and the intensity of EBW emission simultaneously [18]. The author also participated in an EBW receiving experiment carried out on CDX-U, where the idea of controlling the MC efficiency by a local limiter was tested [19]. Whereas several theoretical considerations of EBW heating in ST have been reported, no progress was made in high power heating experiments while these receiving experiments were carried out, and an experimental demonstration was highly desired. TST-2 was temporarily moved to Kyushu University where 8.2 GHz 200 kW microwave power was available. The same low field side perpendicular X-mode injection scenario was employed. A local limiter improved to withstand the high-power plasma heating experiment was used in this experiment. This experiment provided the first demonstration of heating of an ST plasma by the EBW [20, 21].

This study is specifically oriented to the application of a wave in the electron cyclotron frequency range ($\sim$ GHz) to fusion plasma. However, the process of MC itself can occur when a wave propagates in any frequency range and in any non-uniform medium. In fusion plasmas, conversion to the ion Bernstein wave from the fast wave in the ion cyclotron frequency range ($\sim$ MHz) is actively studied. MC is also seen in magnetized astrophysical plasmas, such as radio wave emission from Jupiter, in the Earth's magnetosphere, and possibly in the solar corona.

This thesis is organized as follows: In chapter 2, review of ST is presented. In chapter 3, EBW physics is revisited. Chapter 4 is devoted to the design and construction of TST-2. Chapter 5 describes the diagnostic tools and the heating system. Chapter 6 presents and discusses the experimental results. Chapter 7 summarizes the results and perspectives for future research.

Chapter 2

Spherical Tokamak

In this chapter, the spherical tokamak (ST) concept is described. Proposal of the ST was deeply related with the advanced tokamak concept to improve the tokamak to satisfy high confinement, high stability, and steady state simultaneously. After description of the background, the status of ST research at the time this work was initiated is reviewed. Progress made since then is addressed separately in the last section.

2.1   Magnetic fusion energy

Energy generated by fusion reactions of light atoms has been considered a possible source of virtually inexhaustible energy. Such an idea was first proposed soon after World War II. Though the fusion reaction itself is the same process as that occurring in a hydrogen bomb, it turned out to be extremely challenging to realize it in a controlled manner. To achieve fusion reaction, fuel atoms need to be heated to a very high temperature at high density. Even the D-T reaction, $D + T \rightarrow He^4$ (3.52Mev) + n (14.06MeV), which has a sufficiently large reaction cross section at the lowest temperature among such reactions, requires a temperature of ~ 10 keV. At such temperatures the fuel gas is completely ionized and is in the plasma state.

   In the presence of a magnetic field, a charged particle follows a helical trajectory with its axis along the magnetic field. This property can be used to confine a high temperature plasma. This scheme is called magnetic fusion energy (MFE). When a magnetic field line intersects a solid material, energetic plasma particles can come in direct contact with the material and the surface would evaporate. To avoid such a situation, connecting one end of the field line to the other end was devised. In the tokamak, the plasma is confined in a toroidal (torus shaped) magnetic field configuration.
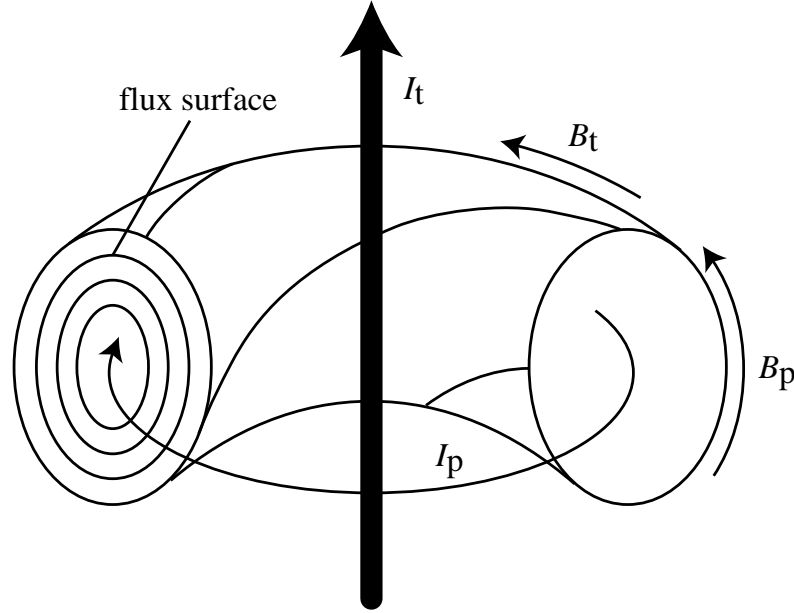
Figure 2.1: Schematic of the tokamak.

2.2   Tokamak

Figure 2.1 shows the tokamak configuration schematically. An external current along the axis of symmetry, I_t, produces a strong magnetic field in the toroidal direction B_t. Plasma current I_p is driven in the plasma either by externally means or by the plasma itself, and produces the poloidal magnetic field B_p. The combination of B_t and B_p produces magnetic field lines confined on a toroidal surface called the flux surface. The tokamak configuration consists of a set of nested flux surfaces.

Among various fusion reactor concepts, the tokamak [22] is considered to be the closest to realizing a fusion power plant. To demonstrate the scientific and technical feasibility of fusion power, the ITER (International Thermonuclear Experimental Reactor) Project was initiated in 1985 by an agreement signed by M. S. Gorbachev and R. W. Reagan. After over 20 years of design activity, the site for constructing ITER was decided in 2006, and its construction is about to start.

With the development of fusion energy as the ultimate goal, every fusion program including MFE must address the issue of minimizing the cost of electricity (CoE). To reduce CoE, high beta, good confinement, and steady-
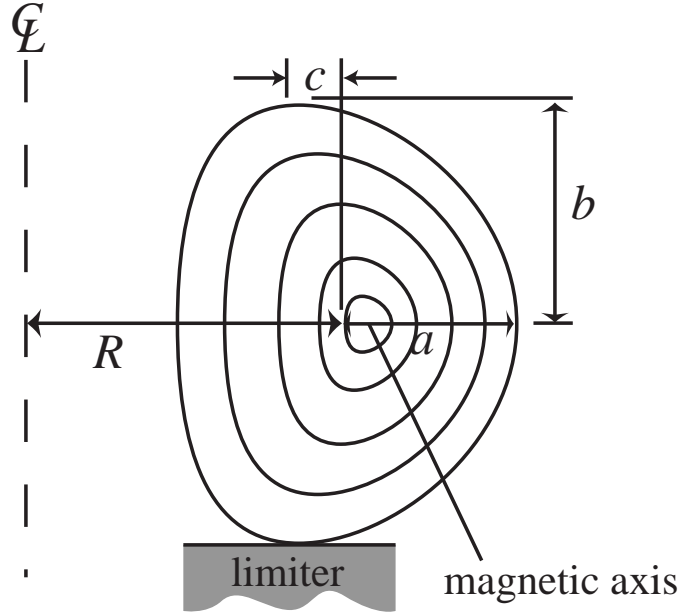
Figure 2.2: Geometrical parameters of the tokamak.

state operation must be satisfied simultaneously. These are the key issues in tokamak research. After introducing geometrical parameters of the tokamak in the next subsection, these issues are considered before discussing the spherical tokamak.

2.2.1 Geometrical parameters

Geometrical parameters characterizing the tokamak configuration are defined in Fig. 2.2. The tokamak is an axi-symmetric toroidal configuration. The magnetic axis is the line corresponding to the limit of innermost flux surface, and is shifted outward from the geometrical axis (R in Fig. 2.2) by the Shafranov shift. The last closed flux surface (LCFS) is the outermost closed flux surface of confined plasma, outside which magnetic field lines intersect a material wall.

The major radius R is the distance from the symmetry axis to the geometric axis. The minor raidus a is the horizontal distance from the geometric axis to the LCFS. The ratio of R to a is called the aspect ratio ($A \equiv R/a$). In conventional tokamaks A is typically in the range 2.5–4. The cross section of a tokamak plasma is usually vertically elongated and shifted towards the symmetry axis as shown in Fig. 2.2. Using the symbols defined in the figure,

the elongation $\kappa \equiv b/a$ and the triangularity $\delta \equiv c/a$ are defined.

2.2.2 Beta

The plasma beta β is defined as the ratio of the plasma kinetic pressure to the magnetic pressure,

$$\beta = \frac{2\mu_0 p}{B^2}, \tag{2.1}$$

where p is the plasma pressure and B is the magnetic field strength. Since both plasma pressure and magnetic field strength have spatial dependences, the toroidal beta, defined as $\beta_t = 2\mu_0 \langle p \rangle / B_{t0}^2$, where $\langle p \rangle$ is the volume averaged plasma pressure and B_{t0} is the externally applied toroidal field at the geometrical axis, is often used. High β operation is required for economical fusion power plant. The fusion power density P_w is proportional to $n^2 \langle \sigma v \rangle Q$, where n is the fuel ion density, $\langle \sigma v \rangle$ is the fusion reaction cross section averaged over the velocity distribution function, and Q is the energy produced by a single fusion reaction. Since $\langle \sigma v \rangle$ for D-T reaction near optimum temperature is approximately proportional to T_i^2, P_w is proportional to $\beta_t^2 B_{t0}^4$. Since higher B_{t0} devices are massive and expensive, it is advantageous to achieve the required P_w at higher β_t and lower B_{t0}.

The highest β achievable in a tokamak is limited by various instabilities such as the kink-ballooning mode, the neoclassical tearing mode [23], and the resistive wall mode [24]. Theoretical prediction of the achievable β in a realistic tokamak geometry relies on numerical analysis. The most well-known is the analysis of the kink-ballooning mode with low toroidal mode numbers performed for INTOR and JET by Troyon in 1984 [25]. According to this analysis, the upper limit for β_t is given by

$$\beta_c[\%] = \beta_N \frac{I_p[\mathrm{MA}]}{a[\mathrm{m}] B_{t0}[\mathrm{T}]}, \tag{2.2}$$

where β_N is the normalized beta, and I_p is the plasma current in MA. This is called the Troyon limit. This form of beta limit has been confirmed in a number of tokamak experiments (for example, $\beta_N \sim 3.5$ for tokamaks with $A \sim 3$ [26]). More recently the achievement of $\beta_N \sim 7.2$ is reported from the National Spherical Torus Experiment (NSTX) [27].

2.2.3 Confinement time

To achieve the condition required for fusion, it is necessary to confine the energy injected into the plasma for a sufficiently long time. The simplest way to characterize confinement is by the global energy confinement time,

defined as $\tau_{\mathrm{E}} \equiv W_{\mathrm{K}}/P_{\mathrm{input}}$, where W_{K} is the energy stored in the plasma, and P_{input} is the input power to the plasma.

Processes that contribute to energy loss from the plasma include thermal conduction, convection, radiation, and charge exchange. Transport by Coulomb collisions in the tokamak geometry is described by the neoclassical theory (see for example Ref. [28, 29]). However, the conduction loss observed experimentally is usually larger than that predicted based on neoclassical theory. The enhanced energy loss is attributed to transport caused by plasma turbulence, and is called the anomalous transport [30]. Suppression of turbulence and anomalous transport is an important subject in tokamak research. In the high confinement mode (H-mode) [31], confinement improves due to suppression of plasma turbulence and associated transport at the plasma edge. Formation of the internal transport barrier (ITB) improves confinement by suppressing turbulence inside the plasma [32]. It is known that improved confinement is attributed to the suppression of turbulence by the $E \times B$ shear flow [33, 34]. While theory fails to predict transport quantitatively, efforts are made to relate the measured energy confinement to gross plasma parameters in the form of empirical scaling laws [35, 36]. Such scaling laws are used to predict the energy confinement time in designing new devices such as ITER.

2.2.4 Steady state operation

Originally, the tokamak was considered to be a pulsed device since the plasma current was driven by induction using the central solenoid. Resistive heating of the plasma by the current flowing the plasma is called Ohmic heating. Ohmic heating is effective only when the plasma temperature is relatively low, less than 2–3 keV, since the plasma resistivity decreases as $T^{-3/2}$. To achieve fusion reactions, additional heating up to 10–20 keV is necessary. Plasma heating methods using external injection of neutral beams (NB) or large amplitude radio-frequency (RF) waves have been developed. Such techniques can also be used to drive the plasma current. This is accomplished by deforming the velocity distribution function of the plasma towards one direction. This is called current drive (CD). Progress in the development of CD techniques has made steady state tokamak operation a realistic option. Achieving steady state operation without sacrificing beta or confinement is a challenging topic, and is called advanced tokamak (AT).

Since providing sufficient non-inductive current drive power is expensive, most of the plasma current must be driven by the self-generated bootstrap current [37]. The bootstrap current is proportional to $(\partial p/\partial r)/B_{\mathrm{p}}$, where B_{p} is the poloidal magnetic field. Since B_{p} is generated by the plasma cur-

rent, increasing the bootstrap current is contradictory to increasing β, if β_N were constant. In AT experiments, one aims at achieving high β, high confinement, and high bootstrap current fraction simultaneously. This requires improvement in β_N.

2.3   Spherical Tokamak

The spherical tokamak (ST) is a tokamak with very low aspect ratio ($A < 2$). Though experimental reports of low aspect ratio tokamak can be traced back to 1970, the prevalence of ST research started from the contemplation of advantageous features of the ST by Peng and Strickler in the mid 1980s [1]. The ST concept was proposed based on motivation of achieving the same goal as AT research, namely simultaneous realization of steady-state, high confinement, and high β. When construction of TST-2 started at the end of 1998, ST research was making a transition from the initial phase of characterizing the ST plasma on a small scale to proof-of-principle experiments on a medium scale. Construction activities of MAST [38] and NSTX [39], which are ST devices that are three times larger than TST-2, were being completed. More reactor-relavent research topics including identification and improvement of the beta limit, heating and current drive by NB and RF injection, and high energy particle physics were attracting interest. It is convenient to separate the chronicle of ST research at that time.

2.4   Early perspectives of ST

The merit of reducing the aspect ratio for achieving high β was shown intuitively in Ref. [1]. Troyon's scaling (Eq. 2.2), implies that β can be increased by increasing I_p or decreaseing B_t0. However, MHD stability imposes a limit of the maximum plasma current for a given toroidal field. More precisely, there is a minimum limit for the edge safety factor q_a imposed by stability. The safety factor is a parameter which defines the topology of a flux surface. If a field line turns three times in the toroidal direction while it turns once around the poloidal circumference, the safety factor of that flux surface is three. The most fundamental limit is known as the Kruskal-Shafranov limit for $n = 1$, $m = 1$ ideal kink instability, $q_\mathrm{a} > 1$. Consideration of other modes such as the internal mode, the tearing mode, and the resistive mode, the limit become more stringent ($q_\mathrm{a} > 2 \sim 3$).

The edge safety factor of a tokamak with arbitrary aspect ratio and elon-

gation is approximately given by

$$q_{\mathrm{a}} = \frac{2\pi a B_{\mathrm{t0}}}{\mu_0 I_{\mathrm{p}}} \frac{1.22\epsilon - 0.68\epsilon^2}{(1-\epsilon^2)^2} \frac{1+\kappa^2}{2}, \qquad (2.3)$$

where ϵ is the inverse aspect ratio $(1/A)$. Equation 2.3 indicates a tremendous advantage of low aspect ratio in increasing q_{a}. In addition, as the aspect ratio decreases, the plasma tends to elongate in the vertical direction naturally. This is because the plasma feels the poloidal field created by the plasma current flowing on the opposite side of torus more strongly as $A \to 1$. This feature is called natural elongation and contributes to increasing β_{c}. Figure 2.3 shows the dependence of β_{c} on the aspect ratio, including the effect of natural elongation. A significant increase of β_{c} is predicted, when the aspect ratio is reduced below 2. In Ref. [1], it is pointed out that other characteristics of ST plasmas, such as near-omnigeneity and short length of magnetic field in the bad curvature region imply improved MHD stability.

Following the intuitive discussion of Ref. [1], the maximum achievable beta of ST plasmas were evaluated in more detail by several authors. A wide range of equilibrium with β_{t} exceeding 20% at $A = 5/3$ that is stable for low n (n =1–3) modes, the $n = \infty$ ballooning mode and Mercier instability was reported [40]. Stability against kinetic instabilities were also analyzed using a comprehensive toroidal eigenvalue code with realistic equilibria. It was reported that the reduction of "bad" magnetic curvature region contributes to stabilization of both electrostatic and electromagnetic high-n instabilities at sufficiently small aspect ratio [41].

Experimentally, START (Small Tight Aspect Ratio Tokamak) was the only experiment that tested the high beta stability of the ST plasma. START demonstrated that over $\beta_{\mathrm{t}} > 30\%$ and $\beta_{\mathrm{N}} > 4$ could be sustained for several energy confinement times [42]. START experiments also showed that energy confinement of ST plasmas approximately followed the ITER98bpy1 [43] scaling, an empirical scaling law derived from experimental data obtained in conventional aspect ratio tokamaks. It was also reported that, in Ohmic discharges, the measured confinement time exceeded the neo-Alcator scaling significantly [44]. However, START was a small scale experiment with a major radius of ~ 0.3m. Though the beta surpassed the values achieved in large conventional aspect ratio tokamaks, START plasmas were not considered sufficiently collisionless, and a confirmation in larger, hotter, and less collisional STs that were being commissioned was highly desired.

Concerning steady-state operation, a stable equilibrium was found theoretically at an aspect ratio of $A = 1.4$ and an elongation of $\kappa = 3.0$, with 99.3% of plasma current provided by the plasma pressure at $\beta = 45\%$ [45]. The demonstration of steady-state operation was left to the next generation
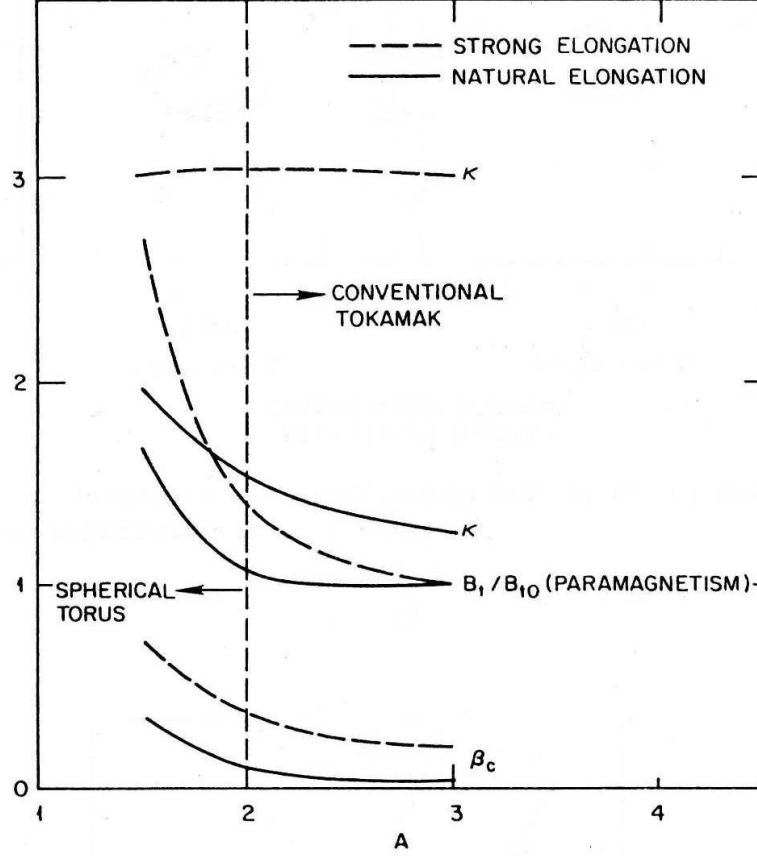
Figure 2.3: Dependence of β_c and paramagnetism (B_t/B_{t0}) on aspect ratio for strongly elongated and naturally elongated plasmas [1].

STs. Another important issue is that current drive (CD) techniques using radio frequency (RF) waves established in conventional tokamaks and stellarators are not applicable to ST plasmas. Therefore, development of a new RFCD method is required, and many approaches are being studied.

2.5 Waves in ST plasmas

2.5.1 Unique features of ST

In plasma physics, β is a measure of importance of finite temperature effects. For example, in the finite Larmor radius (FLR) expansion of the plasma dielectric tensor, the tensor elements are expanded in series of $\lambda = \frac{1}{2}k_\perp^2 \langle \rho^2 \rangle =$

$\frac{k_\perp^2 \kappa T_\perp}{m\Omega^2}$, where $k_\perp$ is the perpendicular wavenumber, $T_\perp$ is the perpendicular temperature of the species being considered, and $\Omega = eB/m$ is the cyclotron angular frequency. Recalling that the susceptibility is proportional to the number density (see Eq. 3.22, where ω_{pe}^2 is proportional to the density), the first order effect is proportional to β. A low β expansion is also used frequently in the analysis of plasma instabilities.

The result of the increased significance of finite temperature effects is that completely different waves must be used in ST plasmas. ST plasmas are generally overdense ($\omega_{pe}^2/\Omega_{ce}^2 > 1$), except at the very edge of the plasma. In overdense plasmas, plasma waves behave quite differently compared to underdense plasmas. Plasma waves commonly used in fusion plasma experiments for diagnosis, heating and current drive, such as the electron cyclotron (EC) and lower hybrid (LH) waves have severe accessibility problems. The EC wave has no access to the plasma core. Only high $n_\parallel$ LH waves satisfy the accessibility condition, but these waves are damped in the low temperature edge region, and the achievable CD efficiency is very low. In the range of ion cyclotron (IC) frequency, the fast wave can access the plasma core and is used for ICRF heating on the Globus-M spherical tokamak. However, it is noted in Ref. [3] that the fast waves with low harmonic numbers is expected to mode convert to a short wave length mode similar to the ion Benstein wave (IBW) [46] at a relatively low ion beta, and waves with $\omega \leq \Omega_{ci}$ are poorly absorbed.

2.5.2 Promising waves in ST plasmas

Two plasma waves, the high harmonic fast wave (HHFW) [3] in the intermediate frequency range between IC and LH, and the electron Bernstein wave (EBW) in the EC frequency range, are candidate waves considered for heating and current drive in high β plasmas. As mentioned in Ch. 1, EBW is anticipated to play a similar role to the electron cyclotron wave used in underdense plasmas [4, 5, 6]. Besides heating and current drive, measurement of the electron temperature using EBW emission was proposed. The status of EBW research when the construction of TST-2 started can be summarized as follows: A pioneering work on the detection of and heating by EBW was performed on the WA-7S stellarator using a plasma with $\omega_{pe}^2/\Omega_{ce}^2 \sim 1$ [9, 10]. Later demonstrations on tokamaks were also reported [7, 8], but $\omega_{pe}^2/\Omega_{ce}^2$ was still in the region near unity. No experiments on ST-like plasmas having $\omega_{pe}^2/\Omega_{ce}^2 \sim 10$–100 has been performed yet. Since EBW is the main theme of the present thesis, theoretical description and review of related work are given in more detail in the next chapter.

As for HHFW, pioneer experiments were performed on CDX-U, and an

indication of electron heating based on spectroscopic data was reported in
Ref. [47]. However, a majority of discharges exhibited only moderate core
T_e rise, with most of the heating occurring outside $r/a = 0.5$. Obviously,
a clearer result is desired and scaled-up experiments are planned in next
generation STs.

2.5.3   Plasma start-up

Plasma start-up is a field in which RF is envisaged to play an important
role. A major drawback of the ST is that it has a severe space restriction
on the inboard side, where the Ohmic heating (OH) solenoid is placed in
conventional tokamaks. Though present day STs are equipped with an OH
solenoid, it is considered impossible to accomodate an OH solenoid in the
nuclear environment of an ST reactor. Since the OH solenoid is used to start
up the plasma current, an ST reactor must seek an alternative technique for
plasma start-up which is simple and reliable.

Several methods of plasma current start-up have been demonstrated. The
methods independent of radio frequency waves are described first. START
has used a novel merging compression method [48]. Two plasmas are pro-
duced at upper and lower parts of the torus inductively by a current swing
of poloidal field coils placed inside the vacuum vessel. Two plasmas are
merged on the midplane to form a single plasma. The technique used on
TS-3 resembles that of START [49]. The difference is that TS-3 used two
sets of poloidal field coils and eight electrodes to produce spheromaks at
the upper and lower parts of the torus. When spheromaks with toroidal
fields in opposite directions are merged (counter helicity merging), a field
reversed configuration (FRC) with unity beta is produced. By applying an
external toroidal field to the FRC, ultra-high-beta ($50\% \sim 70\%$) spherical
tokamak plasmas were formed. Helicity injection [50] can be used to sustain
the plasma current by applying a bias voltage to the magnetic flux that pen-
etrates through two electrodes. Coaxial helicity injection (CHI) was used to
produce ST plasmas with plasma currents of up to $150\,\mathrm{kA}$ on HIT (Helicity
Injected Tokamak) [51]. A numerical simulation suggests that a significant
amount of volt-seconds can be provided by the vertical field coil [52]. How-
ever, a significant heating power is required to sustain the inductively driven
plasma current.

Despite these promising results, it is still questionable that these methods
can be used on an ST based reactor. Plasma generation using an electrode
discharge is always accompanied by a concern about impurity contamination.
In-vessel coils and electrodes are difficult to shield, and are definitely unfa-
vorable in a reactor. They must also be consistent with divertors for exhaust

handling, which are located at the upper and lower parts of the vacuum vessel. Implementation of CHI would make the already quite complicated vacuum vessel even more complicated.

Plasma start-up using RF has a long history of experiments on conventional aspect ratio tokamaks. Plasma start-up followed by plasma current ramp-up by a combination of electron cyclotron (EC) and lower hybrid (LH) waves was first demonstrated on the WT-2 tokamak (RF tokamak) [53], and was extended by other experiments using either ECH, LH, or both waves [54, 55, 56]. In ST, CDX-U reported a generation of a small plasma current ($\sim 1\,\mathrm{kA}$) by RF injection alone [57]. Similar experiments were also carried out on TST-2, and CDX-U results were confirmed. It is interesting to note that plasmas produced were overdense even though the injected RF is in the EC frequency range. The pressure driven current was proposed to explain this result [57], but the consideration remained qualitative. Such overdense plasmas seem to provide a suitable starting point for a target plasma to try further plasma current ramp-up by EBW current drive (EBCD). Recently, an experiment on LATE [58] achieved an order of magnitude higher plasma current ($\sim 15\,\mathrm{kA}$), but it is not claimed that EBCD was realized.

2.6 ST experiments worldwide

Encouraged by the promising results on START, various ST devices are being operated or are being constructed worldwide, as shown in Table 2.1, giving us a broader and deeper understanding of the ST plasma. Of course, it is impossible to cover the whole range of diverse ST research exhaustively. The following list is intended to introduce the recent experimental trend.

The largest scale ST experiments, MAST and NSTX, were commissioned around 2000. Plasmas produced in these two devices have major radii of $\sim 0.7\,\mathrm{m}$, minor radii of $\sim 0.5\,\mathrm{m}$, and plasma currents of $\sim 1\,\mathrm{MA}$. After successful attainments of the first plasma around 2000, both devices have been enhancing their capabilities step by step.

Concerning β and confinement, NSTX has reported to have reached the ideal no-wall β limit in Ref. [66]. The maximum toroidal and normalized betas achieved were 25% and 4.3, respectively. When the calculated no-wall limit is exceeded, beta either saturates by the development of NTM or suffer a fast β collapse caused by the resistive wall mode. Very recently, a plasma with toroidal and normalized betas of nearly 40% and 7.2, respectively, were realized by driving a sufficient plasma rotation [27]. In terms of plasma heating by RF waves, HHFW heating is studied extensively on NSTX [67]. Strong wave absorption by electrons, wave acceleration of energetic ions, and

Table 2.1: ST experiments worldwide.

name	R [m]	a [m]	location
CDX-U	0.34	0.22	P.P.P.L. (U.S.A.)
ETE	0.3	0.2	LAP/INPE (Brazil)
Globus-M [59]	0.36	0.24	Ioffe Inst. (Russia)
HIST [60]	0.3	0.24	Himeje Inst. of Tech. (Japan)
HIT-II	0.3	0.2	Univ. of Washington (U.S.A.)
LATE [61]			Kyoto Univ. (Japan)
MAST	0.85	0.65	Culham (U.K.)
NSTX	0.86	0.67	P.P.P.L. (U.S.A.)
Pegasus [62]	≤ 0.4		Univ. of Wisconsin (U.S.A.)
QUEST	0.68	0.40	Kyushu Univ. (Japan)
SUNIST [63]	0.3	0.23	Tsinghua Univ. (China)
TS-4 [64]	~ 0.45		Univ. of Tokyo (Japan)
TST-2	0.38	0.25	Univ. of Tokyo (Japan)
UTST [65]	0.39	0.24	Univ. of Tokyo (Japan)

indications of current drive have been observed. The increase of the edge ion temperature was observed during HHFW heating, and parametric decay of HHFW into the ion Bernstein wave and the ion-cyclotron quasimode was suggested as a possible mechanism [68].

In addition to large STs, a new generation of small STs with unique features has been constructed. Pegasus was constructed at the University of Wisconsin to explore the extremely low aspect ratio regime ($A \to 1$). By the use of a very slim center stack, Pegasus can produces plasmas with $A \geq 1.13$. Very high stable β_t ($\leq 20\%$) and normalized current ($I_\mathrm{N} \equiv I_\mathrm{p}/aB_\mathrm{t} = 6.6\,\mathrm{MA/mT}$) were reported [69]. Tearing modes with low mode numbers, particularly the $m/n = 2/1$ mode limits the achievable plasma current. Plasma start-up by small plasma sources, similar to the plasma gun used in a helicity injection experiment on TST-M [70], was also reported. The initial results using two plasma guns arranged to inject electrons along the magnetic field lines reported in Ref. [62] are quite promising.

HIT was upgraded as HIT-II [71], and a hand-off of a plasma made by coaxial helicity injection to Ohmic heating was recently demonstrated [72]. CHI was also implemented on NSTX, and a successful production of a plasma current has been achieved. However, a recent report from HIT-II [72] suggests that more efforts are required to make purer plasmas.

The relaxation phenomenon is an interesting topic of plasma physics. On HIST, physics experiments of relaxation phenomena of helicity injected plasmas have been performed. A reversal of the external toroidal field is

often used in the generation of a reversed field pinch (RFP) configuration. It is found that when reversing the external toroidal field in a helicity-driven spherical tokamak, the magnetic configuration changes to a spherical RFP, but does not stay in that configuration. Rather, the plasma changes its poloidal field direction spontaneously, and results in a flipped ST, indicating that the conservation of helicity acts to keep the sign of helicity the same [60]. The experiments on TS-3 were scaled up to TS-4. Two flux cores, which have both toroidal and poloidal windings, are used to produce spheromaks, rather than using electrodes [64]. The relaxation process of two spheromaks to an FRC is investigated in detail [73].

Several new machines are also being constructed. UTST is being constructed at Kashiwa Campus of the University of Tokyo to explore the feasibility of the merging start-up scenario previously demonstrated on TS-3 and TS-4, but using only poloidal coils placed outside the vacuum vessel. Removal of in-vessel components is unavoidable when applying this technique in a reactor. However, UTST uses very thin vacuum vessel to allow fast penetration of magnetic field into the vessel, and it seems that further development will be necessary, even after positive results is obtained.

In Globus-M, a doubling of the ion temperature was observed by ICRF heating [74]. The ion heating efficiency depended on the location of the second harmonic hydrogen cyclotron layer and on the concentration of hydrogen ions in a deuterium plasma.

CDX-U has redefined its research objective to plasma-wall interaction (PWI), in particular, exploration of the feasibility of liquid lithium as a plasma facing component. In Ref. [75], extensive lithium wall coating and liquid lithium plasma-limiting surfaces were reported to result in dramatic improvements in Ohmic plasma discharges due to reducing recycling. Increases of the global energy confinement time by factors of up to 6, exceeding the confinement scaling ITER98P(y,1) by a factor of 2–3, were reported. These results will be extended by up-coming experiments on the Lithium Tokamak Experiment (LTX) [76].

Exploration of PWI with a different strategy will be pursured at Kyushu University. CPD (Compact PWI experimental Device), with a similar size to TST-2, has been contructed as a prototype of a following larger device, QUEST (Q-shu University Experiment with Steady-state Spherical Tokamak). The primary objective of these devices are steady-state sustainment of ST plasmas, in which PWI and exhaust handling are anticipated to become a key issue. A closed diverter and a hot tungsten first wall kept at 800 K (equivalent to 1100 K carbon first wall) are planned to keep the 100% wall recycling condition. In order to realize steady state operation, a further development of non-inductive plasma heating and current drive techniques

is required. EBW current drive (EBCD) is planned to sustain the plasma current in steady state.

In summary, proof-of-principle scale experiments are confirming promising features of ST plasmas, and larger scale experiments with Q (= fusion power/auxiliary heating power) ~ 1, such as the Component Text Facility (CTF) are being proposed [77]. On smaller STs, advanced ideas such as EBW/ICRF heating, PWI/exhaust handling, and plasma start-up are being tested.

Chapter 3

EBW theory

In this chapter, theoretical background for the experiment is described. The topics includes 1) description of the electron Bernstein wave (EBW) as a hot plasma electrostatic mode, 2) excitation of EBW by linear mode-conversion from the externally launched electromagnetic wave, 3) propagation of EBW in an in-homogeneous plasma and 4) EBW absorption via electron cyclotron damping. The review of the EBW researches is given in the last section.

3.1 General form of dispersion relation in magnetized plasmas

The dispersion relation for waves in a plasma is obtained from the existence condition of non-trivial solutions of a homogeneous wave equation.

From Maxwell's equations, we have

$$\frac{1}{\mu_0} \nabla \times \boldsymbol{B} = \boldsymbol{j} + \epsilon_0 \frac{\partial \boldsymbol{E}}{\partial t} = \frac{\partial \boldsymbol{D}}{\partial t}, \tag{3.1}$$

$$\nabla \times \boldsymbol{E} = -\frac{\partial \boldsymbol{B}}{\partial t}. \tag{3.2}$$

The plasma response enters through $\boldsymbol{j}$ which is given in terms of macroscopic particle velocities

$$\boldsymbol{j} = \sum_s \boldsymbol{j}_s = \sum_s n_s q_s \boldsymbol{v}_s, \tag{3.3}$$

where n_s is the number density of particles of species s with charge q_s, or more generally

$$\boldsymbol{j} = \sum_s \boldsymbol{j}_s = \sum_s \int d^3\boldsymbol{p}\, \boldsymbol{v}_s f_{s1}(\boldsymbol{r}, \boldsymbol{p}, t), \tag{3.4}$$

where $f_{s1}(\boldsymbol{r}, \boldsymbol{p}, t)$ is the first-order perturbed distribution function for particles of species s.

To obtain the wave equation, it is necessary to know the relationship between the electric field $\boldsymbol{E}$ and $\boldsymbol{j}_s$. As briefly summarized in the next section, consideration of the equation of motion for cold plasma or Vlasov equation for hot plasma leads the linear relationship

$$\boldsymbol{j}_s = -i\omega\epsilon_0\boldsymbol{\chi}_s\boldsymbol{E}, \tag{3.5}$$

where $\boldsymbol{\chi}_s$ is called the susceptibility tensor for particles of species s. Equations 3.1 and 3.2 can be combined to give the homogeneous plasma wave equation, which can be written after Fourier transformation,

$$\boldsymbol{k} \times (\boldsymbol{k} \times \boldsymbol{E}) + \frac{\omega^2}{c^2}\boldsymbol{\epsilon} \cdot \boldsymbol{E} = 0, \tag{3.6}$$

or using the refractive index $\boldsymbol{n} = \boldsymbol{k}c/\omega$

$$\boldsymbol{n} \times (\boldsymbol{n} \times \boldsymbol{E}) + \boldsymbol{\epsilon} \cdot \boldsymbol{E} = 0, \tag{3.7}$$

where $\boldsymbol{\epsilon} = \boldsymbol{1} + \sum_s \boldsymbol{\chi}$ is the dielectric tensor. Choosing the coordinate system with z parallel to the magnetic field and the wave vector lying in x-z plane, Eq. 3.7 can be written in a matrix form as

$$\begin{bmatrix} \epsilon_{xx} - n_z^2 & \epsilon_{xy} & \epsilon_{xz} + n_x n_z \\ \epsilon_{yx} & \epsilon_{yy} - n_x^2 - n_z^2 & \epsilon_{yz} \\ \epsilon_{zx} + n_x n_z & \epsilon_{zy} & \epsilon_{zz} - n_x^2 \end{bmatrix} \begin{bmatrix} E_x \\ E_y \\ E_z \end{bmatrix} = 0. \tag{3.8}$$

Hence the existence condition for non-trivial solutions is that the determinant of the matrix is zero, giving the dispersion relation. Depending on the specific problem to be solved, the determinant of Eq. 3.8 is calculated in different ways. For example, when $n_\parallel (= n_z)$ is defined by an external condition such as antenna structure, the determinant of Eq. 3.8 is expressed as a function of $n_\perp^2 (= n_x^2 + n_y^2)$. In the cold plasma limit, the determinant gives a quadratic equation for $n_\perp^2$,

$$A_1 n_\perp^4 - B_1 n_\perp^2 + C_1 = 0 \tag{3.9}$$

with

$$\begin{aligned} A_1 &= S \\ B_1 &= RL + PS - n_\parallel^2(P + S) \\ C_1 &= P(n_\parallel^2 - R)(n_\parallel^2 - L), \end{aligned} \tag{3.10}$$

where S, D, R, L, and P are Stix parameters defined in Eqs. 3.28 and 3.30.

In some situations, the wave equation 3.7 can be simplified from a vector equation to a scaler equation. This is called the electrostatic approximation and the waves represented well within this approximation are called electrostatic waves. The EBW is one such wave. The approximation lies in the replacement of the vector electric field $\boldsymbol{E}$ by a potential gradient $-\nabla\phi$. The fourier representation

$$\boldsymbol{E} = -\nabla\phi = -i\boldsymbol{k}\phi \tag{3.11}$$

indicates that the electric field is parallel to the wave vector. Because the scaler products of $\boldsymbol{n}$ with 3.7 gives

$$\boldsymbol{n} \cdot \boldsymbol{\epsilon} \cdot (\boldsymbol{E}_\perp + \boldsymbol{E}_\parallel) = 0, \tag{3.12}$$

using Eq. 3.11, the dispersion relation becomes

$$\boldsymbol{n} \cdot \boldsymbol{\epsilon} \cdot \boldsymbol{n} = 0. \tag{3.13}$$

By writing Eq. 3.12 in the form

$$(n^2 \boldsymbol{1} - \boldsymbol{\epsilon}) \cdot \boldsymbol{E}_\perp = \boldsymbol{\epsilon} \cdot \boldsymbol{E}_\parallel, \tag{3.14}$$

one can see that $\boldsymbol{E}_\perp$ will be small compeared to $\boldsymbol{E}_\parallel$ when $n^2 \gg |\epsilon_{ij}|$, which is sufficient to validate the electrostatic approximation. Choosing the coordinate system in the same way as Eq. 3.8, the electrostatic dispersion relation can be written as

$$n_\perp^2 \epsilon_{xx} + 2n_\perp n_\parallel \epsilon_{xz} + n_\parallel^2 \epsilon_{zz} = 0 \tag{3.15}$$

3.2 Dielectric tensor

Given the framework to find the dispersion relation for plasma waves, the remaining task is to obtain the detailed form of the dielectric tensor $\boldsymbol{\epsilon}$. Here, derivation of the dielectric tensor for hot non-relativistic Maxwalliwan plasma needed to a theoretical foundation for the work presented in this thesis is described. A detailed calculation is given in Ref. [78]. As for relativistic effects, which appears only in cyclotron damping of EBW in the immediate vicinity of cyclotron resonance, a description is given in a different section.

The rate of change of the distribution function f as one moves along the trajectory is

$$\frac{df}{dt} = \frac{\partial f}{\partial t} + \frac{\partial f}{\partial \boldsymbol{r}}\frac{\partial \boldsymbol{r}}{\partial t} + \frac{\partial f}{\partial \boldsymbol{p}}\frac{\partial \boldsymbol{p}}{\partial t}, \tag{3.16}$$

where $f = f(\boldsymbol{r}, \boldsymbol{p}, t)$, $\boldsymbol{p} = m\boldsymbol{v}$, and $m = m_0(1 - v^2/c^2)^{-1/2}$ is the relativistic mass. Using the zero-th order trajectory of a charged particle of species s

in a static magnetic field, given by $\frac{dr}{dt} = \boldsymbol{v}$ and $\frac{\partial \boldsymbol{p}}{\partial t} = q_s \frac{\partial \boldsymbol{v}}{\partial c} \times \boldsymbol{B}_0$, the rate of change is written as

$$\frac{df}{dt} = \frac{\partial f}{\partial t} + \boldsymbol{v}\frac{\partial \boldsymbol{r}}{\partial t} + q_s \frac{\boldsymbol{v}}{c} \times \boldsymbol{B}_0 \cdot \frac{\partial \boldsymbol{p}}{\partial t}. \tag{3.17}$$

Dividing the distribution function and the field quantities into zero-th order unperturbed part and the small amplitude 1st order perturbation, the first-order Vlasov equation can be written

$$\frac{df_{s1}}{dt} = q_s(\boldsymbol{E}_1 + \frac{\boldsymbol{v}}{c} \times \boldsymbol{B}_1) \cdot \frac{\partial f_{s0}}{\partial \boldsymbol{p}}. \tag{3.18}$$

and its solution is given by the integration

$$f_{s1}(\boldsymbol{r}, \boldsymbol{p}, t) = -q_s \int_{-\infty}^{t} dt' (\boldsymbol{E}_1(\boldsymbol{r}', t') + \frac{\boldsymbol{v}'}{c} \times \boldsymbol{B}_1(\boldsymbol{r}', t')) \cdot \frac{\partial f_{s0}(\boldsymbol{p}')}{\partial \boldsymbol{p}'} \tag{3.19}$$

along zero-th order trajectory from time $t' = -\infty$ to $t' = t$. After Fourier transform and transforming from Lagrangian to Eulerian coodinates, Eq. 3.19 can be rewritten into

$$\begin{aligned} f_{s1}(\boldsymbol{r}, \boldsymbol{p}, t) = -q_s e^{i\boldsymbol{k}\cdot\boldsymbol{r}-i\omega t} \int_0^\infty d\tau e^{i\beta} \Big\{ & E_x U \cos(\varphi + \omega\tau) + \\ E_y U \sin(\varphi + \omega\tau) + E_z \Big[& \frac{\partial f_0}{\partial p_\parallel} - V\cos(\varphi - \theta + \Omega\tau) \Big] \Big\}, \end{aligned} \tag{3.20}$$

where the definitions of β, φ, θ, U,V, and W (which appears in the next equation) can be found in Ref. [78]. Substituting Eq. 3.20 into Eq. 3.4 and arranging terms in tensor form, and after long calculation, the susceptibility for arbitrary distribution function $f(\boldsymbol{p}_\perp, \boldsymbol{p}_\parallel)$ is given by

$$\begin{aligned} \boldsymbol{\chi}(\mathbf{k}, \omega) &= -\sum_s \frac{\omega_{ps}^2}{\omega^2} \int_0^\infty 2\pi p_\perp dp_\perp \int_{-\infty}^\infty dp_\parallel \sum_{n=-\infty}^\infty \frac{\omega}{\omega - k_\parallel v_\parallel - n\Omega_{cs}} \boldsymbol{S}_n, \\ \boldsymbol{S}_n &= \begin{bmatrix} \frac{n^2 J_n^2}{z^2} p_\perp U & \frac{in J_n J_n'}{z} p_\perp U & \frac{n J_n^2}{z} p_\perp W \\ -\frac{in J_n J_n'}{z} p_\perp U & (J_n')^2 p_\perp U & -i J_n J_n' p_\perp W \\ \frac{n J_n^2}{z} p_\parallel W & i J_n J_n' p_\parallel U & (J_n)^2 p_\parallel W, \end{bmatrix} \end{aligned} \tag{3.21}$$

where z denotes $k_\perp v_\perp/\Omega$. For a Maxwellian distribution function, further calculations from Eq.3.21 lead to

$$\boldsymbol{\chi} = \frac{\omega_{pe}^2}{\omega} \sum_n e^{-\lambda} Y_n(\lambda), \tag{3.22}$$

where

$$
Y_{\mathrm{n}}(\lambda) = \begin{bmatrix} \frac{n^2 I_n}{\lambda} A_n & -in(I_n - I_n') A_n & \frac{k_\perp}{\Omega} \frac{nI_n}{\lambda} B_n \\ in(I_n - I_n') A_n & (\frac{n^2}{\lambda} I_n + 2\lambda I_n - 2\lambda I_n') A_n & \frac{ik_\perp}{\Omega} (I_n - I_n') B_n \\ \frac{k_\perp}{\Omega} \frac{nI_n}{\lambda} B_n & -\frac{ik_\perp}{\Omega} (I_n - I_n') B_n & \frac{2(\omega - n\Omega)}{k_{//} v_{th}^2} I_n B_n \end{bmatrix}
$$
(3.23)

and A_n and B_n are defined as

$$
A_n = \frac{1}{k_\parallel v_{th}} Z_0(\zeta_{\mathrm{n}}),
$$
(3.24)

$$
B_n = -\frac{1}{2k_\parallel} \frac{dZ_0(\zeta_{\mathrm{n}})}{d\zeta_{\mathrm{n}}},
$$
(3.25)

where

$$
\zeta_{\mathrm{n}} = \frac{\omega - n\Omega}{k_\parallel v_{\mathrm{th}}}
$$
(3.26)

In Eq. 3.23,

$$
\lambda = \frac{k_\perp^2 \kappa T_\perp}{m\Omega^2} = \frac{1}{2} k_\perp^2 \rho^2
$$
(3.27)

is related to the ratio of Larmor radius to the wave length, and determines the importance of finite temperature effect.

$Z_0(\zeta_n)$ is called the plasma dispersion function those imaginary part determines the significance of the Landau and cyclotron damping. The imaginary part is an odd function having maximum at $\zeta_n = 0$ and, decreasing monotonically as $|\zeta_n|$ increases, goes to zero when $\zeta_n \to \pm\infty$. The simplest example is the damping that occurs when $k_\perp = 0$, and accordingly $\lambda = 0$. In this case, the remaining terms in the susceptibility tensor are $Y_0(0)$ and $Y_{\pm 1}(0)$. $Y_0(0)$ becomes proportional to B_0, those imaginary part have maximum around $\zeta_0 = 1$, corresponding to the absorption when the phase velocity is near the thermal velocity v_{th} (Landau damping). $Y_{\pm 1}(0)$ becomes proportional to $A_{\pm 1}$ that has the largest imaginary part at $\zeta_{\pm 1} \sim 0$, which corresponds to the absorption occurring near the cyclotron frequency (cyclotron damping).

When the temperature is negligibly small ($\lambda = 0$ limit) the susceptibility tensor is significantly simplified (cold plasma apporximation),

$$
\boldsymbol{\chi}_s = \begin{bmatrix} -\frac{\omega_{ps}^2}{\omega^2 - \Omega^2} & -i\frac{\Omega\omega_{ps}^2}{\omega(\omega^2 - \Omega^2)} & 0 \\ i\frac{\Omega\omega_{ps}^2}{\omega(\omega^2 - \Omega^2)} & -\frac{\omega_{ps}^2}{\omega^2 - \Omega^2} & 0 \\ 0 & 0 & -\frac{\omega_{ps}^2}{\omega^2} \end{bmatrix}
$$
(3.28)

Eq.3.28 gives the definition for Stix parameters, S, D, P, R, and L. In cold plasma theory, the dielectric tensor are frequently used using these parameters as

$$\boldsymbol{\epsilon} = 1 + \sum_s \boldsymbol{\chi}_s = \begin{bmatrix} S & -iD & 0 \\ -iD & S & 0 \\ 0 & 0 & P \end{bmatrix} \tag{3.29}$$

and

$$\begin{aligned} R &\equiv S + D \\ L &\equiv S - D \end{aligned} \tag{3.30}$$

The frequencies of wave modes relevant to this thesis are high ($\omega \sim \omega_{\mathrm{ce}}$) and the motion of ions can be neglected. Hence it is sufficient to consider only electron contribution.

3.3   Quasi-transverse mode

This section and the next are devoted to the description of important wave modes to understand the electron Bernstein wave physics. In this section, quasi-transverse (QT)-X and QT-O modes are described. They are cold plasma modes and are used to measure the EBW generated in plasma by the detector located outside the plasma or to excite the EBW by a wave launched from outside the plasma. The cut-off and resonance associated with these modes determine the excitation of EBW.

Neglecting the ion response in Eq.3.28, the determinant of the matrix on the left hand side of Eq.3.8 becomes (Altar-Appleton-Hartree dispersion relation)

$$n^2 = 1 - \frac{2\omega_{pe}^2(\omega^2 - \omega_{pe}^2)/\omega^2}{2(\omega^2 - \omega_{pe}^2) - \Omega_e^2 \sin^2\theta \pm \Omega_e\Delta}, \tag{3.31}$$

where

$$\Delta = [\Omega_e^2 \sin^4\theta + 4\omega^{-2}(\omega^2 - \omega_{pe}^2)^2 \cos^2\theta]^{1/2}. \tag{3.32}$$

A convenient factoring of Eq.3.31 is possible, when the size of the two terms of Δ are significantly different. The case in which

$$\Omega_e^2 \sin^4\theta \gg 4\omega^{-2}(\omega^2 - \omega_{pe}^2)^2 \cos^2\theta]^{1/2}. \tag{3.33}$$

is called quasi-transverse (QT), since $\theta = \pi/2$ corresponds to the wave vector perpendicular to the magnetic field. In this case, Eq.3.31 becomes

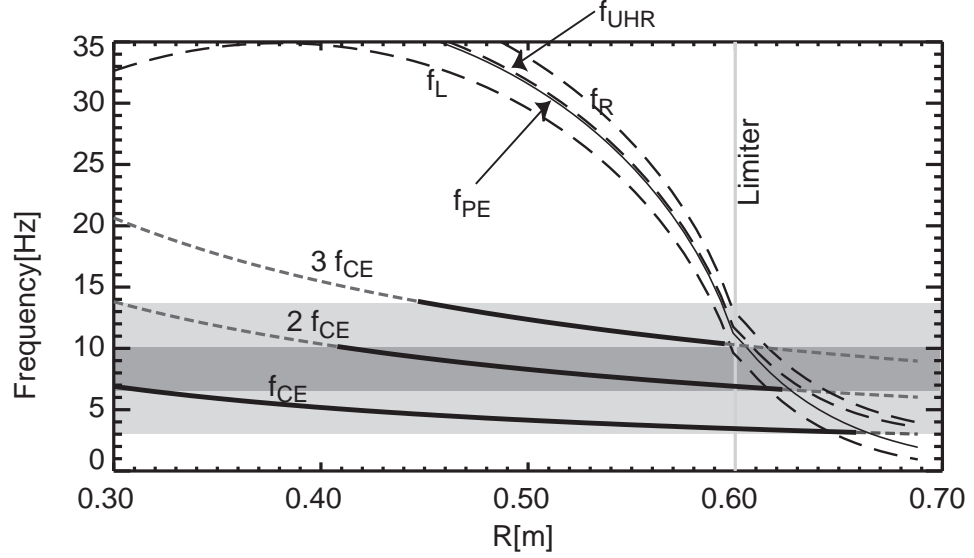$$n^2 = \frac{\omega^2 - \omega_{pe}^2}{\omega^2 - \omega_{pe}^2 \cos^2\theta}, \tag{3.34}$$

Figure 3.1: Profiles of f_{ce}, f_{pe}, f_L, f_R and f_{UHR} in a ST plasma. $B_t = 0.2\,\text{T}$, $n_e = 1 \times 10^{19} m^{-3}$, and $n_{\text{limiter}} = 0.1 \times 10^{19} m^{-3}$ was used.

or

$$n^2 = \frac{(\omega^2 - \omega_{pe}^2)^2 - \omega^2 \Omega_e^2 \sin^2 \theta}{\omega^2 (\omega^2 - \omega_{pe}^2) - \omega^2 \Omega_e^2 \sin^2 \theta}. \tag{3.35}$$

The former is called the ordinary mode (QT-O) and the latter is called the extraordinary mode (QT-X).

The QT-O mode is independent of the magnetic field strength and its cutoff occurs when $\omega = \omega_{pe}$. The QT-O mode can propagate only where the electron density is so low that the electron plasma frequency is lower than the wave frequency. The QT-X mode has two cutoffs at

$$\omega = \frac{\pm \Omega_e \sin \theta + \sqrt{\Omega_e^2 \sin^2 \theta + 4\omega_{pe}^2}}{2} \tag{3.36}$$

and a resonance at

$$\omega^2 = \omega_{pe}^2 + \Omega_e^2 \sin^2 \theta. \tag{3.37}$$

These cutoffs and resonance are called left-hand cutoff, right-hand cutoff and upper hybrid resonance, respectively. For perpendicular propagation, the left-hand cutoff frequency ω_L, the right-hand cutoff frequency ω_R and

the upper hybrid resonance frequency ω_{UHR} are given by,

$$\omega_{\mathrm{R}} = (\Omega_{\mathrm{ce}} + \sqrt{\Omega_{\mathrm{ce}}^2 + 4\omega_{\mathrm{pe}}^2})/2, \tag{3.38}$$

$$\omega_{\mathrm{L}} = (-\Omega_{\mathrm{ce}} + \sqrt{\Omega_{\mathrm{ce}}^2 + 4\omega_{\mathrm{pe}}^2})/2, \tag{3.39}$$

$$\omega_{\mathrm{UHR}} = \sqrt{\omega_{\mathrm{pe}}^2 + \Omega_{\mathrm{ce}}^2}. \tag{3.40}$$

Figure 3.1 shows the profiles of f_{ce}, f_{pe}, f_{L}, f_{R}, and f_{UHR} in a TST-2 plasma. $B_{\mathrm{t}} = 0.2\,\mathrm{T}$, $n_{\mathrm{e}} = 1 \times 10^{19} m^{-3}$ at the plasma center and $n_{\mathrm{limiter}} = 0.1 \times 10^{19} m^{-3}$ at the plasma edge defined by the limiter are used in the calculation. These parameters are typical in plasmas used in the radio-reflecomter experiments presented in Sec. 6.1. Noted as peculiarity of ST plasma before, f_{pe} is an order of magnitude larger than f_{ce} in the plasma core region and the region where $f_{\mathrm{pe}} > f_{\mathrm{ce}}$ covers most of the plasma except for the very edge region. According to Eq. 3.34 and Eq. 3.35, the O-mode can propagate where $\omega > \omega_{\mathrm{pe}}$, while the X-mode can propagate where $\omega > \omega_{\mathrm{R}}$ or $\omega_{\mathrm{UHR}} > \omega > \omega_{\mathrm{L}}$. Resultantly, both modes cannot propagate in most of the ST plasma.

Figure 3.2 shows the profiles for $k_\perp$ of the 8.2 GHz microwave in the edge region at two different magnetic field strengths. The wave number for zero density corresponds to the vacuum wave length. Again in this figure, it is shown that the region where the O-mode and the X-mode can propagate is very restricted in low density region. A high k, short wavelength, mode is connected to the X-mode at the upper hybrid resonance. This is the electron Bernstein wave, described in detail in the next section.

3.4 Electron Bernstein wave

It is appropriate now to evaluate the electrostatic dispersion relation Eq. 3.13 or Eq. 3.15 within the framework of hot plasma kinetic theory, Eq.3.22. Assuming $T_\perp = T_\parallel$ and $V = 0$, and considering only the electron contribution, the dispersion relation becomes

$$
\begin{aligned}
& k_\perp^2 + k_\parallel^2 + 2\frac{\omega_{\mathrm{pe}}^2}{v_{\mathrm{th}}^2}[1 + \sum_n e^{-\lambda} I_n(\lambda)\zeta_0 Z_0(\zeta_n)] = \\
& k_\perp^2 + k_\parallel^2 + 2\frac{\omega_{\mathrm{pe}}^2}{v_{\mathrm{th}}^2} \sum_n e^{-\lambda} I_n(\lambda)(1 + \zeta_0 Z_0(\zeta_n)) = 0.
\end{aligned}
\tag{3.41}
$$

In the case of exactly perpendicular propagation ($k_\parallel = 0$), by retaining only the first term of an asymptotic expansion of the plasma dispersion
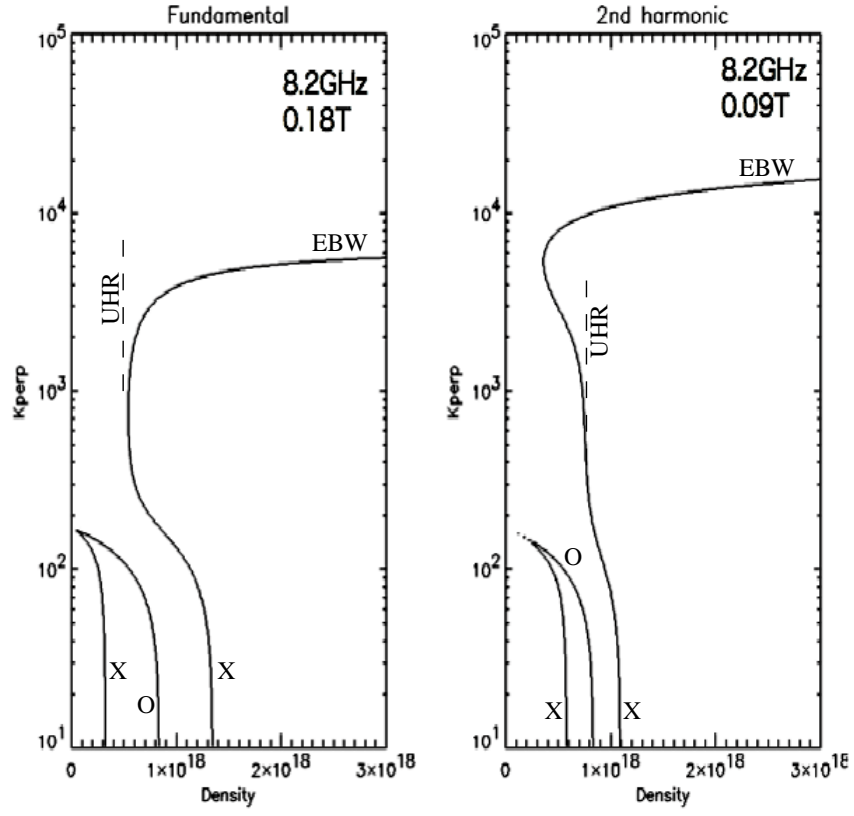
Figure 3.2: Expanded profiles of $k_\perp$ of the perpendicularly injected 8.2 GHz wave in the plasma edge region for (left) $B_t = 0.09T$ corresponding to fundamental heating, and (right) $B_t = 0.18T$ corresponding to 2nd harmonic heating in the core region.
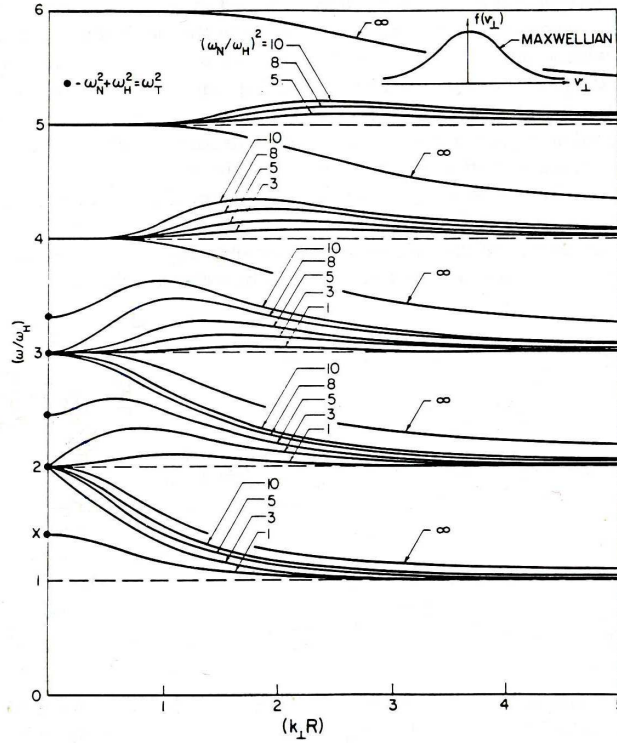
Figure 3.3: Dispersion relationship of EBW (by courtesy of [78]). ω_{H} and ω_{N} are the cyclotron frequency and the plasma frequency, respectively.

function, $Z_0(\zeta_n) \sim -k_\parallel v_{\mathrm{th}}/(\omega - n\Omega)$, and then taking the $k_\parallel \to 0$ limit, the dispersion relation reduces to

$$1 = 2\frac{\omega_{\mathrm{pe}}^2}{\Omega_{\mathrm{ce}}^2} \sum_{n=1}^{\infty} \frac{e^{-\lambda} I_n(\lambda)}{\lambda} \frac{n^2}{q^2 - n^2} \tag{3.42}$$

where

$$q = \frac{\omega}{\Omega_{\mathrm{ce}}}. \tag{3.43}$$

The dispersion relation for the EBW is shown in Fig.3.3. It is shown that all EBWs have resonances at the cyclotron frequency and its harmonics. The lowest frequency EBW has cutoff at UHR. In our experimental condition, the frequency is determined by the external microwave power source and parameters such as the density, and correspondingly ω_{pe}, changes in the radial direction. The EBW dispersion under the experimental condition is shown in Fig. 3.4 (Figure 3.2 corresponds to an expanded view in the range
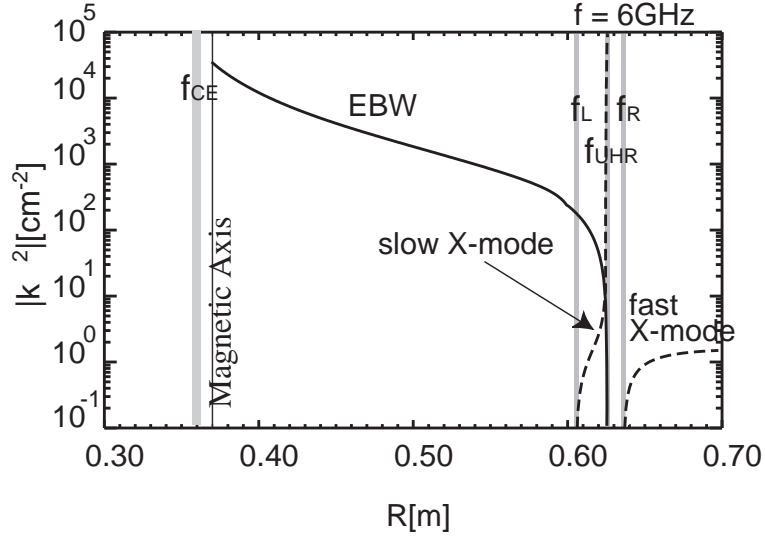
Figure 3.4: $k_\perp^2$ profile of EBW at 6 GHz. Plasma parameters are same as Fig.3.1

0.6 m $< R <$0.7m). At UHR, $k_\perp$ of the EBW goes to zero while $k_\perp$ of the X-mode goes to infinity. This provides the condition for mode-conversion between these waves to occur as discussed in next section.

Another noticeable point of Eq. 3.42 is that it has no imaginary part and hence no absorption could happen. Moreover, since the term $\frac{n^2}{q^2-n^2}$ goes to infinity at a cyclotron resonance, $k_\perp$ goes to either zero or infinity there ($e^{-\lambda}I_n(\lambda)$ needs to go to zero). Obviously these are caused by taking the limit of the argument of Z_0 in an ambiguous manner, namely $\omega \to n\Omega_{ce}$ and $k_\parallel \to 0$ simultaneously. A proper analysis of the EBW near the cyclotron resonance requires a relativistic treatment, in which case the wave number remains finite and a finite absorption reappears (See Sec. 3.7).

3.5 Mode conversion

3.5.1 Difficulties of exciting the EBW in an ST plasma

To heat the plasma by am external microwave source, it is necessary to excite a proper plasma wave in the plasma, in this case the EBW. As shown in Fig.3.4, the EBW encounters a cutoff at UHR and is confined inside the plasma. In addition, the EBW is an electrostatic wave, having its electric fields parallel to the wave vector. These features create a particular difficulty

of using the EBW for plasma heating, since direct excitation by an externally launched electromagnetic wave is impossible. Meanwhile, the X-mode (denoted as the slow X-mode in the figure) has a resonance at UHR. It implies that a linear mode conversion between the X-mode and the EBW occurs near UHR. The linear mode conversion (MC) occurs when the dispersion curves of two dirfferent modes coalesce in a particular region of the plasma and the power of one mode is transferred to the other mode. Since the X-mode is electromagnetic, it seems suitable for excitation by an external microwave source. In fact, in some experimental condition, there is no f_L cutoff in the plasma and the EBW heating using the high field side incidence slow X-mode has been demonstrated [7, 8] (see the detailed description in Sec. 3.8),

Another difficulty under the current experimental condition is that the slow X-mode is apparently inaccessible. There is the f_L cutoff on the high field side of the slow X-mode propagation region and the evanescent region between UHR and the right-hand isolates the slow X-mode from the branch accessible from outside the plasma (denoted as the fast X-mode in the figure). However, note that the thickness of the evanescent region is of the order of cm, which is comparable to the wave length of the injected microwave. Remembering that the WKB approximation gives the phase in in-homogeneous medium by $i \int k(x)dx$, the attenuation in this region is not expected to be complete and some power will tunnel through it.

To be exact, the WKB approximation is violated when $k(x)$ changes rapidly as in this region and one has to solve the Maxwell equations directly (full-wave analysis) to obtain a complete picture. What full-wave analysis tells us is that a significant power pass through the evanescent region and is mode converted to the EBW. It is predicted that even a complete conversion to the EBW is possible if a specific condition is satisfied. Before proceeding to the full-wave analysis, consider qualitatively the condition under which a complete MC occurs. The power that passed through the evanescent region travels towards the high density side as the slow X-mode. The slow X-mode is reflected at the high density cutoff and travels back to UHR. Some fraction of power passes through the evanescent region and appears on the fast X-mode branch again. Suppose that this reflected wave has the same amplitude and the phase difference of π compared to the wave reflected at the right-hand cutoff, then these two reflected waves cancel each other and total reflection becomes zero, resulting in 100% MC.

The above consideration implies that to understand MC under the current situation, one has to treat the UHR and the two cutoffs as a set (triplet). In the following two sections, the wave is considered analytically using the cold plasma full-wave equation and the MC efficiency is obtained based on a resonant absorption model. The numerical technique to calculate the MC
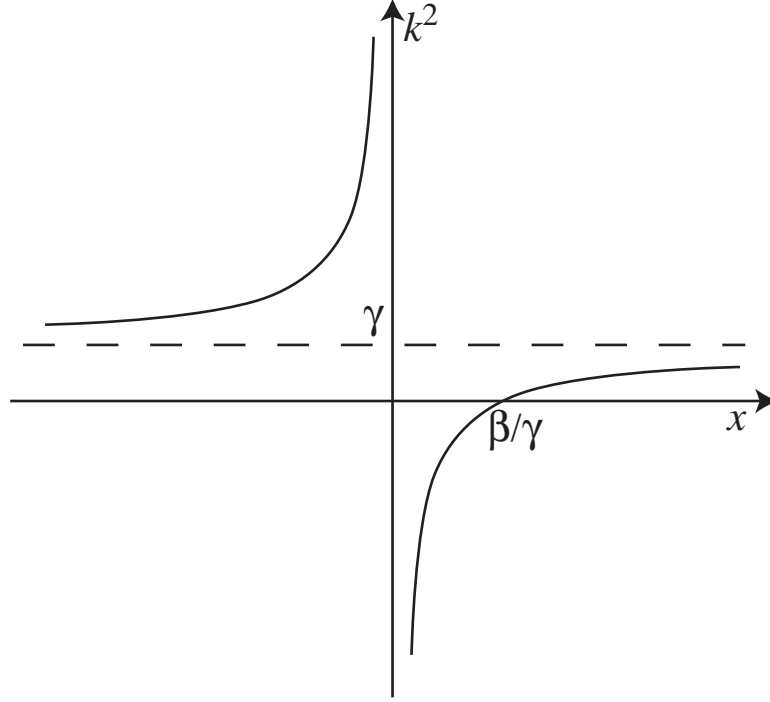
Figure 3.5: k^2 profile near a cutoff-resonance doublet.

efficiency for arbitrary density profile is given in Sec. 3.5.6. Though it is convenient for calculation of the MC efficiency, the model lacks a behavior of a wave after mode convertion to the EBW. Inclusion of the EBW requires consideration of finite temperature effects and is reviewed in the Sec. 3.8.

3.5.2 Budden model

Consider the dispersion of the perpendicularly propagating X-mode given by

$$n_\perp^2 = \left(\frac{ck_\perp}{\omega}\right)^2 = \frac{RL}{S} = \frac{(\omega^2 - \omega_L^2)(\omega^2 - \omega_R^2)}{\omega^2(\omega^2 - \omega_{UHR}^2)}. \tag{3.44}$$

Suppose both $\omega = \omega_R$ and $\omega = \omega_{URL}$ layers are located in a narrow region, and that the spatial dependence of these values are given by linear functions of distance. For the time being, the left-hand cutoff is assumed to be located far away and is excluded from the analysis. The resultant dispersion relation is a back-to-back linear and singular turning point doublet that considered by Budden [79] and a model dispersion relation is given by

$$n_\perp^2 = (\gamma - \beta/x), \tag{3.45}$$

where γ and β are positive constants and x is the distance normalized by c/ω. The spatial profile of this dispersion relation is shown in Fig. 3.5, indicating a resonance at $x = 0$ and a cutoff at $x = \beta/\gamma$.

Suppose all spatial variations are along the x direction and the system is uniform in y and z directions. To construct a wave equation for inhomogenous plasma, remember that $\boldsymbol{k}$ comes from Fourier transform of ∇ in Eq.3.1 and 3.2. While Fourier transform in y and z directions are still valid, it is necessary to retain differentiation in the x direction, yielding

$$\frac{d^2 E}{dx^2} + (\gamma - \beta/x)E = 0, \tag{3.46}$$

which is called the Budden equation. The Budden equation can be expressed in the form of Whittaker's representation of the confluent hypergeometric function

$$\frac{d^2 E}{dz^2} + \left(-\frac{1}{4} - \frac{1}{2}\frac{i\eta}{z}\right)E = 0, \tag{3.47}$$

by replacing $z = -2i\sqrt{\gamma}\xi$ and $\eta = \beta/\sqrt{\gamma}$. The solutions are given by the Whittaker functions $W_{\kappa,1/2}(z)$ and $W_{-\kappa,1/2}(-z)$.

In order to evaluate the mode-conversion efficiency, one does not need to know the Whittaker functions for arbitrary z but only need its asymptotic form. In connecting the asymptotic forms of Whittaker functions care must be taken of the Stokes phenomena. Since we assume time dependence of $e^{-\omega t}$, the pole located at $x = 0$ is displaced above the real axis when the collision-frequency is finite. To preserve continuity when the collision-frequency is finite, the integration path must go below the pole and the asymptotic forms are given by

$x \to -\infty$

$$W_{\kappa,1/2}(z) \sim z^{\kappa}e^{-z/2} \tag{3.48}$$

$$W_{-\kappa,1/2}(-z) \sim z^{\kappa}e^{i\pi\kappa}e^{z/2} \tag{3.49}$$

$x \to \infty$

$$W_{\kappa,1/2}(z) \sim z^{\kappa}e^{-z/2} \tag{3.50}$$

$$W_{-\kappa,1/2}(-z) \sim \left(z^{-\kappa}e^{z/2} - \frac{2\pi i}{\Gamma(1/2 - \mu + \kappa)\Gamma(1/2 + \mu + \kappa)}z^{\kappa}e^{-z/2}\right)e^{i\pi\kappa} \tag{3.51}$$

Looking at $W_{\kappa,1/2}(z)$ on the right ($x \to \infty$), the asymptotic form of $e^{-z/2} = e^{-2i\sqrt{\gamma}x}$ represents a wave moving to the right (leaving the doublet), and there is no term for a wave moving to the left (entering the doublet). Hence, $W_{\kappa,1/2}(z)$ corresponds to the wave entering doublet from the left.

There is no left moving wave in $W_{\kappa,1/2}(z)$ on the right of the doublet ($x \to -\infty$), indicating that no reflection occurs when a wave enters from the left. As for transmission, the change of amplitude comes from $z^\kappa = |z|^\kappa e^{\kappa \times \arg z}$ and the power transmission coefficient T becomes

$$T = \left| \frac{\lim_{z \to i\infty} z^\kappa e^{-z/2}}{\lim_{z \to -i\infty} z^\kappa e^{-z/2}} \right|^2 = e^{-\pi\eta}. \tag{3.52}$$

In the same way, since $W_{-\kappa,1/2}(-z)$ on the left ($x \to -\infty$) contains only the left moving wave, $W_{-\kappa,1/2}(-z)$ is considered a solution for the wave entering the doublet from the right. In this case, Eq. 3.49 contains waves propagating in both directions, predicting that both reflection and transmission occur, when a wave enters from the right. The power transmission and reflection coefficients are

$$T = e^{-\pi\eta} \tag{3.53}$$

$$R = (1 - e^{-\pi\eta})^2, \tag{3.54}$$

respectively.

3.5.3 Resonant absorption model

It the Budden equation, it is found that, the wave power entering the doublet is not conserved. In the case of the left moving wave, the lost power is

$$C_{\text{doublet}} = 1 - T - R = e^{-\pi\eta} - e^{-2\pi\eta} \tag{3.55}$$

and is interpreted to be absorbed by the doublet. This power balance gives an estimate of the MC efficiency from the X-mode to the EBW.

The Budden model does not specify where the lost power goes. The answer depends on the mechanism neglected in the dispersion relation, Eq. 3.46. Expanding $e^{-\lambda}I_n(\lambda)$ in Eq. 3.22 gives the first order finite temperature correction on S, R, and L in Eq.3.44, which is proportional to $k_\perp^2$. The resultant equation becomes a 4th order equation of $k_\perp$, in which the singularity at $S = 0$ is removed and a new branch appreas. As show in Fig.3.4, the new branch is the EBW which can be excited via MC occurring near UHR.

One might expect that the lost power is the power transferred to the new branch. However, the finite temperature effect also includes dissipative phenomena such as Landau, transit-time and cyclotron damping The dissipative phenomena associated with particle collision, introducing a non-zero imaginary part to γ, may also contribute to wave absorption. Only when all these other effects can be neglected, it is justified to assign the lost power to the power transferred to the new branch.
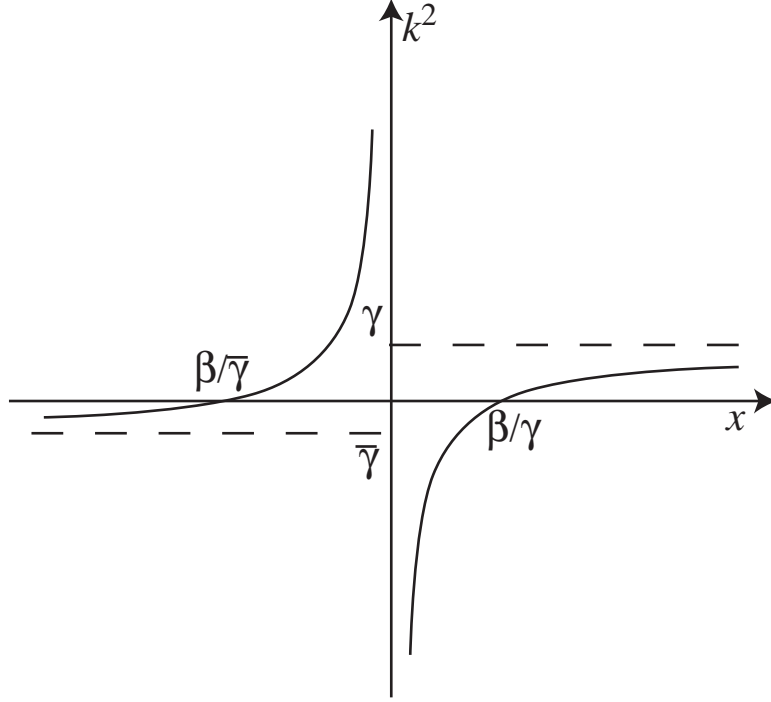
Figure 3.6: k^2 profile near a cutoff-resonance-cutoff triplet.

3.5.4   L-UHR-R triplet

Consider now that all $\omega = \omega_{\mathrm{L}}$, $\omega = \omega_{\mathrm{R}}$ and $\omega = \omega_{\mathrm{URL}}$ are located in a narrow region. Modifying Budden's dispersion relation, a model dispersion relation for this case is given by

$$n_\perp^2 = \begin{cases} (\gamma - \beta/x) & \text{if } z > 0 \ , \\ (-\bar{\gamma} - \beta/x) & \text{if } z \leq 0 \end{cases} \tag{3.56}$$

where β, γ, and $\bar{\gamma}$ are all positive parameters and x is the distance normalized by c/ω. The spatial profile of this dispersion relation is shown in Fig.3.6. The MC efficiency for this model is given by [14]

$$C = 4e^{-\pi\eta}(1 - e^{-\pi\eta})\cos^2(\varphi) \tag{3.57}$$

$$\varphi = \frac{\pi}{2} + \cos^{-1}\left(\frac{N_{\mathrm{R}}^2 - N_{\mathrm{I}}^2}{N_{\mathrm{R}}^2 + N_{\mathrm{I}}^2}\right)$$

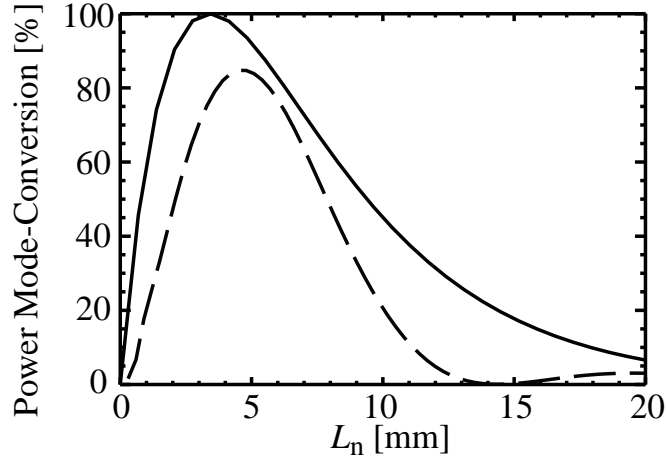Figure 3.7: The maximum MC efficiency C_{max} (solid line) and the MC efficiency calculated using 1-D full-wave code (dashed line) of the low field side X-B scenario for the frequency of $8.2\,\text{GHz}$ and the magnetic field of $0.18\,\text{T}$.

where N_{R} and N_{I} are the real and imaginary part of N, respectively, and N is given by

$$
\begin{aligned}
N ={}& \ln\left(\frac{i\eta}{\bar{\eta}}\right) + \pi\left\{i\coth\left(\frac{\pi}{2}\eta\right) + \cot\left(\frac{\pi}{2}\bar{\eta}\right)\right\} - \frac{1}{\bar{\eta}} - \frac{i}{\eta} \\
& + \psi\left(1 + \frac{1}{2}\bar{\eta}\right) - \psi\left(1 + \frac{i}{2}\eta\right)
\end{aligned}
\tag{3.58}
$$

ψ is the Psi function and $\bar{\eta} = \beta/\sqrt{\bar{\gamma}}$.

Compared to the original Budden model, while Eq. 3.55 gives the maximum MC efficiency of 25 % when $e^{-\pi\eta} = 1/2$, Eq. 3.57 gives the maximum MC efficiency of 100 %, when $e^{-\pi\eta} = 1/2$ and φ is $n\pi$, (where n is integer), consistent with the preliminary consideration described in the previous section.

3.5.5 Low field side incidence X-B MC scenario

The MC described in the previous section is the low field side incidence X-B MC scenario. The X-mode is injected from the low field side of the torus towards the triplet composed of the UHR and the two cutoffs. The MC efficiency depends on η in Eq. 3.57. η vary by changing the distance between UHR and cutoffs. Comparing Eq. 3.44, Eq. 3.56, and $\eta = \beta/\sqrt{\bar{\gamma}}$, η

is expressed by local plasma parameters as

$$\eta = \frac{\Omega_{\mathrm{ce}} L_{\mathrm{n}}}{c\alpha}\left(\sqrt{\alpha^2 + 1} - 1\right)^{1/2}, \tag{3.59}$$

where $\alpha = \omega_{\mathrm{pe}}/\Omega_{\mathrm{ce}}$ and L_{n} is the density scale length at UHR. Figure 3.7 shows the MC efficiency as a function of L_{n}. The one dimensional full-wave code described in the next section is used in the calculation. The magnetic field of 0.18 T and the wave frequency of 8.2 GHz is used in the calculation, which was used in the EBW heating experiments of the present thesis. The maximum MC efficiency C_{max} is the efficiency excluding the contribution of the phase in Eq.3.57. It is found that the calculated MC efficiency is about 80% at optimum density scale length of about 5 mm, which is close to the best condition for C_{max}.

In this MC scenario, the X-mode is injected perpendicularly to the magnetic field. Such an X-mode is linearly polarized and can be launched by a simple horn antenna, which is an advantage of this MC scenario. However, the optimum L_{n} is found to be considerably shorter than the naturally occurring L_{n} at the edge of TST-2 plasma. In this research, we used a local limiter to shorten L_{n} (See Sec.5.5).

3.5.6   Numerical method

In order to calculate the MC efficiency for an arbitrary $k_{\parallel}$ and density and magnetic field profiles, one needs to rely on numerical computation. A technique described here calculates the MC efficiency for one dimensional stratified plasma. The size of the mode conversion region ($\sim$cm) is small compared to the tokamak plasma ($\sim$30 cm in TST-2). The plasma is assumed to be uniform in y and z directions. All variables including the wave electric and magnetic fields ($\mathbf{E}$ and $\mathbf{B}$, respectively), the static magnetic field strength B_0, its angle from the z axis φ, and the electron density n_{e} are assumed to depend on x alone and to have a functional form of $A(x)e^{i(k_{\mathrm{y}}y + k_{\mathrm{z}}z - \omega t)}$.

In the calculation of the susceptibility χ (Eq. 3.28), the static magnetic field was taken to be in the z direction. Rotating the coordinates around the x axis by φ, the susceptibility for an arbitrary magnetic field angle is given by

$$\boldsymbol{\chi} = \frac{\omega_{\mathrm{pe}}^2}{\omega^2 - \Omega_{\mathrm{ce}}^2}\begin{bmatrix} 1 & i\beta\cos\varphi & -i\beta\sin\varphi \\ -i\beta\cos\varphi & 1 - \beta^2\sin^2\varphi & -\beta^2\sin\varphi\cos\varphi \\ i\beta\sin\varphi & -\beta^2\sin\varphi\cos\varphi & 1 - \beta^2\cos^2\varphi \end{bmatrix}, \tag{3.60}$$

where $\beta = \Omega_{\mathrm{ce}}/\omega$.

Generally speaking, the susceptibility tensor needs some modification when the plasma is inhomogenous, since it is given by integrating the first order perturbed distribution function. However, in the cold plasma approximation (zero Larmor radius limit), the x dependence of the perturbed distribution function does not contribute to the susceptibility tensor. Hence, Eq. 3.60 can be used directly with Maxwell equations, Eq. 3.1 and Eq. 3.2. Recalling $\boldsymbol{j}_s = -i\omega\epsilon_0\boldsymbol{\chi}_s\boldsymbol{E}$ and $\boldsymbol{\epsilon} = \mathbf{1} + \sum_s \boldsymbol{\chi}_s$ and using the above mentioned functional form, Maxwell equations yield 6 linear equations for field parameters $\mathbf{E}$ and $\mathbf{B}$ and their derivatives dE_y/dx, dE_z/dx, dB_y/dx, and dB_z/dx. Derivatives of E_x and B_x do not appear in the equations. Omitting E_x and B_x, equations are arranged in the following form

$$\frac{c}{\omega}\epsilon_{xx}\frac{d}{dx}\begin{bmatrix} E_y \\ E_z \\ B_y \\ B_z \end{bmatrix} = i\mathbf{M}\begin{bmatrix} E_y \\ E_z \\ B_y \\ B_z \end{bmatrix} \tag{3.61}$$

where

$$\mathbf{M} = \begin{bmatrix} -n_y\epsilon_{xy} & -n_y\epsilon_{xz} & -n_y n_z & \epsilon_{xx} - n_y^2 \\ -n_z\epsilon_{xy} & -n_z\epsilon_{xz} & \epsilon_{xx} - n_z^2 & -n_y n_z \\ a_1 & a_2 & n_z\epsilon_{xz} & n_y\epsilon_{xz} \\ a_1 & a_3 & n_z\epsilon_{xy} & n_y\epsilon_{xy} \end{bmatrix} \tag{3.62}$$

and $n = ck/\omega$, $a_1 = \epsilon_{xx}(\epsilon_{yz} + n_y n_z) + \epsilon_{xy}\epsilon_{xz}$, $a_2 = \epsilon_{xx}(\epsilon_{zz} - n_y^2) + \epsilon_{xz}^2$, and $a_3 = \epsilon_{xx}(\epsilon_{yy} - n_z^2) + \epsilon_{xy}^2$.

This is the first order differential equation. The singularity at UHR is resolved by introducing a small positive imaginary part to ω. Then, equations can be solved numerically when boundary conditions are specified for E_y, E_z, B_y, and B_z and their derivatives.

What we want to know is the reflected and the transmitted power when we inject a wave with a particular polarization from the vacuum side. It is difficult to specify the boundary condition at the vacuum side, since the wave has both injected and reflected components. At the boundary deep inside the plasma, only waves leaving form the MC region can exist, because both modes are evanescent there. Hence, integration must start from the interior boundary. After integrating the two leaving modes back to the vacuum boundary, one finds them having both entering and leaving components. Separating these components and selecting the linear combination of the two modes to match the polarization of the injected wave, the reflected wave power for that polarization is obtained, giving the MC efficiency based on the resonant absorption model.

3.6   Propagation of EBW

Since the EBW is a short wave length mode, propagation of the EBW between the upper hybrid resonance and the cyclotron resonance is well described by the WKB approximation. The trajectory of the EBW can be calculated by ray-tracing. For calculation in a toroidal device like ST, it is convenient to use the toroidal coordinate system (r, θ, ϕ), where r is the minor radius and θ and ϕ are poloidal and toroidal angles, respectively, and the ray equations are

$$\frac{dk_{\mathrm{r}}}{dt} = -\frac{\partial D}{\partial r}, \tag{3.63}$$

$$\frac{dm}{dt} = -\frac{\partial D}{\partial \theta}, \tag{3.64}$$

$$\frac{dn}{dt} = -\frac{\partial D}{\partial \phi}, \tag{3.65}$$

$$\frac{dr}{dt} = \frac{\partial D}{\partial k_{\mathrm{r}}}, \tag{3.66}$$

$$\frac{d\theta}{dt} = \frac{\partial D}{\partial m}, \tag{3.67}$$

$$\frac{d\phi}{dt} = \frac{\partial D}{\partial n}, \tag{3.68}$$

where m and n are poloidal and toroidal mode numbers, defined by $m = rk_\theta$ and $n = rk_\phi$, and $D = 0$ is the dispersion relation for a uniform plasma. The third equation shows explicitly that the toroidal mode number is conserved when toroidal symmetry $\frac{\partial}{\partial \phi} = 0$ exists.

When the medium is dissipation free, the dielectric tensor is Hermitian and D is a real function. However, in a dispersive medium, D becomes complex, making the evaluation of right hand side not so straight forward. When the Hermitian part of the dielectric tensor is larger than the anti-Hermitian part ($\epsilon_{ij} + \epsilon_{ij}^\dagger \gg \epsilon_{ij} - \epsilon_{ij}^\dagger$), however, the extension of the ray equations is well-known. In such circumstance, the anti-Hermitain part does not affect the leading order of the real part of D and its effect appears on the imaginary part of D.

The deposition of wave energy is computed by integrating the damping decrement γ along the ray trajectory
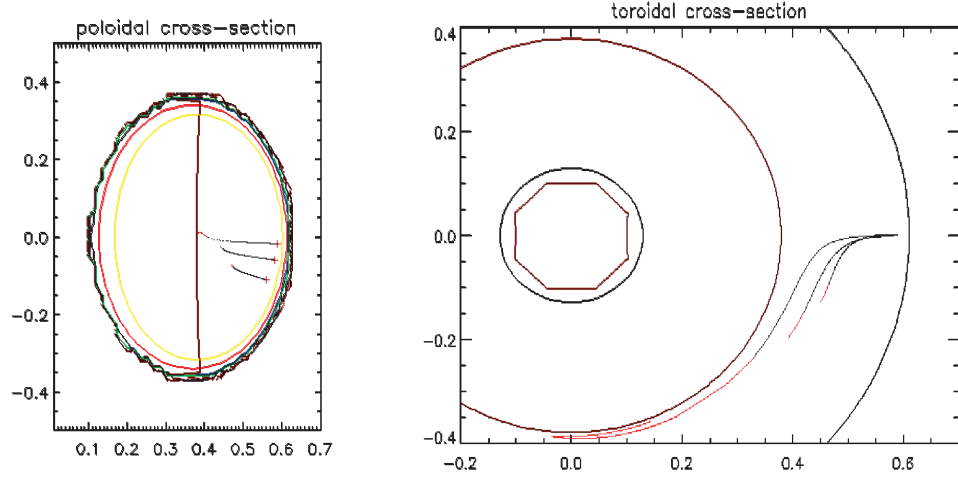
$$\frac{dW}{dt} = -2\gamma W, \tag{3.69}$$

Figure 3.8: Trajectory of 8.2 GHz EBW starting from different toroidal angles under the nearly perpendicular incidence condition ($n_\parallel = 0.01$) on the poloidal cross section (left) and the toroidal cross section (right). $T_e = 400\,eV$, $n_e = 1 \times 10^{19}\,\mathrm{m}^{-3}$, and parabolic profiles are assumed. Fundamental ECR layer is located near the magnetic axis. .

where W is the energy of the EBW. Expanding D in the small imaginary part of frequency γ, D becomes

$$D(\boldsymbol{r}, \boldsymbol{k}, \omega + i\gamma) = D(\boldsymbol{r}, \boldsymbol{k}, \omega) + i\gamma \frac{\partial D(\boldsymbol{r}, \boldsymbol{k}, \omega)}{\partial \omega} = 0. \qquad (3.70)$$

Using the real and imaginary parts of D, γ is evaluated as

$$\gamma = \frac{\mathrm{Im}(\mathrm{D}(\mathrm{r}, \mathrm{k}, \omega))}{\partial \mathrm{Re}(\mathrm{D}(\mathrm{r}, \mathrm{k}, \omega))/\partial \omega}, \qquad (3.71)$$

without directly calculating the dispersion relation for complex frequency.

In Fig. 3.8, an example of ray tracing is shown. It can be seen that the EBW launched near the mid-plane propagates to the vicinity of the cyclotron resonance, while the wave launched away from the mid-plane is damped far away from the resonance. This is the effect of $k_\parallel$ up-shift. As $k_\parallel$ increases during propagation, the wave sees a greater Doppler shift. The figure also shows that the EBW propagates perpendicularly to the magnetic surface near the UHR and, as it propagates deeper into the core region, it changes direction and propagates nearly in the toroidal direction when it is absorbed. This feature is considered attractive for driving the plasma current. Figure 3.9 shows four ray trajectories having different initial $k_\parallel$ and poloidal angle.
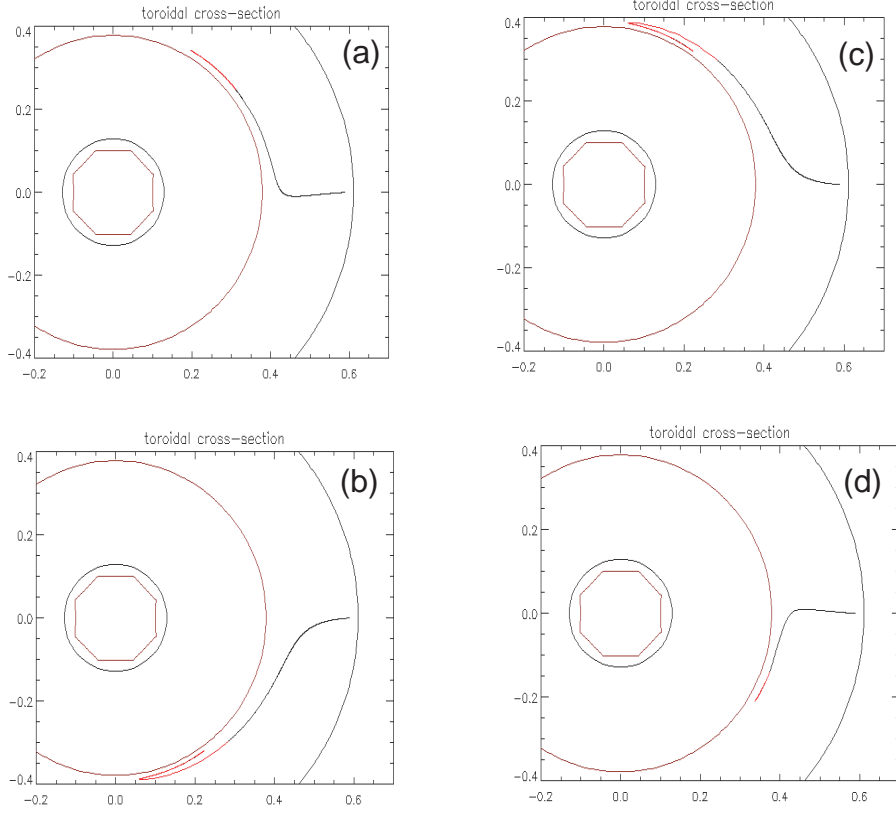
Figure 3.9: Effects of the initial $n_\parallel$ and the poloidal angle on the ray trajectory. Trajectories of EBW launched (a) with $n_\parallel = 0.4$ and from 3cm above the mid-plane, (b) with $n_\parallel = 0.4$ and from 3cm below the mid-plane, (c) with $n_\parallel = -0.4$ and from 3cm above the mid-plane, and (d) with $n_\parallel = -0.4$ and from 3cm below the mid-plane, respectively. Equilibrium is assumed to be same as Fig. 3.8.

Compared with the trajectories starting near the mid-plane shown in Fig. 3.8, the toroidal direction of propagation reverses by changing the poloidal angle from above to below the mid-plane, while the initial $k_\parallel$ have a smaller effect on the trajectory.

3.7 EBW near the cyclotron resonance

In the previous section, it is shown that the EBW is absorbed by the electron cyclotron damping when the EBW is excited away from the mid-plane of the torus. The non-relativistic dispersion relation used in the calculation is sufficient for such a trajectory. However, when the wave is launched near the mid-plane, the EBW propagates to the immediate vicinity of the electron cyclotron resonance.

As mentioned at the end of Sec. 3.4, in order to understand the behavior of the EBW near the cyclotron resonance, the relativistic effect must be considered. This effect changes the mass and adds a correction to the particle gyration frequency depending on its momentum ($\Omega_{\mathrm{ce}} = \frac{eB_0}{mc} \rightarrow \frac{eB_0}{\gamma mc}$, where $\gamma = (1 - p^2/m^2c^2)^{1/2}$). Because the change of mass is proportional to $\sqrt{1 - v^2/c^2} - 1 \sim v^2/2c^2$, the relativistic absorption spreads in the width of

$$\left| \frac{\omega - n\Omega_{\mathrm{ce}}}{\omega} \right| \leq \frac{v_{\mathrm{th}}^2}{2c^2}, \tag{3.72}$$

which determines the domain where the relativistic effect is important.

A general form of the xx component of the relativistic susceptibility of electrons with the relativistic Maxwell distribution is

$$\chi_{\mathrm{xx}}(\mathbf{k}, \omega) = -\frac{\omega_{\mathrm{pe}}^2}{\omega^2} \frac{\mu_r}{2K_2(\mu_r)} \int_0^\infty \bar{p}_\perp d\bar{p}_\perp \int_{-\infty}^\infty d\bar{p}_\parallel \sum_{n=-\infty}^\infty \frac{\bar{p}_\perp^2 \frac{n^2}{\nu_\perp^2 \bar{p}_\perp^2} J_n^2(\nu_\perp \bar{p}_\perp)}{\gamma - n_\parallel \bar{p}_\parallel - n(\Omega_{\mathrm{c}}/\omega)}, \tag{3.73}$$

where $\mu_r = 2\frac{c^2}{v_{\mathrm{th}}^2}$, $\nu_\perp = n_\perp \frac{\omega}{\Omega_{\mathrm{ce}}}$, $\bar{p}_\perp = p_\perp/mc$ and $\bar{p}_\parallel = p_\parallel/mc$ are normalized momenta, and $K_2(\mu_r)$ is the modified Bessel function. Though this formula resembles Eq. 3.21 for the classical case, the existence of γ in the denominator makes the momentum space integration more difficult. In the analysis of electron cyclotron waves, the finite Larmor radius (FLR) expansion assuming a small λ is commonly used, which turns the dispersion relationship into a polynomial function. However, in the EBW case, $\lambda \ll 1$ is generally not satisfied and the integration must be carried out numerically.

A quick way to see how the EBW behaves near the ECR is to use an approximation of the relativistic correction to Ω_{ce} as $\Delta\Omega_{\mathrm{ce}} = v_{\mathrm{th}}^2/c^2\Omega_{\mathrm{ce}}$. The

starting point is the non-relativistic dispersion relationship, Eq. 3.42. Remembering $e^{-\lambda}I_n(\lambda) \sim \frac{(\lambda/2)^n}{n!}$, we dropped all terms except $|n| = 1$, yielding the real part of the wave vector of

$$k_\perp = \left\{ \frac{4}{\sqrt{\pi}} \frac{\Omega_{ce}^3}{v_{th}^3} \frac{\omega_{pe}^2}{\omega^2 - (\Omega_{ce} - \Delta\Omega_{ce})^2} \right\}^{1/3}. \tag{3.74}$$

To estimate the strength of absorption, we replace the plasma dispersion function in Eq. 3.41 by its relativistic counterpart, which is a family of relativistic dispersion functions, or Shkarofsky functions $\mathcal{F}_{n/2}$. All Shkarofsky functions have the following asymptotic relationship with the non-relativistic plasma dispersion function,

$$\mu_r \mathcal{F}_{n/2} \sim -\zeta_0 Z_0(\zeta_n). \tag{3.75}$$

In the $k_\parallel = 0$ limit, the Shkarofsky function reduces to the simpler Dnestrovsky function, $F_{n/2}$, which is defined as

$$F_{n/2} = -i \int_0^\infty dt \frac{e^{izt}}{(1 - it)^{n/2}} \tag{3.76}$$

Though there is an ambiguity of choosing n, observing that the leading order term in the FLR expansion is $\mu_r F_{5/2}$ for n=1, we replace the $n = 1$ term by $F_{5/2}$ and take only the $|n| = 1$ terms, yielding an equation for $k_\perp$,

$$k_\perp = \left[\frac{2}{\sqrt{\pi}} \frac{\Omega_{ce}\omega_{pe}^2}{v_{th}^3} \left\{ \mu_r F_{5/2} \left(2\frac{c^2}{v_{th}^2} \frac{\omega - \Omega_{ce}}{\omega} \right) - \frac{3}{2} \right\} \right]^{1/3}. \tag{3.77}$$

Figure 3.10 shows the wave vector near the fundamental cyclotron resonance given by Eq. 3.74 and Eq. 3.77. The electron temperature of $100\,\mathrm{eV}$, the density of $1 \times 10^{19}\,\mathrm{m}^{-3}$, and the magnetic field of $0.3\,\mathrm{T}$ are assumed in the calculation, which are typical plasma parameters in the EBW heating experiments carried out on TST-2@K. As expected for an electrostatic wave, the wave vector is large, but does not diverge. The absorption $(\mathrm{Im}(\mathrm{k}_\perp) < 0)$ takes place only on the high field side of the resonance. It is because the gyration frequency decreases from the classical cyclotron frequency. The absorption is very strong $|\mathrm{Im}(\mathrm{k}_\perp)| \sim |\mathrm{Re}(\mathrm{k}_\perp)|$. In the TST-2 geometry, ω/Ω_{ce} of 0.01 corresponds to $\sim 0.4\,mm$, while $\mathrm{Im}(\mathrm{k}_\perp)$ of $1 \times 10^5 m^{-1}$ corresponds to e-folding length of $\sim 0.06\,\mathrm{mm}$. Accordingly, the EBW coming from the low field side (right of the graph) is expected be absorbed abruptly when it reaches the resonance. A more accurate analysis starting from Vlasov equation [80] showed that the function that takes the place of $-\zeta_0 Z_0(\zeta_n)$ is not
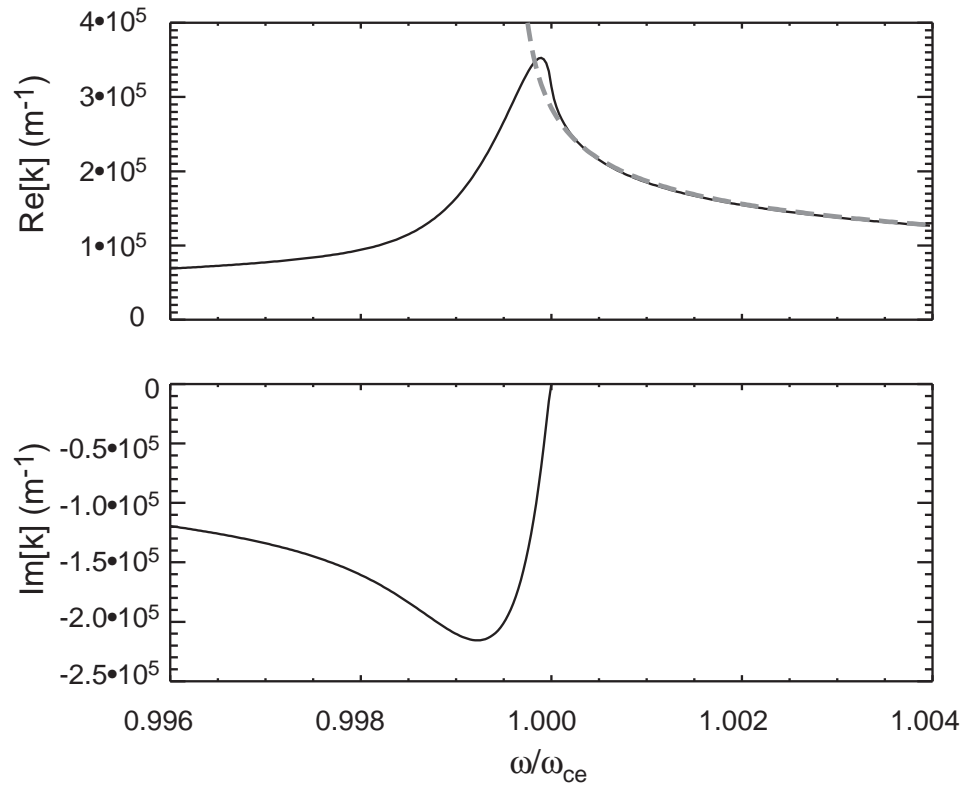
Figure 3.10: The dispersion relationship described by Eq. 3.77 (solid line) , and the real part of $k_\perp$ evaluated by Eq. 3.74 (dashed line)
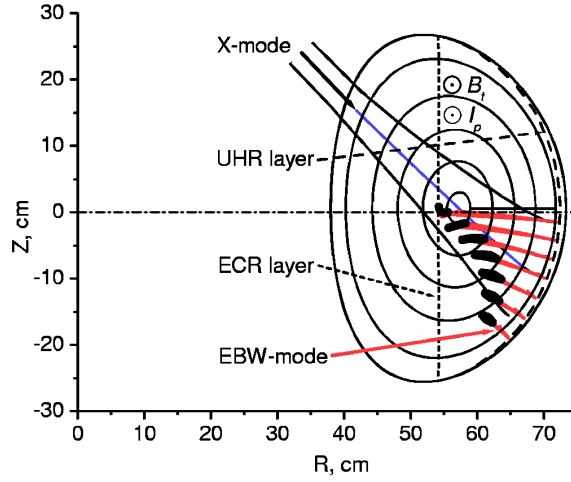
Figure 3.11: An experimental configuration of the X-mode injection from the high magnetic field side of the torus [7].

$F_{5/2}$ but F_2 but the rest of Eq. 3.77 does not change, yielding a quite similar result.

This strong absorption means that the EBW radiation is suitable for a local electron temperature diagnostic. It is known that when the optical thickness exceeds unity, the radiation can be considered as black body emission. In Ref. [11], the optical thickness is calculated to be 300 to 3000 for typical ST plasma parameters.

3.8   Related research on EBW and MC

3.8.1   Other MC scenarios

High field side incidence X-B scenario

When the density is not too high, and when there is no high density X-mode cutoff layer in the plasma, the UHR layer is accessible from the high density side. In such a circumstance, the X-mode EC wave can be launched from the inboard side of the torus, propagate to the UHR layer, and mode convert to the EBW, as shown in Fig. 3.11. This scenario has been tested on a tokamak in which density cannot be raised as easily as in a stellarator [7, 8]. This scenario may be applied to a very early, low density phase of an ST discharge. In fact, such experimental plan is being proposed on MAST [81].
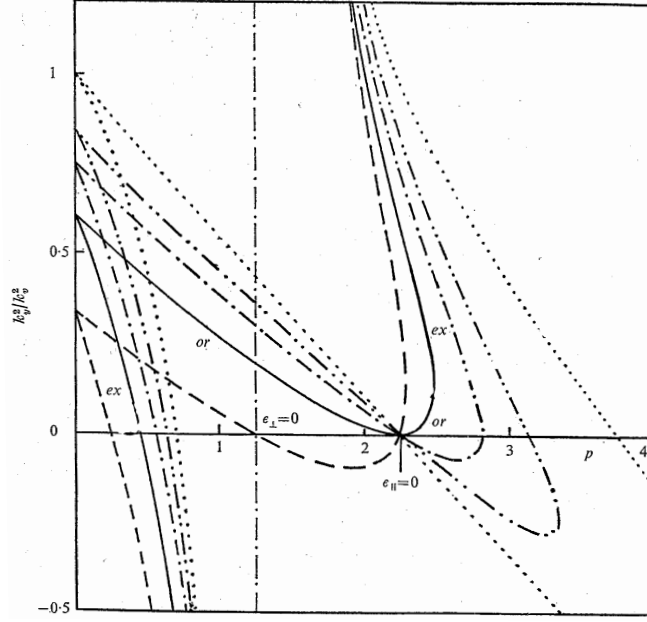
Figure 3.12: Square of the dimensionless wave vector component parallel to the density gradient (k_y^2/k_v^2) as a function of the dimensionless density $(\omega_{pe}^2(y)/\Omega_{ce}^2)$, for $\omega = 1.5\Omega_{ce}$. Curves corresponding to the angles of incidence (γ) of $\sin\gamma = 0$, 0.16, 0.25, 0.4, and 0.66 are plotted [82].

O-X-B scenario

The O-X-B MC scenario was first proposed by Preinhaelter [82]. This MC process requires an optimal parallel component $n_{opt\parallel}$ of the refractive index n, or equivalently, an oblique optimal launch angle ϕ with respect to the magnetic field line. This condition is expressed as

$$n_{opt\parallel} = \frac{\Omega_{ce}}{\Omega_{ce} + \omega_{pe}}, \tag{3.78}$$

which is equivalent to the condition for the X-mode high density cutoff and the O-mode cutoff to coincide spatially. The spatial profiles of k_y, the wave vector component parallel to the density gradient, in a 1-D stratified plasma for various angles of incidence are shown in Fig. 3.12. The solid line in the figure corresponds to the case when the above condition is met, in which the O-mode (denoted by *or* in the figure) on the low density side connects to the mode on the high density side at the cutoff. At other angles of incidence, the figure shows that there is an evanescent region between the modes on the low and high density sides. Note that there is another point where two modes
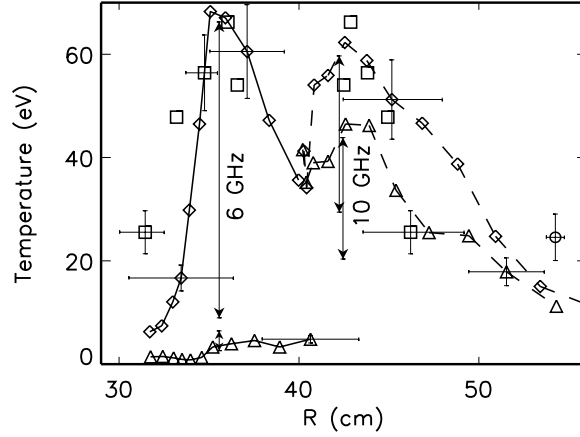
Figure 3.13: The radiation temperature without the local limiter (triangles) and with the local limiter for fundamental emission (diamond, solid line) and second harmonic emission (diamond, dashed line), electron temperature profile measured by Thomson scattering (squares) and Langmuir probe (circle) [19]

.

coalesce. As the O-mode on the high density side propagates deeper into the plasma, it connects to the X-mode (denoted by *ex* in the figure) and travels back to the upper hybrid resonance layer. Preinhaelter examined a full-wave equation near the two connection points using the phase integral method [83] and found that the wave power can be transferred to the other mode without reflection [82]. Since there are two points where different modes coalesce and the wave power is transferred by MC, this scenario is sometimes called "double mode-conversion". This scenario has been tested on stellarators [9, 10, 84] and is planned to be used on ST [85].

3.8.2   Other EBW expereiments on ST

On STs, because of the relatively low magnetic field, the high density X-mode cutoff exists in the plasma and the high field side X-mode injection is not applicable. So far, there has been no report of heating or current drive experiments on ST, except for ours.

A couple of low power EBW receiving experiments have been carried out on STs. Of these experiments, the measurement of T_{rad} carried out on CDX-U [11, 19, 86], is most deeply related to the present research. The author had a chance to participate in this experiment through the US-Japan ex-

change program. A representative result of the CDX-U experiment is shown in Fig. 3.13. The X-mode emission perpendicular to the magnetic surface is measured by a radiometer that covers the fundamental and the second harmonic frequencies. Initially, the CDX-U radiometer measured very low T_{rad} compared to T_{e} measured by Thomson scattering. After installation of a local limiter around the receiving antenna to steepen the density gradient in front of the antenna, the emission became much more intense and the upper envelope of the fluctuating T_{rad} was found to be comparative to T_{e}. These results indicate that by steepening the density gradient in the MC region, the MC efficiency was improved and became nearly 100 % as expected for the triplet MC scenario described in Sec. 3.5.5. Large fluctuations on T_{rad} is considered to result from fluctuations of the MC efficiency caused by density fluctuations in the edge plasma.

The EBW emission diagnostic is also operated on larger STs, MAST and NSTX. In fusion plasmas, a spontaneous improvement in plasma confinement is often observed. It is called the H-mode or the edge transport barrier, when the improvement occurs at the plasma edge [31]. On both MAST and NSTX, increases of EBW emission at transitions to the H-mode were reported [87], indicating that the steepened density gradient found in H-mode improves EBW MC efficiency. The toroidal magnetic field and the corresponding Ω_{ce} are higher in larger spherical tokamaks. The density scale length desired for good X-B MC is shorter. Rather than creating such an extremely steep density gradient, by choosing appropriate polarization and antenna angle with respect to the magnetic surface, MC can be improved for the naturally occurring density gradient. It is noted that the H-mode edge density profile is suitable for O-X-B MC heating than L-mode [87]. On NSTX, in order to characterize the EBW emission generated by O-X-B MC, radiometers having antennas aligned at oblique angles to the magnetic field were used [88]. The radiometers have recently been upgraded to enable steering of the antenna [89]. Detailed comparisons with theoretical predictions, such as the n_{toroidal} and n_{poloidal} dependences of the MC efficiency and the amplitudes of the two linearly polarized emissions are reported.

3.8.3 Experiments in configurations other than ST

On conventional aspect ratio tokamaks and stellarators, diagnosis, heating and current drive using the EBW have been demonstrated. Pioneering experiments of diagnosis [10] and heating [84], based on the O-X-B MC scenario, were performed on the Wenderstein-7AS stellarator by Laqua in 1990s. Emission and heating experiments were reported in detail in Ref. [90]. When the density measured by microwave interferometry and Thomson scattering
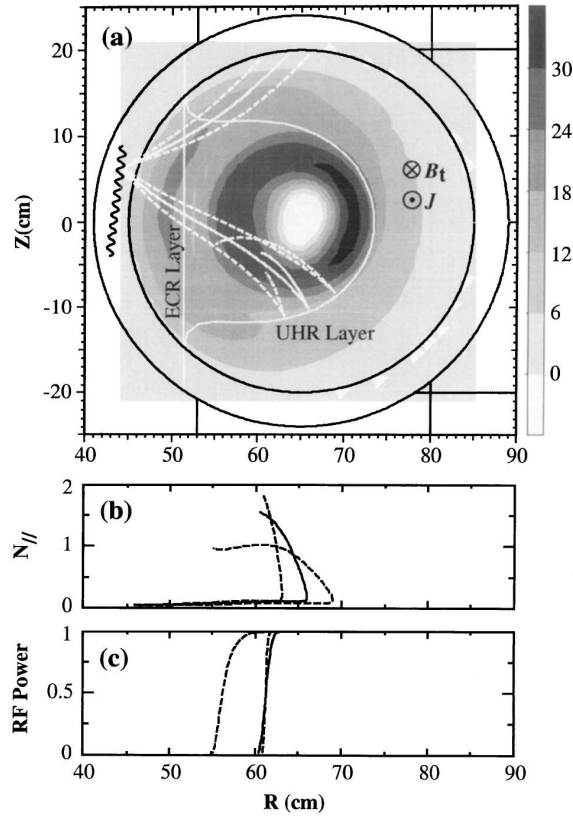
Figure 3.14: High field side X-mode injection experiment carried out on the WT-3 tokamak. (a) Incremental soft X-ray tomography image at the onset of EBW heating shows the location of absorption. (b) $n_\parallel$, and (c) wave power along the ray trajectory [8].
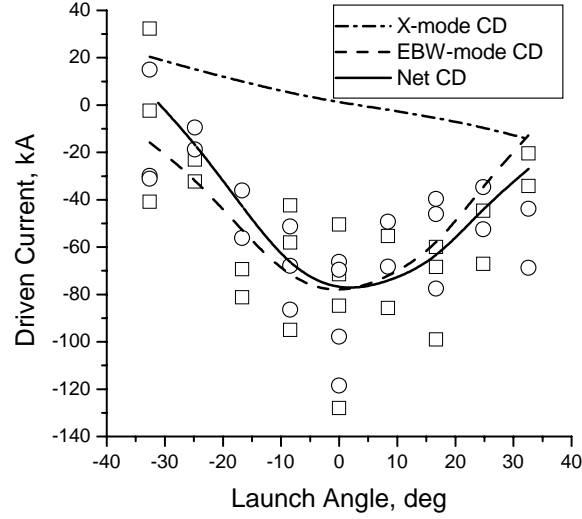
Figure 3.15: Noninductive current driven in the plasma estimated from experimental data, and calculated current driven by the X-mode, the EBW, and both waves [7].

exceeded the cutoff densities of the emitting frequency, EBW emission was detected by a radiometer placed at an optimal angle for O-X-B MC. Scans of the viewing angle showed that the EBW emission is significant at expected optimal angles, and the radiation temperature was about $60 - 70\,\%$ of the line-averaged temperature measured by soft X-ray emission. A microwave power of $220\,\mathrm{kW}$ at $70\,\mathrm{GHz}$ was injected to an NBI sustained plasma with a central density of $1.6\times10^{16}\,\mathrm{m}^{-3}$. It was also reported that parametric instability was observed during EBW heating and that the high frequency part of EBW emission spectrum was affected by non-local "hohlarum" radiation. Recently, current drive was also demonstrated by the same author [9]. The obtained dimensionless current drive efficiency, which normalizes the driven current using RF power, density, temperature, and major radius, exceeded that for standard ECCD by a factor of 2–3.

On the WT-3 tokamak, $100\,\mathrm{kW}$ of power was injected in the X-mode from the high field side of the torus toward an isolated (having no cutoff in its vicinity) UHR layer [8]. A clear plasma heating was observed. As shown in Fig. 3.14, it is found that the EBW was absorbed at neither the electron cyclotron resonance layer nor the UHR layer, but between them. This is consistent with the displacement of the power deposition profile caused by the $n_\parallel$ up-shift of the EBW. The X-mode injection from the high field side was also employed in current drive experiments conducted on the COMPASS-D

tokamak [7]. By scanning the launch angle, it was found that the loop volt-
age drop showed no obvious dependence on the launch angle, although the
temperature increment was double (from 1.5 keV to 3.5 keV) for perpendic-
ular injection compared to the largest launch angle. The loop voltage drop
itself was smaller than that expected from the temperature increase due to
RF injection. This unexpectedly high loop voltage was attributed to counter
current drive by EBW, and the launch angle dependence of the driven cur-
rent was consistent with the calculation using a combined ray-tracing and
Fokker-Planck code (Fig. 3.15).

Reverse field pinch (RFP) is another MFE configuration, in which plasma
is mostly overdense, and the propagation and absorption of EBW in RFP
plasma has characteristics similar to that in an ST plasma [91]. EBW emis-
sion was measured on the Madison Symmetric Torus (MST) RFP, and it was
concluded that the measured emission was caused by the X-B process [92].
Current EBW research on MST is emphasizing the improvement of plasma-
antenna coupling of a phased array antenna. EBW coupling study using the
antenna, consisting of two adjacent waveguides whose relative phase was con-
trollable, reported that the observed coupling to vacuum is consistent with
theoretical calculation, and coupling to plasma reproduced the characteristic
features predicted from a theory [93, 94]. Experiments at moderate to high
power using a more sophisticated phased array antenna are about to begin
[95].

3.8.4 Theoretical works specific to fusion application

As heating and current drive of ST plasmas are envisaged, many theoretical
works on MC, propagation, and absorption of the EBW have been carried
out. In the MC process, finite temperature effects become important when
the wave frequency is near harmonics of the local cyclotron frequency ($n\Omega_{\mathrm{ce}}$,
$n > 2$). While the usual MC theory uses a 4th order model differential
equation, having incoming and outgoing waves of the two modes as a solution,
the inclusion of finite temperature effect to EBW MC occurring at the plasma
edge needs to handle at least a 6th order equation. It is because both QT-X
and QT-O modes contribute to the MC to EBW. A numerical investigation
of EBW MC using such a 6th order differential equation is reported by Ram
[96]. Ram included the most important modification to χ_{xx},

$$\chi_{\mathrm{xx}} = \chi_{\mathrm{xx}} + \frac{-3\omega_{\mathrm{pe}}^2\omega^2}{(\omega^2 - \omega_{\mathrm{ce}}^2)(\omega^2 - 4\omega_{\mathrm{ce}}^2)}\frac{v_{\mathrm{th}}^2}{c^2} \tag{3.79}$$

It was also reported there that the resonance absorption model is consistent
with the kinetic model when the wave frequency is well away from $n\Omega_{\mathrm{ce}}$,

justifying the usage of the model in this research.

Techniques to improve the MC efficiency have been proposed. Polarization control of the injected electromagnetic wave can be used to enhance the MC efficiency. Extensive numerical analyses of such a possibility were reporeted in Ref. [97]. Direct coupling of the EBW with a waveguide antenna was investigated [98], and used in the calculation of coupling of the phased array antenna used in MST [99].

As for propagation and absorption of the EBW, effects that cannot be included properly in the WKB analysis, and relativistic effects have been investigated. When a magnetic well exists in the plasma, which is expected in a high beta ST plasma, the EBW launched from the low magnetic field side of the torus may approach the ECR layer from the high magnetic field side. Propagation and absorption in such a situation were studied in Ref. [100, 101]. As shown in Fig. 3.8, the wave launched near the midplane has the deepest penetration into the plasma, and therefore, is of special interest for heating and current drive. It is reported that the EBW shows different characters depending on whether the ECR layer has concave surface or convex surface [102]. Relativistic effects on EBW are also investigated by several authors [101, 103].

In addition, prospects of plasma heating and current drive using parameters specific to a large ST have been reported. In Ref. [85], plasma heating on MAST using the fundamental and the 4th harmonic resonance based on the O-X-B MC scenario was investigated. EBW was anticipated to play an important role in sustaining the high β plasma non-inductively. In scenario development on NSTX, using an extensive set of computer codes such as the Tokamak Simulation Code [104], it was reported that an off-axis current drive of about $100\,\mathrm{kA}$ driven by EBW is necessary for a full non-inductive sustainment of the plasma with $I_{\mathrm{p}} = 1.0\,\mathrm{MA}$, $B_{\mathrm{t}}=0.35\,\mathrm{T}$, $\kappa \sim 2.5$, $\beta_{\mathrm{N}} \le 9$ and $\beta \le 40\,\%$ [105].

3.8.5 EBW in astrophysics

The EBW is not specific to fusion, and is widely observed in astrophysics. The EBW and its MC to an electromagnetic wave are discussed in research involving solar flare plasmas and ionospheric plasmas.

In Ref. [106], EBW emitted during magnetic reconnection and its MC to electromagnetic waves is considered to be the mechanism of the RF wave bursts observed in the solar flare. In ionospheric modification experiments [107, 108, 109], a powerful high frequency electromagnetic (EM) wave in the electron cyclotron frequency range is launched from the ground, and stimulated a secondary EM emission (SEE) in the sidebands of the reflected

primary wave. The spectrum of the SEE has several specific features, and MC of the EM wave to the EBW, and parametric decay instability (PDI) of these waves are discussed in the explanation of the observed SEE spectrum [110, 111, 112]. Such nonlinear damping is also expected in high power heating of fusion plasmas. In fact, an observation of the side band wave in the WA-7S stellarator was reported already (Ref. [90]). However, experiments on fusion plasmas are presently very limited, and a further investigation is necessary to understand the role of PDI on EBW heating and current drive.

Chapter 4

TST-2 spherical tokamak

This chapter addresses the physics and engineering issues relating to the construction of TST-2 and its plasma operation. After presenting the reasons for constructing a completely new device, plasma parameters required for this device are desicribed. In order to develope plasma operational scenarios, understanding and cancellation of eddy currents induced on the vacuum vessel were crucial. These are described in detail. Finally, plasma parameters achieved in this device are compared with design values.

4.1   Necessity of a new ST device

The spherical tokamak in operation at the University of Tokyo was Tokyo Spherical Tokamak - Modified (TST-M), when RF research was chosen as the major research topic. As shown in Fig. 4.1, the plasma current was $< 60\,\mathrm{kA}$ and the discharge duration was $1-7\,\mathrm{ms}$. Plasma parameters of such plasmas are typically electron density of $\sim 1 \times 10^{19}\,\mathrm{m^{-3}}$ and electron temperature of $30-70$ eV. Higher plasma currents ($I_\mathrm{p} \sim 100kA$) were also obtained but only extremely transiently. These parameters are insufficient for plasma heating experiments by any kind of radio-frequency (RF) wave. Consequently, a new ST device TST-2 was constructed.

Figure 4.2 shows a comparison of cross sections of TST-M and TST-2. Achieved parameters of the two devices are listed in Table. 4.1. Two devices have vacuum vessels of similar radii and heights. Since it was unlikely to expand the capabilities of our power supplies greatly, it was not a good idea to choose a larger plasma size. A smaller plasma was avoided since a poorer plasma confinement is expected. Though similar major and minor radii (R and a, respectively) were chosen, significant improvements on plasma parameters were achieved on TST-2 as is evident from the table.
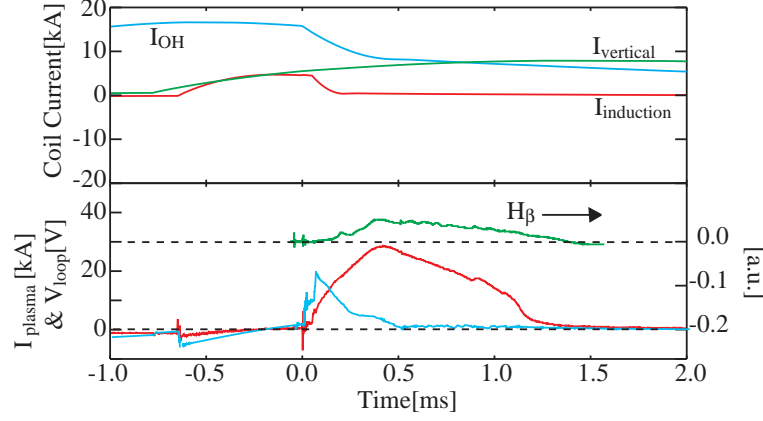
Figure 4.1: Typical coil currents and plasma current of TST-M.

Table 4.1: Comparison of achieved parameters between TST-M and TST-2.

	TST-M	TST-2
Geometry.		
R [m]	0.36	0.38
a [m]	0.28	0.25
A	1.3 - 2.5	>1.5
κ	1.0 - 1.5	$1.2 - 1.8$
Magnets		
B_{t} [T]	0.2	0.3
Ψ_{OH} [mVs]	25	130
Parameters		
I_{p} [kA]	60^1	140
$\tau_{\mathrm{discharge}}$ [ms]	$1 - 7$	50
n_{e} $[\times 10^{19} \mathrm{m}^{-3}]$	$1 - 2$	$1 - 2$
T_{e0} [eV]	$30 - 70$	$300 - 400$
T_{i0} [eV]		$50 - 100$
τ_{E} [ms]	not measured	$1 - 3$

[1] a transiently obtained high plasma current
is excluded.

stray field cancellation coils

C̷L

center stack
(OH coil + TF center legs)
stray field cancellation coils

PF1

PF2

PF4

PF5

PF3

Induction
Coils

TF coil

TF coil

equilibrium field coil

equilibrium field coils
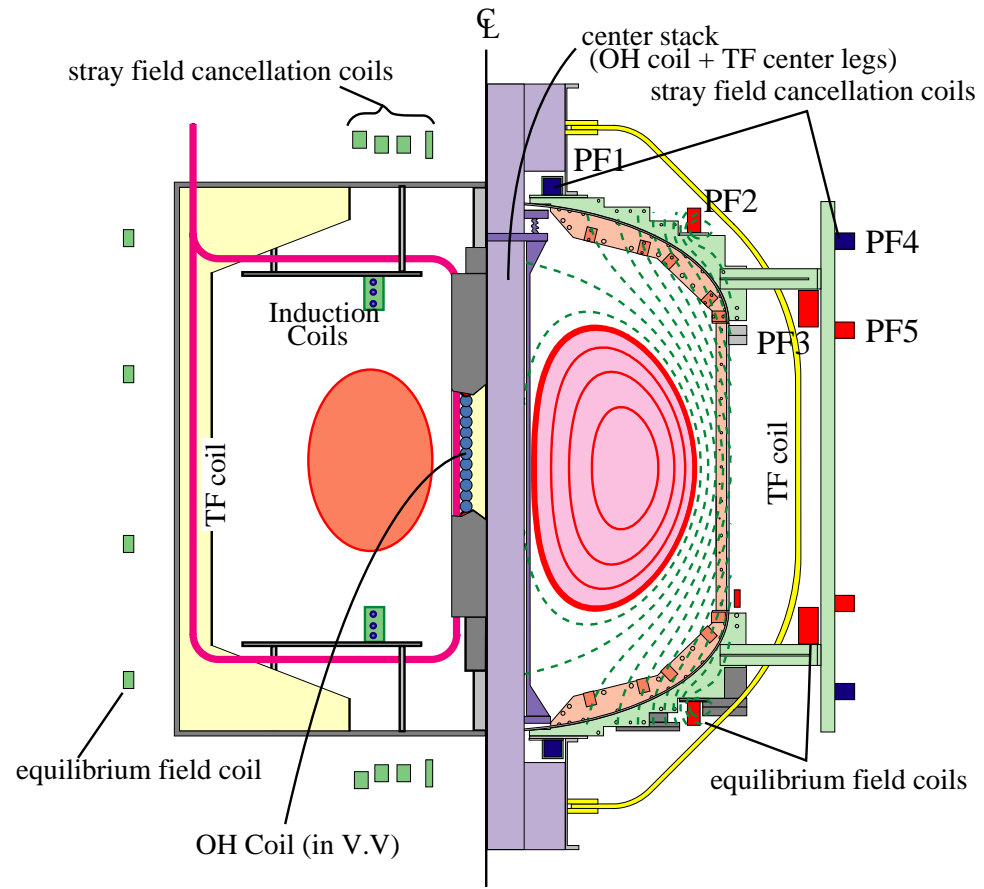
OH Coil (in V.V)

Figure 4.2: Poloidal cross sections of TST-M (left) and TST-2 (right).

4.2   Determination of design parameters

To start a design of a new device, it is necessary to evaluate the plasma parameters required for planned experiments. In case of TST-2, RF heating experiments required that 1) the plasma should absorb the excited RF wave efficiently, and that 2) the plasma should be sustained long enough for heating effects to be confirmed.

4.2.1   Requirements for T_e and n_e

Since EBW is expected to be absorbed efficiently even by a rather low temperature plasma, the requirement for plasma parameters is not so severe. On the other hand, absorption of the high harmonic fast wave (HHFW), which is a fast wave in the frequency range of $5 \sim 20\Omega_{ci}$, puts distinct requirements on T_e and n_e. Using the dispersion relationship described in Ref. [3], the absorption of HHFW was surveyed. The dependence on the initial parallel wave number is shown in Fig. 4.3 for a plasma with electron and ion temperature of $T_e = 200\,\mathrm{eV}$ and $T_i = 100\,\mathrm{eV}$, density of $n_e = 2 \times 10^{19}\,\mathrm{m}^{-3}$, and toroidal magnetic field of $B_t = 0.2\,\mathrm{T}$. Since transit time magnetic pumping (TTMP, denoted as MP in the figure) overcomes the cross term (X in the figure), which cancel each other in the low β regime, the net absorption is calculated to be twice larger than that expected from Landau damping alone.

In Fig. 4.4, the variation of the wavenumber across the plasma is calculated assuming gaussian radial profiles for the density and the temperature. The power absorbed during one pass through the plasma, from the outboard edge to the center to the inboard edge, is called single-pass absorption, and is evaluated by integrating the imargnary part across the plasma profile. For this case, the single-pass absorption efficiency is 40%, as shown in frame (e). It is also found that nearly 100% absorption is inferred if the magnetic field is reduced to a half, though such a plasma may be unstable. This calculation does not include the effects of boundary condition and two dimensional effects. Though quantitative accuracy is rather limited due to this reason, based on a comparison with analysis using a full-wave code, a temperature of $200\,\mathrm{eV}$ and a density of $2 \times 10^{19}\,\mathrm{m}^{-3}$ are necessary for HHFW heating experiments.

4.2.2   Empirical scaling laws

The energy confinement time is a characteristic time scale for which the plasma kinetic stored energy W_K changes when the input power changes. To see the effects of plasma heating on the stored energy, the plasma needs to
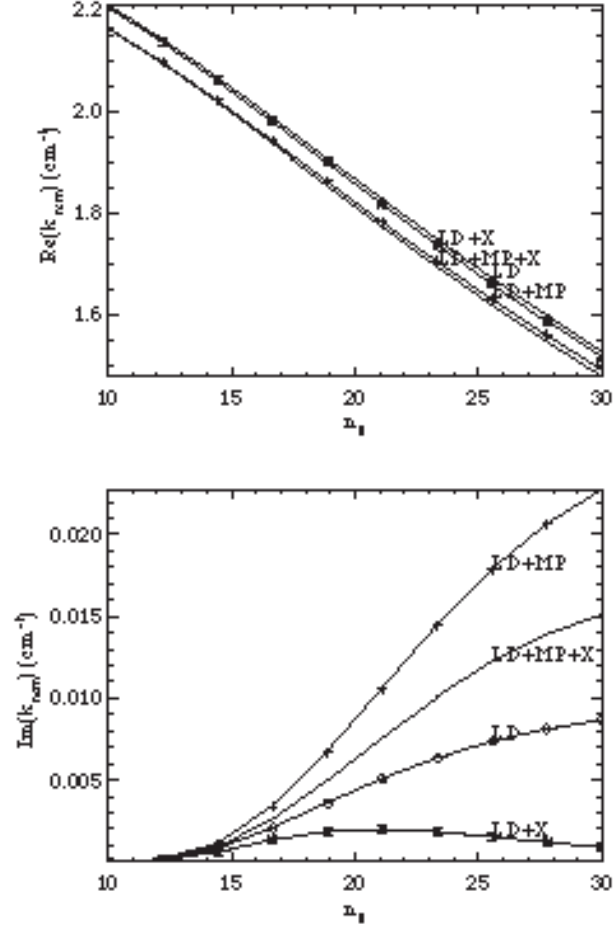
Figure 4.3: Dependence of real and imaginary parts of HHFW wavenumber on $n_\parallel$. $T_e = 200\,\text{eV}$, $T_i = 100\,\text{eV}$, $n_e = 2 \times 10^{19}\,\text{m}^{-3}$, and $B_t = 0.2\,\text{T}$ are assumed, and ion cyclotron damping is neglected.
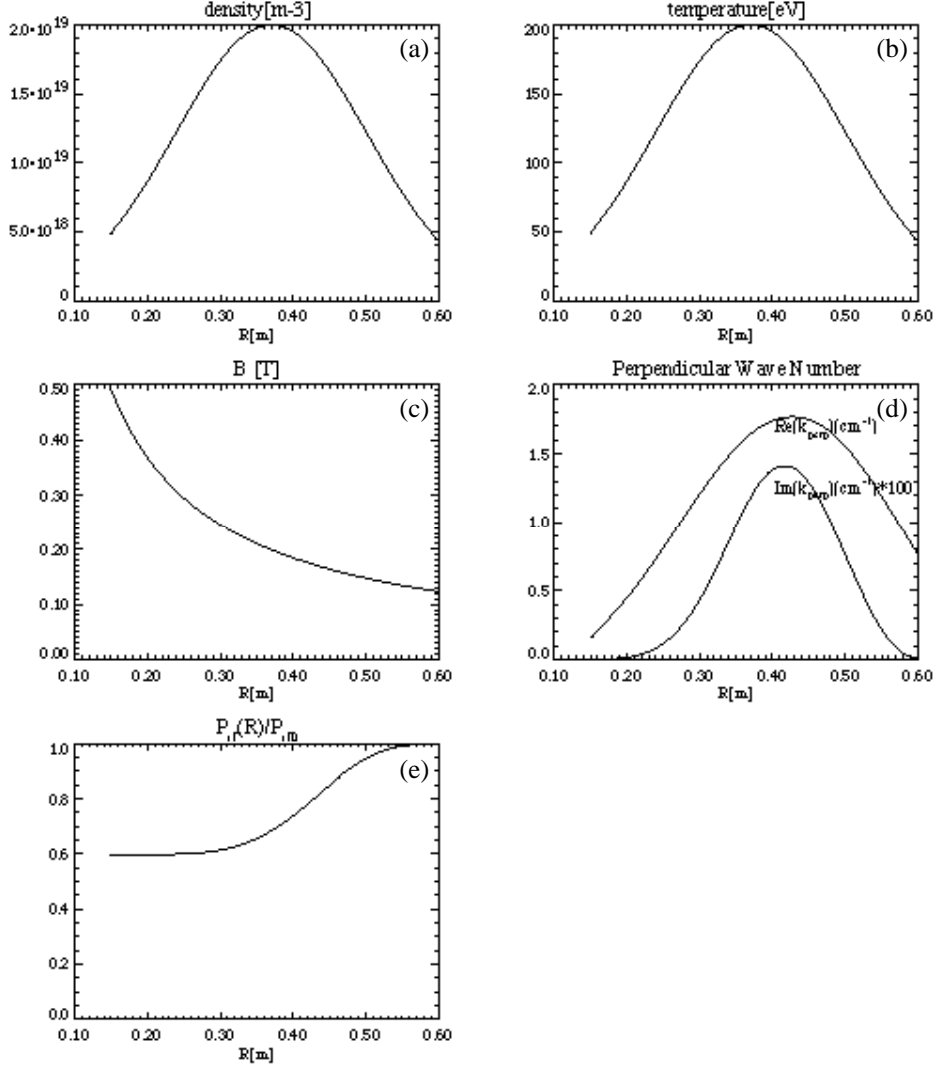
Figure 4.4: Single-pass absorption calculation. (a) Density profile, (b) electron temperature profile, (c) magnetic field profile, (d) real and imaginary parts of wavenumber, (e) fraction of power remaining in the wave. Central parameters are the same as Fig. 4.3.
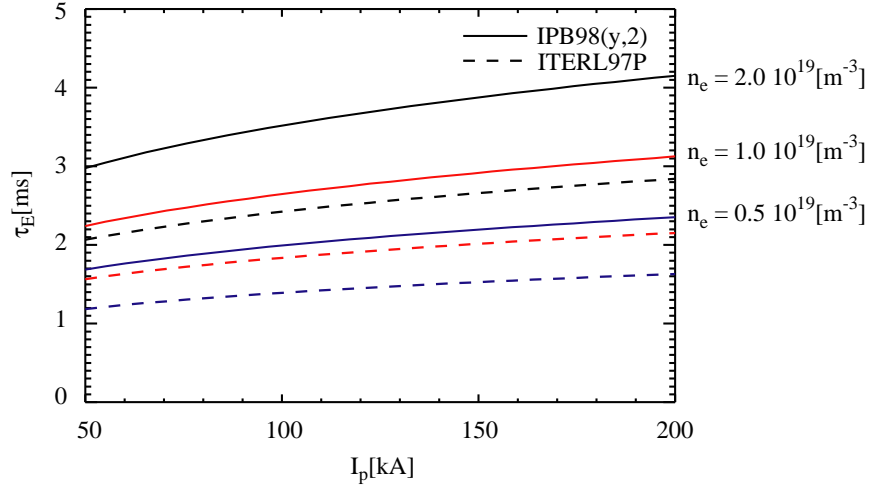
Figure 4.5: Calculations of τ_{E} based on the IPB98(y,2) (solid lines) and the ITERL97P (dashed lines) scaling laws. Black, red, and blue lines correspond to n_{e} of 2.0, 1.0, and $0.5 \times 10^{19}\,\mathrm{m^{-3}}$, respectively.

be sustained for sufficiently longer than the energy confinement time. The energy confinement time was evaluated using empirical scaling laws based on the data from conventional aspect ratio tokamaks. The ITERL97P L-mode scaling[35] predicts the confinement time as

$$\tau_{\mathrm{E}}^{\mathrm{ITERL97P}} = 0.023\, I_{\mathrm{p}}^{0.96} B_{\mathrm{T}}^{0.03} P^{-0.73} n_{19}^{0.40} M^{0.20} R^{1.83}, \epsilon^{0.06} \kappa^{0.64} \tag{4.1}$$

while the H-mode scaling according to the ITER physics basis [36] predicts somewhat longer τ_{E}

$$\tau_{\mathrm{E}}^{\mathrm{IPB98(y,2)}} = 0.0562\, I_{\mathrm{p}}^{0.93} B_{\mathrm{T}}^{0.15} P^{-0.69} n_{19}^{0.41} M^{0.19} R^{1.97} \epsilon^{0.58} \kappa_{\mathrm{a}}^{0}.78 \tag{4.2}$$

where $\kappa_a = S/\pi a^2$, S is the cross sectional area, and M is the average ion mass in units of the proton mass. In these equations, R is the major radius of the geometrical center of the torus, and B is the magnetic field at the geometrical center. Both scaling lows have strong dependence on I_{p} and are quite weakly dependent on B_{t}. Though the applicability of these scaling laws to Ohmically heated ST plasmas produced in TST-2 are questionable, given the lack of a more reliable prediction, these scaling laws were used as upper and lower bounds of τ_{E}. The calculated τ_{E} for the range of I_{p} is shown in Fig. 4.5. It is found that τ_{E} is in the range of 1–4 ms, and consequently, a flat-top (stationary phase) of 10–20 ms is necessary for heating experiments.

An Ohmically heated plasma needs to be heated to a target T_e by Ohmic power input P_{OH} alone. P_{OH} and the kinetic stored energy W_K have the following relationship: $P_{OH} = I_p V_{loop} = W_K/\tau_e$, where V_{loop} is the loop voltage. W_K is expressed by a volume integral of their product of temperature and density, $W_K = \frac{3}{2}\int(n_i T_i + n_e T_e)dV$. By taking $V_{loop} = 2\,\mathrm{V}$, $n_i = n_e$, $T_i = T_e$ and assuming parabolic profiles for them, the achievable T_e for particular I_p and n_e can be evaluated. A survey of various n_e found that I_p of 100–200 kA is necessary to realize T_e and n_e estimated as the target plasma for HHFW heating experiments in the previous section.

In this way, design plasma parameters for TST-2 were determined. The consideration described here are based on many assumptions, and inevitably have large error bars. It is nevertheless important to grasp the relationship between a variety of design parameters and to evaluate the magnitudes of these parameters.

4.3   Engineering details of TST-2

4.3.1   Major changes from TST-M

A major change of design policy is that the TST-2 vacuum vessel is continuous in the toroidal direction, whereas the TST-M vacuum vessel had a toroidal cut, which prohibits generation of net toroidal eddy currents induced in the vacuum vessel wall. The toroidal cut is advantageous for utilizing the limited amount of OH flux to drive the plasma current, and is employed in several tokamaks. However, because of the severe limitation of available area on the inboard side in ST, it is difficult to provide a toroidal cut all around the poloidal circumference. TST-M realized the toroidal cut in a tricky way. It used a cylindrical vessel and located the OH coil and center legs of the TF coil inside the vessel. These in-vessel coils were made of Mineral Insulation (MI) cables. The drawback of such a design is that the small cross sectional area of the MI cable makes the pulse length rating of the coils rather short, which hinders our plan to prolong the discharge duration.

In TST-2, a toroidally continuous vacuum vessel was used, and all coils were located outside the vessel. Since many vacuum feedthroughs used in TST-M were all removed, manufacturing of coil feeders become easier and more reliable. The pulse length rating of the TF coil was increased by a factor of 7. This design makes it possible to wind the OH solenoid around the center legs of the TF coil, which increased the flux swing of the OH solenoid by a factor of 5. On the other hand, careful minimization of the thickness of the vacuum vessel wall and development of a technique to compensate for eddy
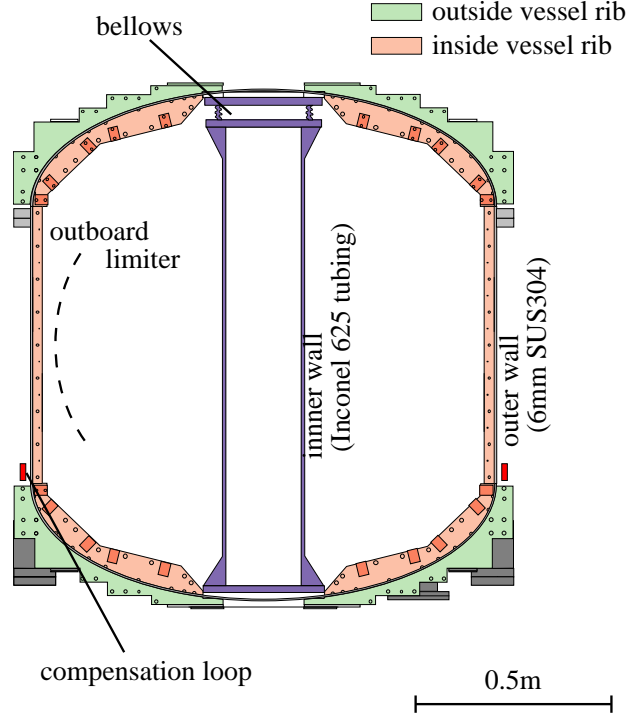
Figure 4.6: Cross section of the TST-2 vacuum vessel.

currents induced in the vacuum vessel wall became necessary.

4.3.2 Vacuum vessel

Figure 4.6 shows the TST-2 vacuum vessel. The height and the radius of the vacuum vessel are 1600 mm and 700 mm, respectively. As mentioned in the previous subsection, it is continuous in the toroidal direction. In order to reduce effects of induced eddy currents, the thickness of the vacuum vessel wall was carefully minimized. The cylinder and the top and bottom domes are made of 6 mm thick stainless steel (SUS-304), while the inner wall is made of a 1.6 mm thick Inconel-625 tubing. The top dome is sealed against the cylinder using a Viton O-ring, and can be separated for installing a large apparatus such as induction coils or RF antennas, if necessary. Based on Japan Industrial Standard (JIS) pressure vessel code, the cylinder is designed to withstand about 2.4 atm from the outside. Considering the reduction of the maximum allowable pressure by port openings as well as electromagnetic forces expected during ST operation, the vessel is reinforced by 12 ribs welded inside and outside the vessel. The inner ribs, welded on the center stack
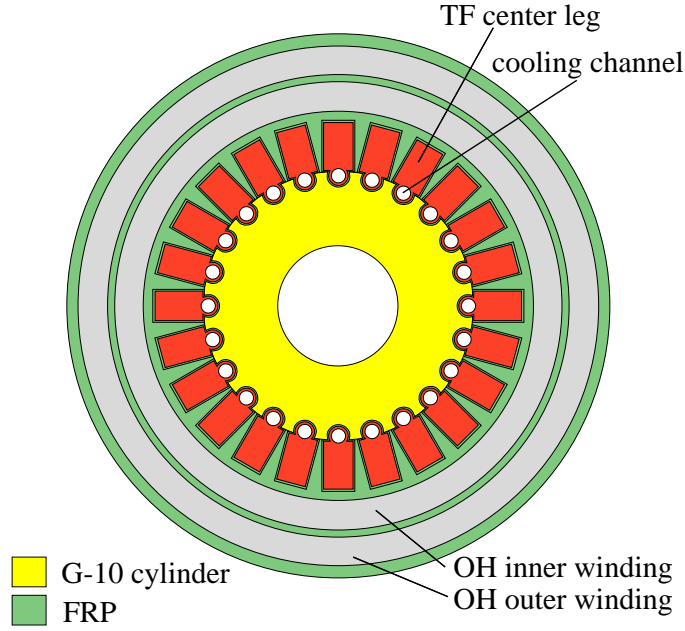
Figure 4.7: Cross section of the center stack.

tubing, are located at $R = 0.125\,\mathrm{m}$. The outboard limiter, which defines the plasma boundary on the outboard side, has a curved contour following the front surface of the RF antenna as shown in Fig. 4.6, and is located at a major radius of $R = 0.64\,\mathrm{m}$ on the midplane.

The behavior of vacuum vessel eddy current was analyzed using a filament current model. According to analysis, the eddy currents induced on the upper dome and the cylinder are expected to be so large as to affect the vertical stability of the plasma seriously, since the magnetic field produced by eddy currents is up-down asymmetric. A compensation loop made of copper conductor was added to reduce the up-down asymmetry. The time constant, determined mostly by the flanges and the compensation loop, is calculated to be $4\,\mathrm{ms}$. The time constant would be shorter by a factor of four without the flanges and the compensation loop.

4.3.3   Center stack

The center stack (CS) is a key component located on the inboard side of torus (4.2). The newly manufactured center stack of TST-2 consists of the Ohmic heating (OH) solenoid and the center legs of the TF coil that are consolidated into a monolithic structure by fiber-reinforced plastic. The height and the

outer diameter of the CS are 2240 mm and 226 mm, respectively. The cross section of the CS is shown in Fig. 4.7. The center legs of the 24-turn toroidal field (TF) coil made from oxygen free high conductivity copper are arranged around a G-10 cylinder, and a 239-turns OH solenoid is wound around the TF legs in two layers. Mica-based tape and fiberglass tape are used for insulation between conductors and is molded by epoxy resin using the vacuum assisted resin transfer method. The conductors of the CS are water-cooled for long pulse operation.

The rated insulation voltage, operating voltage, and operating current are 12 kV, 10 kV, and 25 kA for both OH solenoid and TF legs. The inductance and the resistance of the OH solenoid is 1.04 mH and 3.1 mΩ, resulting in the L/R time constant of 33.5 ms which is comparable to the discharge duration in TST-2. The flux swing corresponding to 25 kA of OH solenoid current is 127 mVs. It can be extended to 254 mVsec using the double-swing mode. The toroidal field strength at the geometrical center ($R = 0.38$ m) at this current is 0.31 T. Since the stress produced by the TF coil current has a large margin even at 25 kA, the TF would be operated at 0.4 T after upgrading the power supply and the support structure for outer legs.

4.3.4 Volt-second consumption

The main task of the OH solenoid is to drive current in the plasma by induction. The plasma current driven by this flux swing can be estimated using the method described in Ref. [113], in which the total flux Ψ_{total} is decomposed as

$$\Psi_{\text{total}} = \Psi_{\text{internal}} + \Psi_{\text{external}} + \Psi_{\text{resisitive}}, \tag{4.3}$$

where Ψ_{total} is the flux provided by the external poloidal field coils including the OH solenoid, and Ψ_{internal} and Ψ_{external} are the poloidal fluxes produced by the plasma current inside and outside the plasma, respectively. $\Psi_{\text{resisitive}}$ is the balance between Ψ_{total} and $\Psi_{\text{internal}} + \Psi_{\text{external}}$ and is called the resistive flux loss. Ejima expressed these terms in forms proportional to the plasma current,

$$\Psi_{\text{internal}} = \mu_0 R \ell_{\text{i}} I_{\text{p}}/2, \tag{4.4}$$

$$\Psi_{\text{external}} = L_{\text{ext}} I_{\text{p}}, \tag{4.5}$$

$$\Psi_{\text{resisitive}} \equiv C_{\text{E}} \mu_0 R I_{\text{p}}, \tag{4.6}$$

where ℓ_{i} is the normalized internal inductance and L_{ext} is the external inductance of the plasma, and C_{E} is the Ejima coefficient. ℓ_{i} is determined by the current density profile in the plasma and is typically in the range 0.3–1.2.
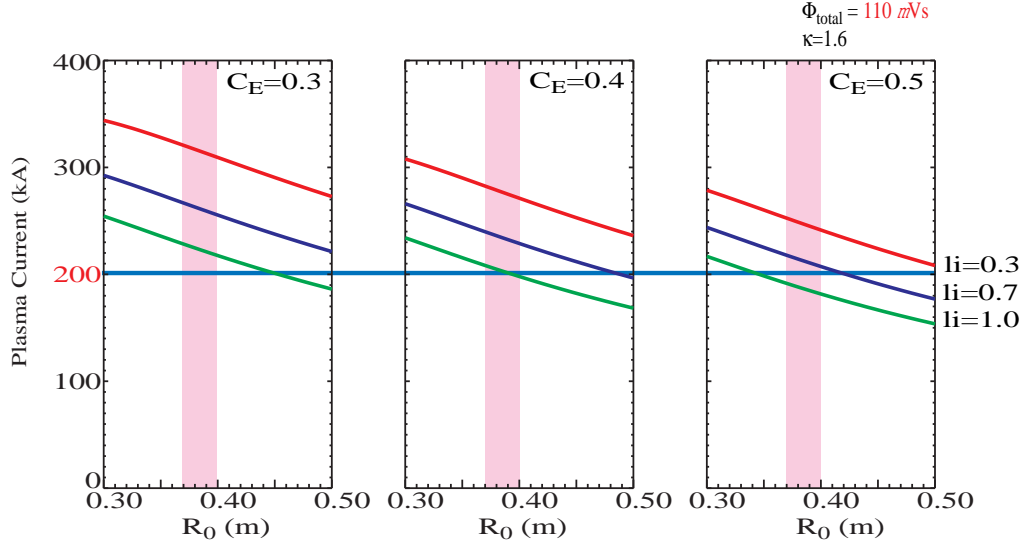
Figure 4.8: Estimates of the driven plasma current by the OH solenoid. Plasma current that can be driven by 110 mVs is calculated for the ranges of major radius of $0.3 \sim 0.5$ m, internal inductance of 0.3, 0.7, and 1.0, and Ejima coefficient of 0.3, 0.4, and 0.5.

An approximate expression for L_{ext} is [114]

$$L_{\text{ext}} = L_{\text{s}} - \mu_0 R \frac{M-1}{4} \big(\ln(8/\epsilon) + \beta_{\text{p}} + \ell_{\text{i}}/2 - 3/2\big) \qquad (4.7)$$

where L_{s} and M are dependent only on the boundary shape parameters, R, κ and A (see [114] for detailed expressions of L_{s} and M). Typically $C_{\text{E}} \geq 0.4$ for large tokamaks, and $C_{\text{E}} = 0.3$–0.5 is reported from the CDX-U spherical tokamak [115].

Predicted plasma currents driven by a flux swing of 110 mVs for ranges of ℓ_{i} and C_{E} are shown in Fig. 4.8. It is found that, except for the most pessimistic case, 110 mVs is enough to start up I_{p} from 0 to 200 kA. Analysis of flux consumption in TST-2 discharges is described in Sec. 4.5.3. It is found that I_{p} of 100 kA was achieved by approximately 60 mVs, consistent with the results of calculation presented here.

4.3.5   Toroidal field coil

The toroidal field (TF) coil consists of inner legs and outer legs. The outer legs are made of tough-pitch copper (TPC), insulated by Kapton tape, and

covered by polyvinyl chloride (PVC) heat shrink tubing. Insulation and protective covering were done in house. Inner and outer legs are connected at the top and the bottom of the CS. The resistances of inner and outer legs are $3.46\,\mathrm{m\Omega}$ and $2.88\,\mathrm{m\Omega}$, respectively. The calculated inductance of the TF coil is about $520\,\mu\mathrm{H}$. The total resistance including the feeder line is approximately $10\,\mathrm{m\Omega}$, and therefore the L/R time is about $50\,\mathrm{ms}$.

In the design of the TF coil, reduction of non-axisymmetric error fields including the TF ripple and the stray field are important. The TF stray field is a concern for disturbing the plasma break down and plasma position control. In fact, it caused problems on TST-M. In order to reduce the TF ripple, placing the outer legs far away from the plasma is effective. However, because of power supply limitation, this approach was not possible. An alternative approach to increase the number of TF turns and decrease the toroidal angle between turns was adopted, even though this is not preferable to secure good port accessibility. Comparing several cases of outer leg major radius, the outer leg position of $R = 0.9\,\mathrm{m}$ was chosen. Using 24 turns
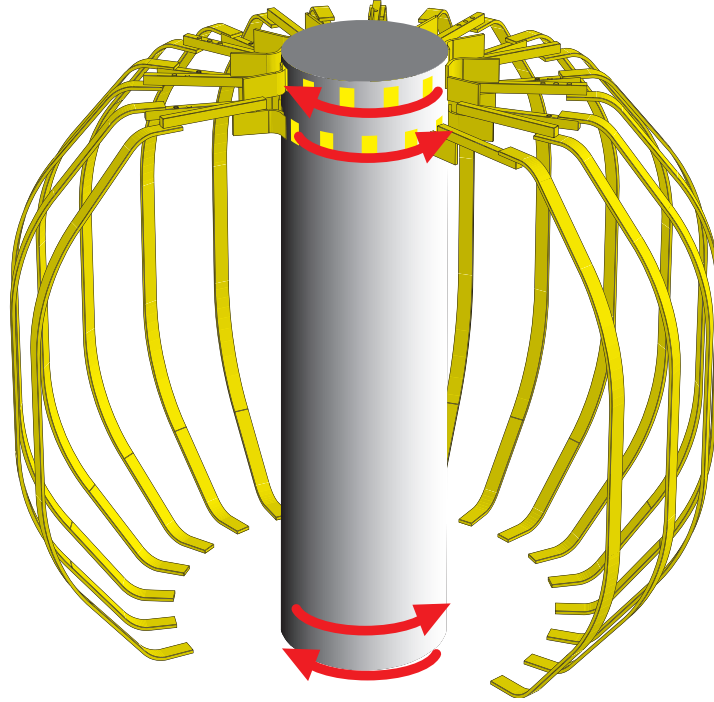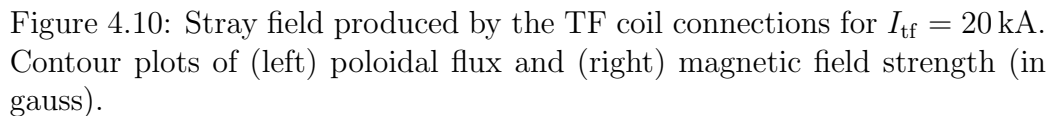

Figure 4.9: Schematic showing the connections of inner and outer legs of the TF coil. The stray field produced by these connections are shown in Fig. 4.10.

Figure 4.10: Stray field produced by the TF coil connections for $I_{\mathrm{tf}} = 20\,\mathrm{kA}$. Contour plots of (left) poloidal flux and (right) magnetic field strength (in gauss).

for the TF coil, the calculated TF ripple is $\widetilde{B_{\mathrm{t}}}/B_{\mathrm{t}} < 10^{-3}$ in the region of $0.1\,\mathrm{m} \leq R \leq 0.6\,\mathrm{m}$.

The power line connecting the TF coil and the power supply and the connections between individual TF coil turns contribute to the stray field. The connection of the TF coil and the power line is made at the top of the vessel, and the power line runs away from the vessel immediately. The TF coil has toroidal current components only at the connections between inner and outer legs. The connections are placed at the top and the bottom of the CS, and the toroidal current components are arranged as shown in Fig. 4.9. This design is intended to cancel the poloidal fields from the toroidal current components with each other. In addition, by making these toroidal current components symmetric with respect to the midplane, the horizontal field component of the residual poloidal field is further reduced. A calculated stray poloidal field is shown in Fig. 4.10. It is noted that the remaining field is of the order of 1 gauss in the vacuum vessel and has no horizontal

Table 4.2: Poloidal field coils of TST-2

	PF1	PF2	PF3	PF4[1]	PF5[1]
R [m]	186	604	950	1169.5	1169.5
Z [m]	±820	±719	±465	±650	±400
Height [mm]	65	65	109	24	24
Width [mm]	43	37	39	27	27
Conductor Crosssection [mm^2]	3×40	3×40	3×10	5×20	5×20
Number of turns	9	6	40	3	3
Taps	3, 6	1, 3	16, 24	1, 2	1, 2
Max. Current [kA]	25	25	10	10	10
Max. Voltage [kV]	5.	5.	5.	5.	5.

[1] Design details are found in [116].

component on the midplane, which is preferable for equilibrium control.

4.3.6 Poloidal field coil

The role of poloidal field (PF) coils is to control the shape of the plasma boundary. Since the tokamak plasma tends to inflate along the major radius, balancing this outward force using the repulsive force between two anti-parallel currents is the primary task of PF coils. PF coils are also used to control higher order shaping parameters such as the elongation and the triagularity.

TST-2 has five sets of poloidal field coils as listed in Table. 4.2 (see also Fig. 4.2). Three PF coils, PF1, PF2, and PF3 are newly manufactured for TST-2. PF4 and PF5 coils were used on TST-M. Balancing of the outward force is the main role of PF3. PF4 is used in series with the OH solenoid to cancel the fringing field of the OH solenoid. PF2 is used to control the vertical elongation. PF5 is used in series with PF2 to increase the ramp rate of the vertical field during the start-up phase of the discharge. PF1 is designed to produce a poloidal field with a large decay index, $n = -\frac{R}{B_z}\frac{\partial B_z}{\partial R}$. It was used to create a mirror field in RF start-up experiments. PF1 can be used as a divertor coil in future experiments.

The establishment of PF coil operational scenarios occupied a significant fraction of TST-2 design activity, and are discussed in Sec. 4.5.1

4.4   Control system and power supplies

4.4.1   Control System

The control system used for TST-M was based on that used on the TNT-A tokamak, which operated during the late 1970s. Electronic parts used in this system were vacuum tubes and standard logic ICs and the control sequence was realized by relays. Naturally, it does not reflect recent progress in digital technology. Since this system is not only inconvenient to use, but also questionable from the viewpoints of safety and reliability, the control system was updated to a more modern system.

At the chip level, standard logic IC circuits were replaced by PICmicro® microcomputers (PIC) from Microchips Technology Inc. [117]. The PIC is a single chip CPU with many on-chip peripheral circuits, used for A/D convertion, communication with PC, etc. A single-ship PIC can replace circuits consisting of 10–20 standard logic ICs, and even add the ability to communicate with a PC over RS-232-C or ethernet. Since it is a CPU, the sequence logic realized by relays can be replaced by software running on it. Over 40 PIC-based controllers were implemented for TST-2. In many cases, new controllers consist of only a few chips, PIC itself and input/output buffers.

On the PC side, communication with PIC controllers are done by Lab-VIEW (National Instruments Co.), which also provides the front-end to users. All aspects of TST-2 operation were integrated into a single LabVIEW-based application. Figure 4.11 shows a screen shot of LabVIEW, from which the operator can specify charging voltages of power supplies, timings and durations of gas puff and pre-ionization power, coil current waveforms, etc. Control parameters are saved to a file automatically, so that the setting used for a previous shot can be restored immediately.

Data acquisition for TST-2 is performed by transient recorders. Signals are stored in the memories of transient recorders, and then transfered to a UNIX workstation after each discharge. Computer Automated Measurement and Control Standard (CAMAC) based transient recorders are continued to be used for TST-2. EC-6900 (Elmec®) is a PC-based 500 kHz 96-channel simultaneous sampling transient recorder and was newly acquired for TST-2. The DAS (Data Acquition System) program on UNIX was expanded to handle EC-6900 data, so the experimentalist does not need to distinguish whether the signal is recorded by CAMAC or EC-6900. Data stored in the workstation are file-shared and accessed from PCs using Dview, a data viewing software running on Interactive Data Language (IDL).
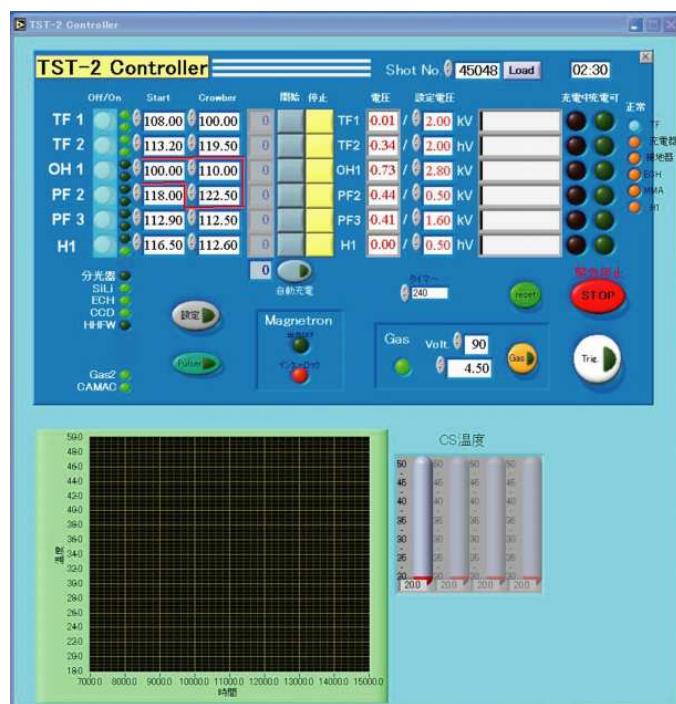
Figure 4.11: User interface screen of LabVIEW-based TST-2 control software.

4.4.2 Capacitor banks

The power supplies used to energize the TST-2 magnet system are capacitor banks, formerly used for TST-M. Power supply modifications are made continually to improve plasma performance in TST-2. Upgrading activities are still continuing at Kashiwa Campus.

Figure 4.12 shows the final state of power supply circuits and TST-2 magnets at Hongo Campus, used for the radio-reflectometer experiment (Sec. 6.1). Modifications from the TST-M power supply system are sumarized below. High energy density capacitors were procured for the TF power supply. For current control of the PF3 coil, a chopper type switching circuit based on Insulated Gate Bipolar Transistor (IGBT) modules (CM1200HA-66H) was installed at the output stage of the capacitor bank. The chopper can be operated at 5 kHz and the rated voltage and current are 2.5 kV and 3 kA, respectively. A small capacitor bank with an H-bridge type current controller was also developed for feed back control of the horizontal field coil (not shown in Fig. 4.12). For longer discharge durations, ignitrons which can switch high voltage and high current can be used in parallel, if needed.

At Kyushu University, different types of power supplies were used for heating experiments. These power supplies are described in the next subsection.

4.4.3 Modifications for TST-2@K

For the heating experiment performed at Kyushu University, power supplies of the TRIAM-1M superconducting tokamak were used. Since the magnet systems of TST-2 and TRIAM-1M are very different, it is important to determine the optimum connections between TRIAM-1M power supplies and TST-2 magnets. Table 4.3 lists the TRIAM-1M power supplies. These power supplies are switching power supplies, operated in pulse width modulation (PWM) mode. The difference from usual switching power supply is that they do not have ripple reduction filters at their outputs. Hence, the output voltages go back and forth between zero and the power supply voltages in every PWM cycle. Power supplies for SP, SN, and BH-FB are controlled by a VME based real-time (RT) controller, which has a base clock rate of 3 kHz. The RT controller controls the current fed from the power supply using a regular PID feed back algorithm. As a reference value of current, in addition to directly specifying the current, one can specify a current calculated from a couple of diagnostics. The RT controller is used for feedback control of other plasma parameters such as density. But these capabilities were not used for TST-2@K because of the relatively short discharge duration.
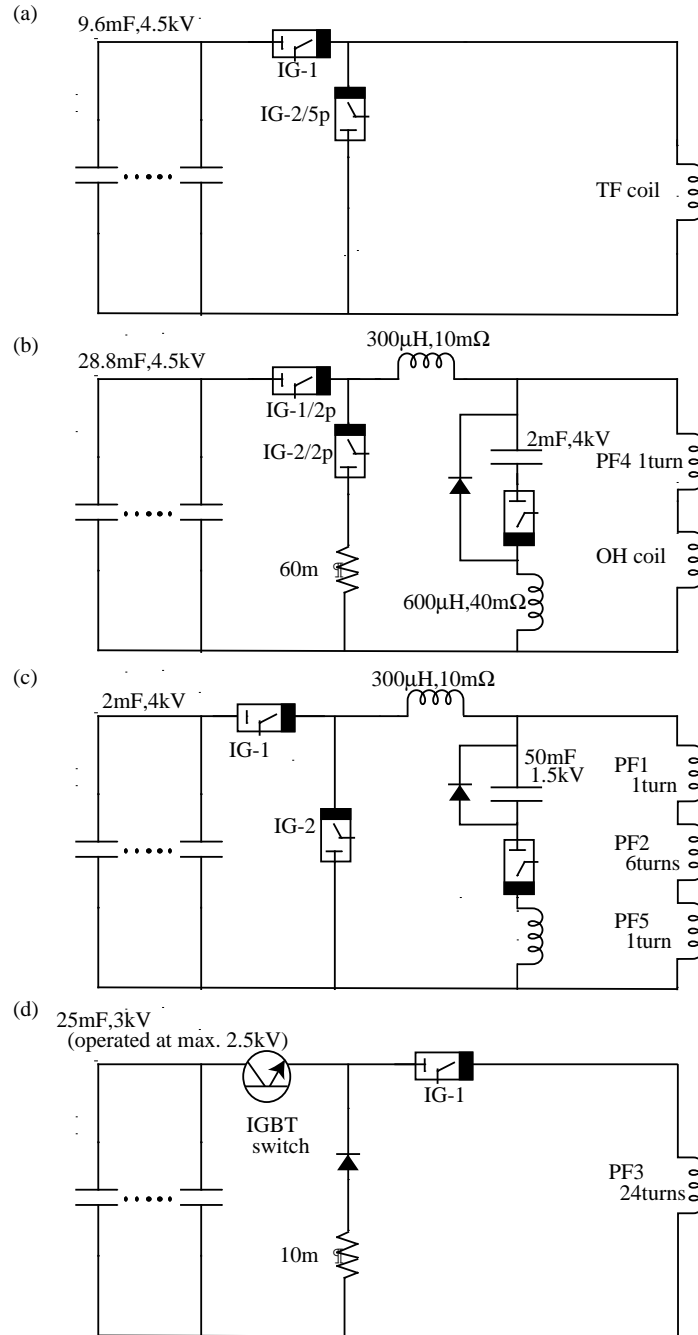
Figure 4.12: TST-2 magnet circuits for (a) TF coil, (b) OH-PF4 coil set, (c) PF1-PF2-PF5 coil set, and (d) PF3 coil used in experiments at Hongo Campus.

Table 4.3: Power supply set of the TRIAM-1M tokamak.

	CT	SP	SN	BH-FB	BH
Spec.					
Polarity	bipolar	unipolar	unipolar	bipolar	unipolar
Current [kA]	35	35	94	10	4.4
Voltage [kV]	1.3	0.296	0.38	1.5	0.052
SW Freq.[kHz]	4CB[1]	0.72	0.72	3	0.72
Role					
TRIAM-1M	OH	$B_z\ (n>0)$[2]	$B_z\ (n<0)$[2]	B_H FB	Steady B_H
TST-2@K	OH	PF2-5	TF	PF3	

[1] Current shape can be modified by firing 4 capaciter banks (CB)

[2] Set of coils for generating positive and negative decay index n to control the plasma shape.

4.5   Plasma operation

4.5.1   operational scenario

When the vacuum vessel is continuous in the toroidal direction as in TST-2, in addition to the coil currents and the plasma current, eddy currents induced on the vacuum vessel contribute to the magnetic field structure. The effect of eddy currents is most significant at break down, when the poloidal field strength must be minimized. During the breakdown phase, electrons are accelerated by the electric field produced by the OH solenoid, and collide with neutrals and ionize them. A chain reaction of ionization produces the plasma. If unwanted poloidal field is too large, as an electron moves along the magnetic field, it encounters the vessel wall before ionizing sufficient number of neutrals, resulting in a longer time to produce the plasma, or even failure to break down.

Figure 4.13 illustrates the evolution of eddy currents and PF coil currents. As shown in (a), the plasma operation is started by the ramp-up of the OH solenoid current. This is called pre-charging. The outer PF coils (PF4) are connected in series with the solenoid in order to prevent the magnetic field line produced by the solenoid from intersecting the vacuum vessel. Pre-charging of the solenoid induces eddy currents. Initially, eddy currents are induced near the solenoid. Eddy currents induced in (a) decay, while eddy currents are induced at larger radii, as shown in (b). This propagation occurs over the time constant of the vacuum vessel (4 ms), while pre-charging of the OH solenoid is completed in about 10 ms. When pre-charging is completed, eddy currents produce a large magnetic fields inside the vacuum vessel as
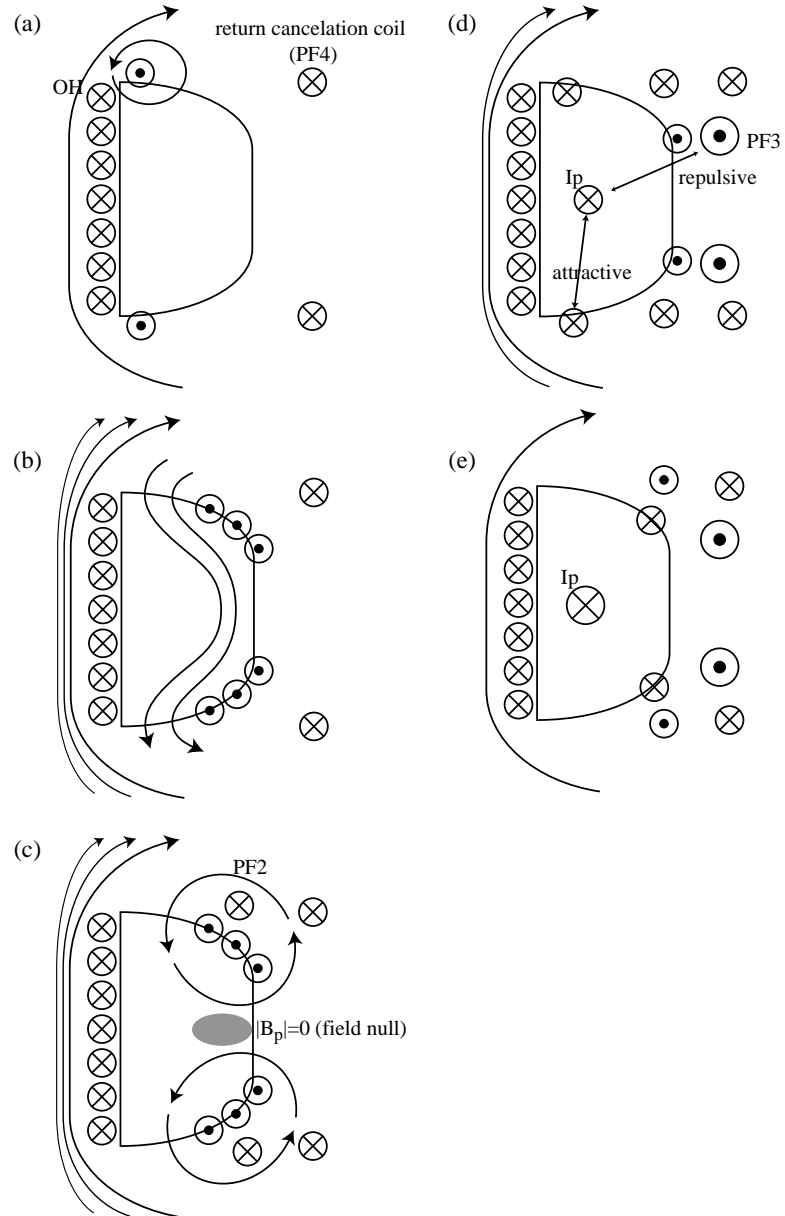
Figure 4.13: Schematic of eddy current cancellation by PF coils.

shown in (b).

After completion of pre-charge, the OH solenoid current begin decreasing, which induces a positive loop voltage. To achieve breakdown by this loop voltage, positive PF2 coil currents are necessary to cancel the eddy currents, as shown in (c). On the midplane, the magnetic field produced by the upper and lower dome currents cancel each other, and a field null (where $|B_\mathrm{p}| = 0$) is created. The situation just after break down is shown in (d). The plasma current flows in the same direction as the OH solenoid. The plasma current tends to expand outward. Holding the plasma in the center of the vacuum vessel using the repulsive force between anti-parallel currents is the role of PF3. The decreasing OH current induces eddy currents that are in the same direction as the plasma current. These currents attract the plasma from the top and the bottom of the torus, which makes the plasma unstable in the vertical direction. If the plasma becomes too unstable, the PF2 coil current must be reversed as shown in (e) to stabilize the plasma.

Two codes were developed to understand the behavior of the eddy currents and their effect on the magnetic field configuration. The first code (EDDY) calculates the evolution of eddy currents using a toroidally symmetric model of the vacuum vessel. The second code (VFIT) calculates the vacuum magnetic field configuration from experimentally obtained flux loop data. Before proceeding with the analyses based on these codes, it is instructive to consider qualitatively how eddy currents are induced on the vacuum vessel, and to estimate the PF coil currents necessary to counteract the effects of these eddy currents.

Calculation of eddy currents using EDDY

EDDY is a simulation code that calculates the evolution of eddy currents induced on the vacuum vessel. The magnetic field is calculated from the obtained distribution of eddy currents and the currents in the poloidal field coils including the OH solenoid. In this code, the vacuum vessel is modeled as a toroidally symmetric conductor that is divided into small segments as shown in Fig. 4.14. Each segment is treated as a single turn circular coil (Filament Current, FC). The evolution of the current in the k-th FC is expressed as

$$L_\mathrm{k}\frac{dI_\mathrm{k}}{dt} = -\sum_i M_\mathrm{i-k}\frac{dI_\mathrm{i}}{dt} - R_\mathrm{k}I_\mathrm{k} \qquad (4.8)$$

where L_k and R_k are the self inductance and the resistance of the k-th FC and $M_\mathrm{i-k}$ is the mutual inductance between the k-th and the i-th FC. L_k and $M_\mathrm{i-k}$ are calculated from the poloidal flux at (r, z) produced by a FC
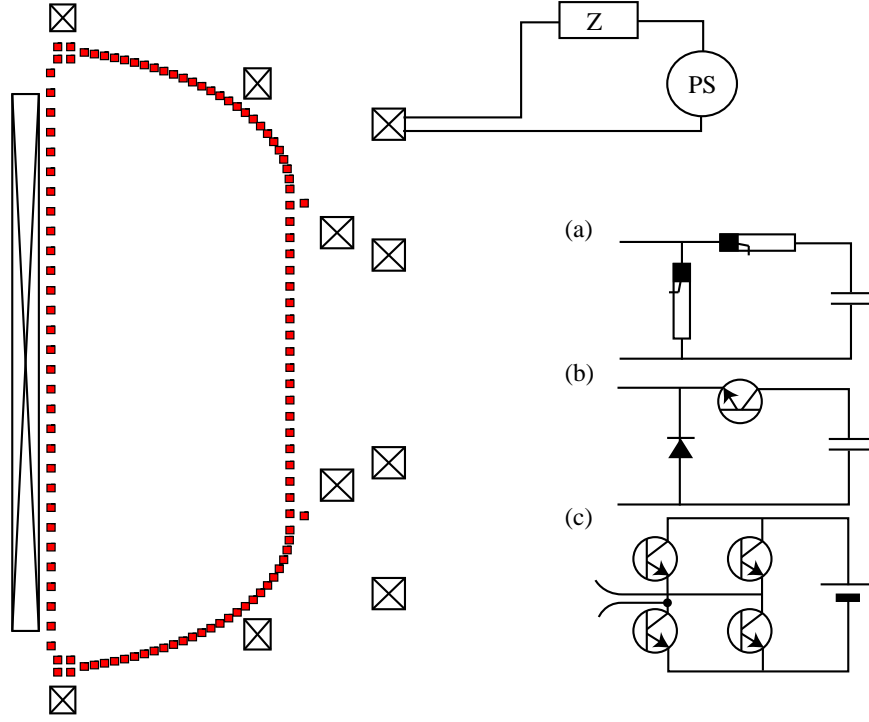
Figure 4.14: Schematics of the eddy current code. Vacuum vessel is segmented into small wall elements. PF coils are connected to power supplies of various types: (a) ignitron based capacitor bank, (b) DC chopper with capacitor, and (c) H bridge based switching power supply.

with current I at (r_0, z_0). In cylindrical coordinates, the poloildal flux is expressed as

$$\Psi(r, z) = \frac{2\mu_0 I \sqrt{r_0 r}}{k} \left((1 - \frac{k^2}{2}) K(k) - E(k) \right) \qquad (4.9)$$

$$k^2 = \frac{4 r_0 r}{(r_0 + r)^2 + (z_0 - z)^2} \qquad (4.10)$$

where $K(k)$ and $E(k)$ are complete elliptic integrals of the first kind and the second kind, respectively.

For poloidal field coils, the voltage applied by the power supply must be added,

$$L_k \frac{dI_k}{dt} = -\sum_i M_{i-k} \frac{dI_i}{dt} - R_k I_k + V_{PS}. \qquad (4.11)$$

The expression for V_{PS} depends on the power supply model. Besides the general purpose voltage source and current source, several types power supply
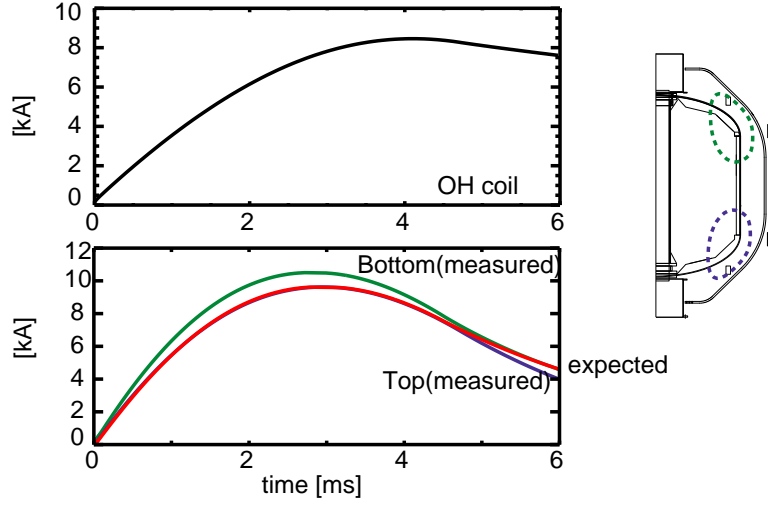
Figure 4.15: Measured eddy currents at upper and lower domes, including the large flange. Only the OH solenoid was operated.

used in TST-2 are implemented in EDDY, (1) single swing capacitor bank power supply, (2) capacitor bank with a DC chopper, (3) capacitor bank with an H bridge, and (4) double swing capacitor bank power supply. Schematic diagrams for (1) to (3) are shown in Fig. 4.14. (4) is the model circuit (b) shown in Fig. 4.12.

The evolution of the eddy currents and coil currents are given by a matrix equation derived by combining Eqs. 4.8 and Eq. 4.11,

$$\mathbf{M}d\vec{I}/dt = -\mathbf{R}\vec{I} + \vec{V}, \tag{4.12}$$

where matrix $\mathbf{M}$ consists of L_k and M_{i-k}, $\mathbf{R}$ is the diagonal matrix consisting of R_k, and $\vec{V}$ is the vector consisting of zero and V_{PS}. The EDDY code solves this simultaneous differential equation for given V_{PS} and $I(t=0)=0$ for all FC. For the four types of power supplies listed above, V_{PS} is calculated by integrating the current on the coil. Hence, the necessary condition for V_{PS} is the initial voltage, the capacitances, and turn-on and turn-off timings of switches.

Figure 4.15 shows a comparison of measured and calculated eddy currents induced by the OH solenoid. In this test, the vacuum vessel was opened to enable direct measurements of eddy currents by Rogowski coils. The Rogowski coils measured the eddy currents in the regions depicted on the right. The code successfully reproduces the behavior of eddy currents to within $\sim 10\%$ error. The eddy currents ramp up quickly when the loop voltage
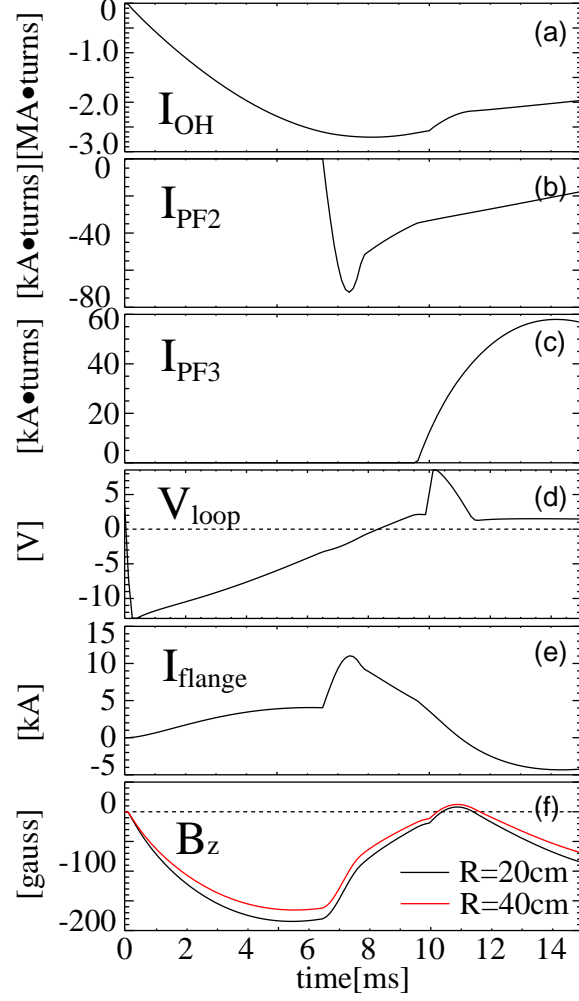
Figure 4.16: Break down scenario simulated by EDDY. (a-c) Curretns in the OH solenoid, PF2 coil, and PF3 coil, (d) loop voltage at the inboard limiter on the mid-plane, (e) eddy current induced on the flange, and (f) vertical magnetic field on the mid-plane at $R = 0.2\,\mathrm{m}$ and $0.4\,\mathrm{m}$. Note that $B_\mathrm{r} = 0$ on the midplane.
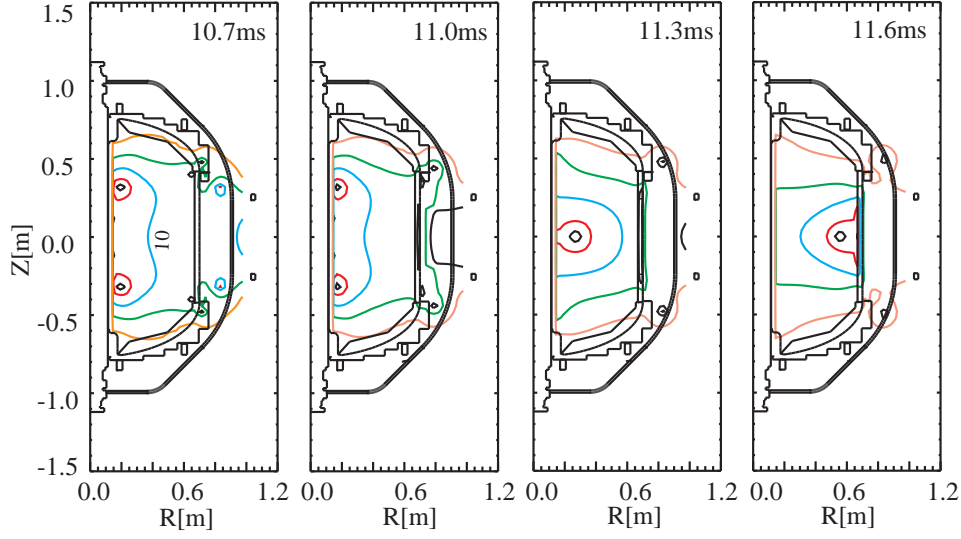
Figure 4.17: Contour plots of $|\mathbf{B}_\mathrm{p}|$ during the break down phase of the case shown in Fig. 4.16.

induced by the OH solenoid is high, and begin to decay as the OH solenoid current saturates. It is shown that the induced eddy currents have similar magnitudes to the solenoid current, indicating their significant contributions to the magnetic field configuration. It is also noted that there is a small up-down asymmetry in the measured currents. Figure 4.16 shows an example of operational scenario developed using EDDY. The OH solenoid is pre-charged by $t = 6$ ms. Large eddy currents are induced on the flanges that connect the upper dome to the cylindrical part of the vacuum vessel. By ramping up of the PF2 coil current, the magnetic fields produced by the eddy currents are cancelled, and at $t = 10$ ms when a large loop voltage is applied, the magnetic fields inside the vacuum vessel become very small. After 12 ms, the PF3 coil current is ramped up to supply the vertical field required for plasma equilibrium. Figure 4.17 shows contour plots of the poloidal field strength $|\mathbf{B}_\mathrm{p}|$ during the breakdown phase (10–12 ms), indicating that a field null ($|\mathbf{B}_\mathrm{p}| = 0$) is created.

Vacuum field reconstruction (VFIT)

A complementary technique to assist the development of PF program for break down is direct measurement of vacuum flux surface. When plasma
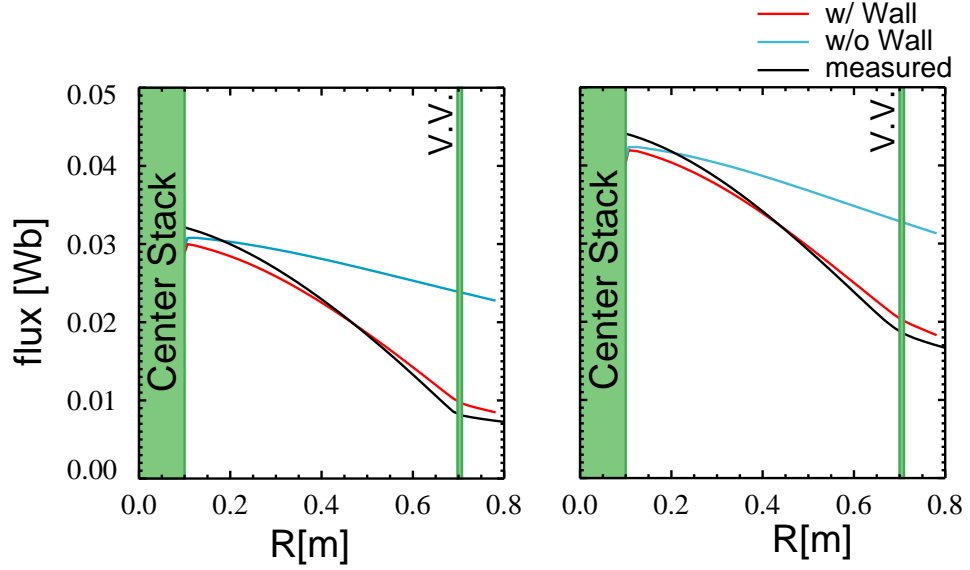
Figure 4.18: Comparison of measured (VFIT) and calculated (EDDY) vacuum poloidal flux profile for the case shown in Fig. 4.15 at $t = 2\,\text{ms}$ (left) and $4\,\text{ms}$(right). The line denoted w/o wall is the poloidal flux neglecting the contribution from eddy currents.

does not exist, the poloidal flux inside the vacuum vessel is expressed by,

$$r\frac{\partial}{\partial r}\frac{1}{r}\frac{\partial \Psi}{\partial r} + \frac{\partial^2 \Psi}{\partial^2 z} = 0. \tag{4.13}$$

According to the theory of partial differential equation, the solution of a homogeneous differential equation of second order is determined uniquely by giving either Neumann or Dirichlet condition on the boundary. In this case, the boundary corresponds to the line drawn just inside the poloidal cross section of the vacuum vessel. Ψ inside the vacuum vessel is given by

$$\Psi(r, z) = \oint \Psi(l)G(r, z, l)dl, \tag{4.14}$$

where the integration is taken along the boundary, and l is the length along the boundary. $\Psi(l)$ is the flux at the boundary and $G(r, z, l)$ is the Green function, which is the solution corresponding to the boundary condition $\Psi(l) = \delta(l - l_0)$.

Flux loops and saddle loops are installed inside the vacuum vessel as shown in Fig. 5.2. Direchlet condition on the boundary is given by interpolating fluxes measured by these sensors. Discretizing the above equation,
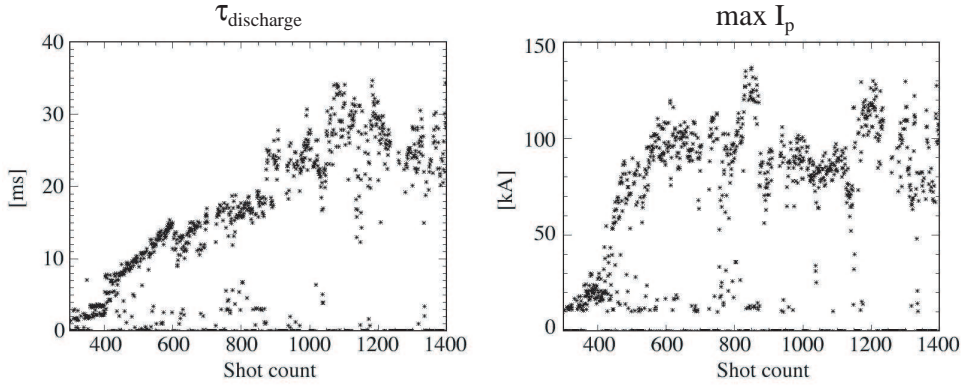
Figure 4.19: Improvement of plasma condition by repetition of discharges: (left) discharge duration and (right) plasma current as functions of shot number.

VFIT calculates $\Psi(r, z)$ as

$$\Psi(r, z) = \sum_i \Psi_i G(r, z, i) dl, \qquad (4.15)$$

where Ψ_i is the flux at the i-th flux loop and $G(r, z, i)$ corresponds to $\Psi(r, z)$ for the boundary condition

$$\Psi_k = \begin{cases} \frac{l - l_{i-1}}{l_i - l_{i-1}} & l \text{ is between i-1th and ith flux loops,} \\ \frac{l_{i+1} - l}{l_{i+1} - l_i} & l \text{ is between ith and i+1th flux loops,} \\ 0 & \text{elsewhere.} \end{cases} \qquad (4.16)$$

Since $G(r, z, i)$ can be calculated beforehand, only matrix multiplication and summation are needed to obtain $\Psi(r, z)$.

Figure 4.18 shows a comparison of the vacuum poloidal flux on the midplane obtained by EDDY and VFIT. It is shown that EDDY and VFIT results resemble each other. Neglecting the contribution of eddy currents gives completely different results.

4.5.2   Discharge cleaning

Generally, there are particles weakly bound to the vacuum vessel wall, just after the vacuum vessel is closed. In fusion experiments, when particles from the plasma hit such a contaminated wall, bound particles can leave the wall, enter the plasma, and radiate a significant energy in the form of

light, hindering the plasma to become hot. Such particles must be removed before starting plasma experiments. In TST-2, baking of the vacuum vessel at 100 ℃, discharge cleaning, and titanium gettering were performed. It is shown from improvements in both discharge duration and plasma current (shown in Fig. 4.19), that the wall condition has become stationary after approximately 1000 plasma discharges.

4.5.3 Startup efficiency

In the last two subsections of this chapter, the experimentally obtained Ejima coefficient C_E and energy confinement time τ_E are compared with those estimated during the design phase. To calculate C_E, the poloidal flux at the center of the plasma must be evaluated. This can be done by either MFIT_FCF (Sec. 5.1.2) or TOKAMAC (Sec. 5.1.3). Since MFIT_FCF can be run even in the absence of plasma, it is used in the present analysis.

Figure 4.20 shows the evolution of the decomposed fluxes for discharge #303432. $\Psi_{\text{coil}} + \Psi_{\text{eddy}}$ in the figure corresponds to Ψ_{total} in Ejima's notation, and Ψ_{p} corresponds to $\Psi_{\text{internal}} + \Psi_{\text{external}}$. Note that Ψ_{eddy} makes a negative contribution, reducing the flux supplied from the coils to the plasma. The noise observed during the hatched period is caused by mis-decomposition of Ψ_{eddy} and Ψ_{p}. It is, to some extent, ambiguous when the ramp-up phase starts and ends. The beginning and the end are defined as the moment when I_{p} exceeds $10\,\text{kA}$ and when the ramp-up rate of the plasma current changes, namely $14.5\,\text{ms}$ and $23.5\,\text{ms}$ for the case shown in Fig. 4.20. From the change of fluxes shown in the figure,

$$\Psi_{\text{total}} \simeq 57\,\text{mVs}, \tag{4.17}$$

$$\Psi_{\text{internal}} + \Psi_{\text{external}} \simeq 33\,\text{mVs}, \tag{4.18}$$

so the resistive component is

$$\Psi_{\text{resistive}} \equiv C_E \mu_0 R I_{\text{p}} \simeq 24\,\text{mVs}. \tag{4.19}$$

Using $R = 0.38$ m and $I_{\text{p}} = 95$ kA in the last equation, $C_E = 0.53$ is obtained. This is slightly higher than C_E assumed in designing the OH solenoid. This is caused by the abrupt drop of plasma current occurring at $16 - 17\,\text{ms}$. The flux loss accompanying the drop is 5–$7\,\text{mWb}$. Without the loss, C_E would be 0.37–0.42.

4.5.4 Confinement

In Sec. 4.2.2, the energy confinement time (τ_E) was estimated for TST-2 plasmas using an empirical scaling law to be in the range of 1–$4\,\text{ms}$. Plasma
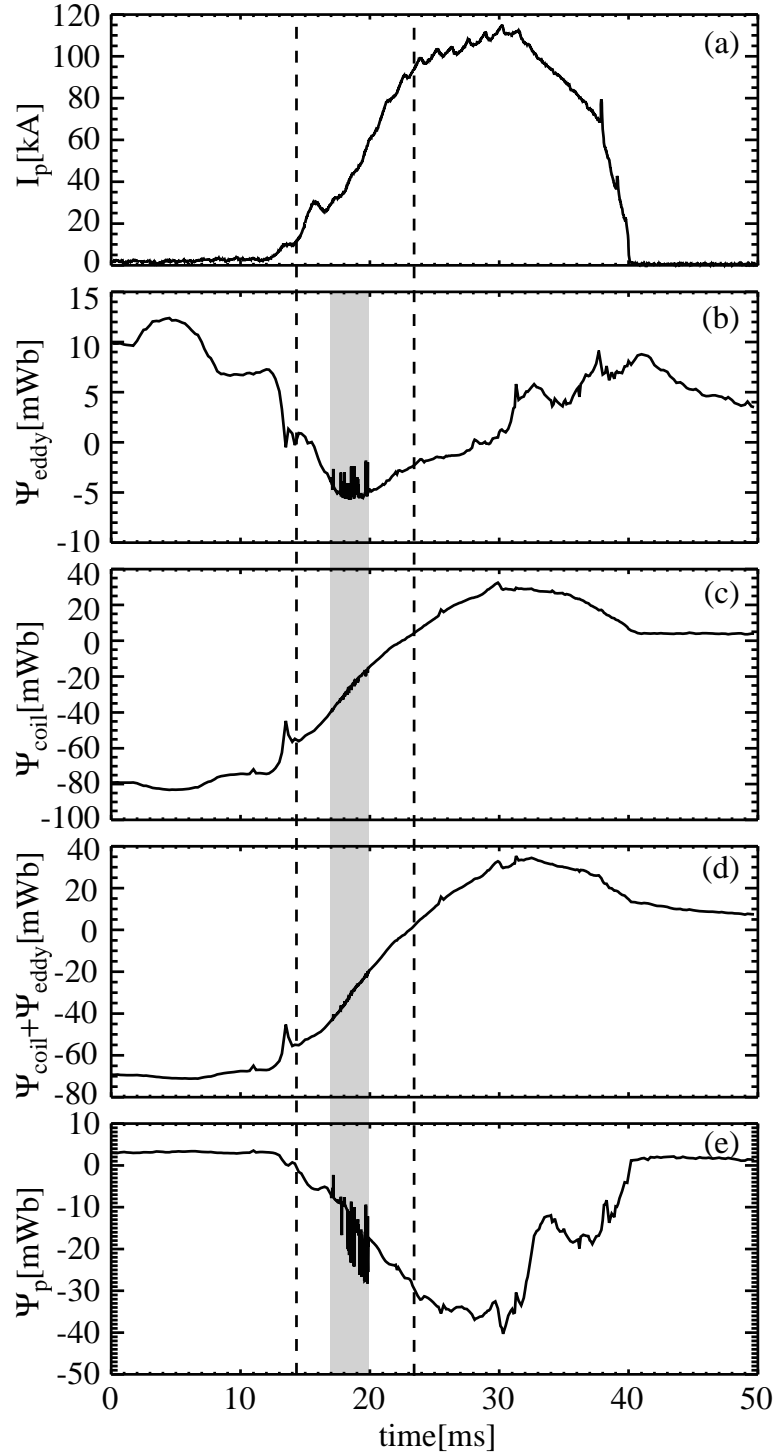
Figure 4.20: Time evolutions of (a) the plasma current and (b-e) fluxes decomposed by MFIT_FCF for #303432: (b) the flux consumed by eddy currents (Ψ_{eddy}), (c) the flux provided by the coils (Ψ_{coil}), (d) the flux provided to the plasma ($\Psi_{\mathrm{coil}} + \Psi_{\mathrm{eddy}}$), and (e) the flux built up in the plasma (Ψ_{p}).

confinement in TST-2 was assessed by comparing τ_E of the plasmas produced in TST-2 to the prediction based on scaling laws. Experimentally, τ_E can be determined from the plasma stored energy obtained by equilibrium reconstruction. Care must be exercised for the evaluation of τ_E when the plasma is not stationary.

The evolution of the total stored energy W_{total} is expressed by

$$\frac{dW_{total}}{dt} = \frac{W_K}{dt} + \frac{W_M}{dt} = P_{input} - P_{loss}, \qquad (4.20)$$

where W_K is the plasma kinetic energy, W_M is the poloidal magnetic field energy, P_{input} is the power input to the plasma (across the last closed flux surface), and P_{loss} is the power leaving the plasma. W_K and W_M are defined as the plasma kinetic energy and the poloidal magnetic field energy integrated over the plasma volume, respectively. For Ohmically heated plasmas, P_{input} is given by $-I_p d\Psi_{edge}/dt$, where Ψ_{edge} is the poloidal flux measured at the last closed flux surface. The energy confinement time τ_E is defined by the relationship $P_{loss} = -W_K/\tau_E$. When the plasma is stationary ($d/dt = 0$), the energy confinement time is simply given by $\tau_E = W_K/P_{input}$. However, when the plasma is not stationary, time derivative terms must be included in the denominator, and τ_E should be evaluated as

$$\tau_E = \frac{W_K}{P_{input} - dW_K/dt - dW_M/dt}. \qquad (4.21)$$

An example is shown in Fig. 4.21. Three terms in the denominator are shown in (c)–(e), and the energy confinement time is show in (f). According to this analysis, $\tau_E = 1$–2 ms in this discharge. At 30 ms, dW_K/dt is zero, $I_p = 0.102\,\mathrm{MA}$, $B_T = 0.28\,\mathrm{T}$, $n_e = 6 \times 10^{19}\,\mathrm{m^{-3}}$, $R = 0.365\,\mathrm{m}$, $\epsilon = 1.52$, $\kappa = 1.44$, and $\kappa_a = 1.37$. Using these values in Eq. 4.1 and Eq. 4.2 yields $\tau_E^{ITERL97P} = 1.0\,\mathrm{ms}$ and $\tau_E^{IPB98(y,2)} = 1.5\,\mathrm{ms}$, indicating that the energy confinement time obtained in TST-2 are consistent with predictions based on these scaling laws.

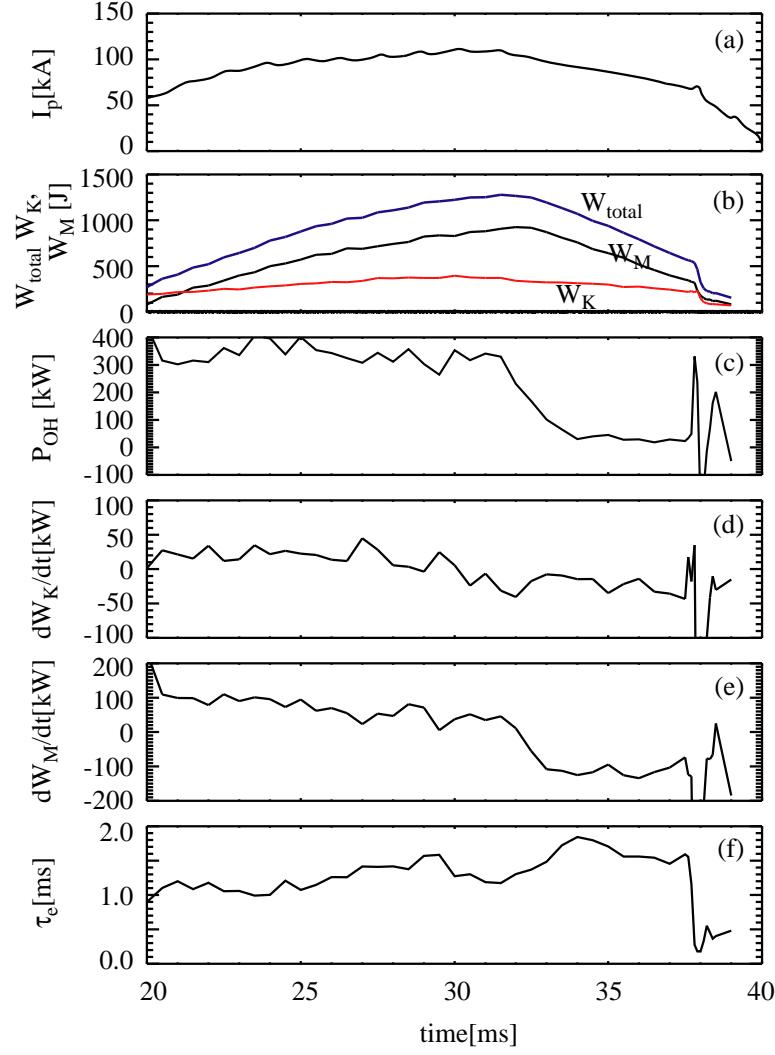Figure 4.21: Time evolutions of (a) plasma current, (b) $W_{\text{total}} = W_{\text{K}} + W_{\text{M}}$, W_{K}, and W_{M}, (c) OH input power, (d) time derivative of W_{K}, (e) time derivative of W_{M}, and (f) energy confinement time in #303432.

Chapter 5

Diagnostics and heating system

This chapter describes diagnostics used in the experiments. Most of the diagnostics installed are commonly used in the fusion plasma research. Only a short summary of theoretical background is presented, since details are found in textbooks such as Ref. [118]. Description concentrates to matters specific to TST-2.

5.1 Magnetics

5.1.1 Magnetic sensors

Magnetic diagnostics measure local magnetic field (pickup coils), magnetic flux (flux loops or saddle loops), and current (rogowski coil). These sensors are shown schematically in Fig.5.1 Output voltages of these diagnostics are given by the following equations:

$$V_{\text{pickup}} = NA\frac{\partial \boldsymbol{B}}{\partial t}, \tag{5.1}$$

$$V_{\text{flux}} = \frac{\partial \Phi}{\partial t}, \tag{5.2}$$

$$V_{\text{rogowski}} = nA\mu\frac{\partial I}{\partial t}, \tag{5.3}$$

where N is the number of turns, A is the crosssectional area, Φ is the magnetics flux crossing flux loop, n is the number of turns per unit length and μ is magnetic permearbility [118]. One needs to integrate the voltage output of the sensors, since the quantity of interest is not time derivative. In order to reduce digitization frequency, the integration is usually performed by an integrator circuit before recorded by a digitizer.
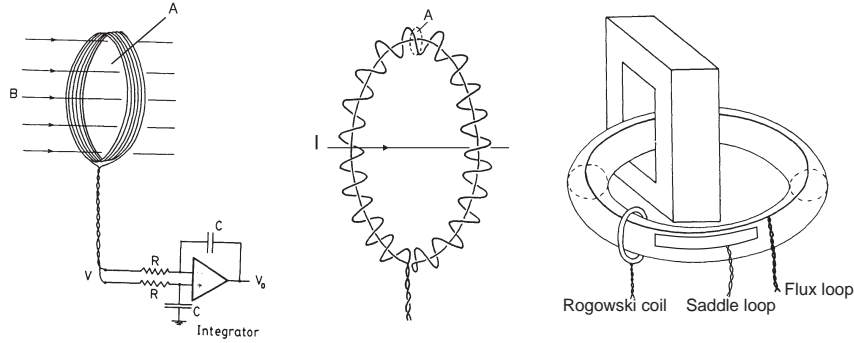
Figure 5.1: Schematics of magnetic sensors. (a) pickup coil, (b) rogowski coil and (c) flux/saddle loops (Courtesy [118])

On TST-2, 35 flux loops, 6 saddle loops, 43 pickup coils are installed. They are arranged to surround plasma as shown in Fig. 5.2. Seven of the pickup coils are arranged in the toroidal direction and used for determination of toroidal mode number of high frequency MHD events. One diamagnetic loop and one I_p rogowski coil are also installed. All these diagnostics are installed inside the vacuum vessel of TST-2, in order to increase their sensitivity to the field generated by plasma. Since the vacuum vessel is pumped in very high vacuum range ($\sim 1 \times 10^{-5}$ Pa) by a turbo molecular pump, either PTFE (Polytetrafluoroethyleneor) or FEP (Fluorinated Ethylene-Propylene) are used for the cover of cable and the bobbins of the pickup coils. The dimensions and the sensitivity are listed in the table 5.1. These diagnostics are covered by a protection plate made from stainless steel. The signals from these magnetic sensors are brought out the vacuum vessel through five 48 pin multi-pin vacuum feedthroughs, installed on the #2 ports. The pickup coils for observation of MHD events are digitized by high frequency (1MHz) digitizers without integration. The left are, then, fed to integrators, to isolators, and lastly digitized by ELEMC EC-6900 80 channel simultaneous digitizer (12bit 500kHz sampling rate).The integrator is an operational amplifier integrator circuit with a non-inverting amplifier at the output stage. The isolator is used to prevent the direct ground connection between the vacuum vessel and the digitizer in the occurrence of a fault connection between the magnetic sensor and the vacuum vessel.

Though the discharge duration of plasma is only about 20 - 30 ms, whole discharge sequence, containing a charging and discharging of the toroidal field coil and Ohmic heating solenoid, has a duration of several hundred mili second. The time constant of the integrator must be as long as 1 s. On the
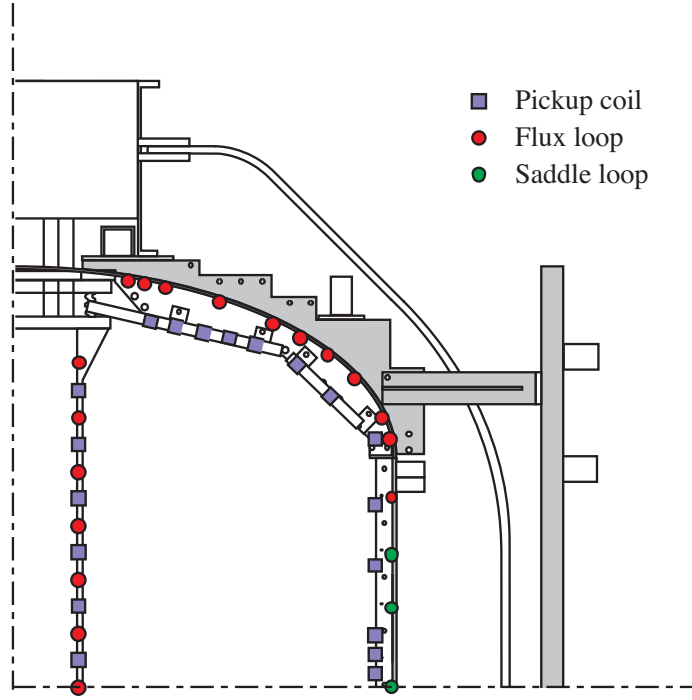
Figure 5.2: The locations of flux loops, saddle loops and magnetic pickup coils

Table 5.1: The dimensions of magnetic signals

location	cross section [mm]	length [mm]	turns	NA
inboard	5.5×12	10	100	1×10^{-2}
dome[1]	Circular R=9	20	100	2×10^{-2}
dome[2]	Circular R=18	20	100	3.5×10^{-2}
outboard	Circular R=9	20	100	2×10^{-2}

[1] for 5 sensors near the center stack
[2] for 2 sensors near the outer wall

Figure 5.3: A photo of magnetics on the low magnetic field side of the torus (without protection cover). The blue sensors are pickup coils and the yellow ones are I_p rogowski coil. Flux loops covered by the protection stainless steel tubes can also be seen.

other hand, when a MHD event occurs, plasma configuration changes as fast as $\sim 10^{-1}$ ms. For accurate integration, a good linearity from 1 Hz to at least 10 kHz with low voltage drift is required. Low off-set is also required to reduce DC offset, when the output stage amplifier is operated in a high gain mode. Several operational amplifiers were tested and OPA627 was found to have saffice the demand. As for the isolators, a low-cost commercially available printed circuit board based on ISO122 and P-61 isolation amplifier (NF corp.) are used. The ISO122 circuit board has the small signal bandwidth of 50 kHz, and it accuracy is acceptable up-to 10kHz. It is used to isolate the signals for equilibrium reconstruction, while P-61 has the bandwidth of 100kHz and be used for MHD observation.

5.1.2 Filamentary current model (MFIT_FCF)

Role of magnetic diagnostics are not limited to the measurement of local quantities expressed in Eq. 5.1, 5.2, and 5.3. Rather, the purpose of preparing many pickup coils and flux loops as illustrated in Fig.5.2 is the determination of the shape of plasmas and global quantities such as stored energy, and internal inductance described in the following two section.

Filamentary current method [119, 120, 121] estimates the boundary shape of plasma by approximating the magnetic field produced by plasma by that produced by a small number, say 6, of toroidal filamentary currents. To identify the plasma boundary, filaments need to be put approximately inside the half of the minor radius. By fitting a current on the filaments by the magnetic fields, magnetic field sufficiently far away from the filaments shows good agreement with an exactly calculated plasma boundary. The boundary shape, thus obtained, can be used to determine global parameters such as β_{p}, ℓ_{i} [120]. Since the field produced by the toroidal filamentary current can be expressed in a analytic formula, this technique provides a very quick way of estimation. The blurred filament model [122] and movable filament model [123] are variable of this technique.

In the filament code used here, 15 of blurred filaments are spread in the vacuum vessel. It is because plasmas move in the vertical direction at the beginning and the end of discharges. The code is named MFIT_FCF (magnetics fitting using fixed current filament). Instead of usual least-squre fitting, a non-neagtive least square fitting is used to prohibit the appearance of negative currents on the filaments. The boundary shape obtained by this code is not used for the determination of global parameters, since not all filaments are located well inside plasmas. Yet, this code is useful for the analysis of plasmas the beginning and the end of discharges, in which equilibrium reconstruction generally fails to converge. It is also used in the
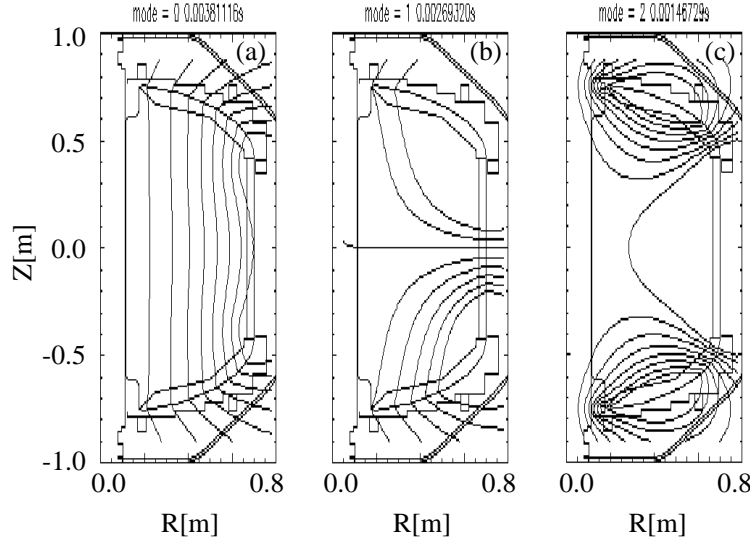
Figure 5.4: Examples of mode coils. Contour plots of the poloidal flux produced by (a) m=0, (b) m=1, and (c) m=3 eddy currents, where m is the poloidal mode number.

analysis of RF assisted plasma current ramp-up experiments [124]. Another important purpose of using the filamentary current model analysis is the estimation of the profile of the vessel eddy currents. The eddy currents are modeled by the filaments distributed on the vessel. A weighted sum of the magnetic field produced by the vessel filaments is treated as a virtual "mode coil" and currents of the mode coils are fitted. To determine the weight of filaments, eigen-vectors of L/R matrix of the filaments representing the vacuum vessel are used in this analysis. Poloidal flux profiles produced by a few low mode number mode coils are shown in Fig. 5.4. In TST-2, 6 to 8 mode coils are used, and total number of unknows become 23 to 25.

An example of the boundary shape obtained is shown in Fig. 5.5. Owing to the non-neagtive least square fitting, the obtained flux surface shown in (a) resembles Fig. 5.7. The flux surface of the magnetic field produced by the mode coils alone, shown in (b), indicates that large eddy currents are induced on the flange connecting the upper-dome and the cylinder of the vessel.
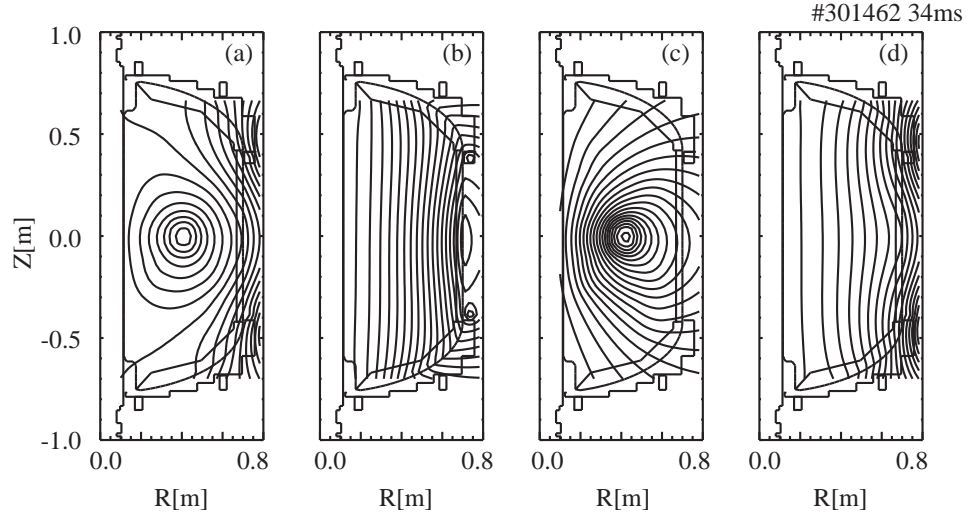
Figure 5.5: Contour plots of the poloidal flux produced by (a) all, (b) the vessel eddy currents, (c) the filaments representing the plasma, and (d) the poloidal field coils of #301462 at 35 [ms].

5.1.3 Equilibrium reconstruction

Determination of global quantities needs equilibrium reconstruction. Equilibrium of a tokamak plasma is expressed by the so-call Grad-Shafranov (GS) equation [125, 126],

$$R\frac{\partial}{\partial R}\frac{1}{R}\frac{\partial \psi}{\partial R} + \frac{\partial^2 \psi}{\partial^2 Z} = -\mu_0 R^2 p'(\psi) - \mu_0^2 (f(\psi)^2)', \qquad (5.4)$$

where ψ is the poloidal magnetic flux, $p(\psi)$ and $f(\psi)$ are the pressure and poloidal current density, and $'$ denotes the differentiation by ψ. Strictly speaking, Eq. 5.4 represents the equilibrium with an isotropic pressure and no flow. Plasmas analyzed in this research is considered to fulfill this condition. When these effects are not negligible, reconstruction becomes more difficult. Plasma with a strong flow is actively studied theoretically and ST is considered as a candidate for realizing such plasmas. Unisotropic pressure is observed on plasmas with much bean driven ion components (for example see Ref. [127]).

There have been many computer codes developed for MHD equilibrium calculation for theoretical [128, 129] and experimental [130] purposes. A detailed review of MHD equilibrium calculation is found in Ref. [131]. The code that we use is TOKAMAC, originally developed at Columbia University.

TOKAMAC reconstructs an equilibrium consistent with diagnostics in the sense of least square error, on a finite difference space mesh.

In a reconstruction code, for the sake of efficiency, functional forms of $p(\psi)$ and $f(\psi)$, which are arbitrary functions of ψ in the GS equation, are generally assumed a priori. Two types of functional form can be used in TOKAMAC. The first simpler one is

$$p'(\psi) = p_0(1 - X)^{(\gamma-1)}, \tag{5.5}$$

where X is the normalized flux given by $X = (\psi - \psi_0)/(\psi_{lim} - \psi_0)$ that gives $X = 0$ and $X = 1$ at the magnetic axis and the plasma edge, respectively. A similar expression is used for f^2. The second is a polynominal model as follows

$$p'(\psi) = p_{edge} + \sum_{i=1}^{N_p} p_i(X^{(i-1)} - X^{N_p}). \tag{5.6}$$

The parameters appears in $p(\psi)$ and $f(\psi)$ are fitted to be consistent with a specific condition, in this research, the result of the magnetic diagnostics located outside plasmas. Fitting algorithm is illustrated in Fig. 5.6, which is sometimes referred as Picard iteration [128]. In short, the GS equation is solved using a certain set of parameters at first. Secondly, linearized responses of the magnetic sensors to slight changes of the parameters are computed. Then, proper modifications to the parameters are determined by singular value decomposition in order to reduce the differences between measured magnetic sensor signals and the ones calculated from the equilibrium obtained at the first step. By the repetition of GS calculation and SVD fitting, TOKAMAC reaches a equilibrium consistent with, in this research, the magnetic diagnostics.

To introduce TOKAMAC to TST-2, a few modifications were made. In the original TOKAMAC, the number of magnetic axis (hill of the ψ surface) and separatrix (saddle point of the ψ surface) are assumed to be one. In TST-2, because of eddy currents induced on the vacuum vessel, there are many hills and saddle points on the ψ surface and TOKAMAC fails to find the magnetic axis in such situation. We restricted the region in which TOKAMAC search for the magnetic axis. We also put "mode coils" representing the eddy currents in a TOKAMAC input file to model the magnetic field produced by them. Initial current of "mode coils" are determined MFIT_FCF . A glue code to call TOKAMAC from IDL (Interactive Data Language) front end was also added. The front end accumulates the processed discharge equilibrium data in a database.

If free parameters in $p(\psi)$ and $f(\psi)$ are too many, as general in SVD fitting, parameters tends to go to extreme values those effects mostly cancel
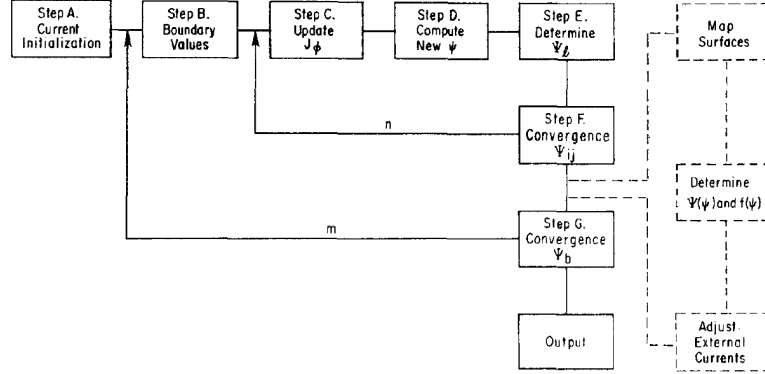
Figure 5.6: Diagram of equilibrium reconstruction [128].

each other, leading to funny results. It is known that β_p and ℓ_i can be separately measured by external magnetic field alone, for elongated plasmas like TST-2. Because the vertical field required for equilibrium depends on $\beta_p + \ell_i/2$, another restriction is provided by using the currents on the poloidal field coils in the input of TOKAMAC. It is noted in Ref. [130] that todoidal current density may be parametrized in terms of four parameters, namely β_p, ℓ_i, I_p, and q_0, indicating four free parameters can be used. However, this choice resulted in the appearance of negative pressure in the pressure profile, especially in the analysis of the early stage of discharge. Hence we choose to use the second functional form with three, one for $p(\psi)$ and two for $f(\psi)$, parameters. In the following section, we test the accuracy of fitting by increasing the number of parameters.

5.1.4 Accuracy of reconstruction

Figure 5.7 shows an example of reconstruction Evaluated β_p, β_t, β_N, ℓ_i, E_k, and E_m at this moment are 0.19, 0.016, 0.97, 0.67, 424J, and 959J, respectively. Since the quantitative analysis of the EBW heating experiments relies on increases of E_k to a large degree, it is of special importance for us to evaluate the accuracy of thus obtained global parameters. Comparison of measured and fitted values are shown in Fig. 5.8, indicating rather good agreement between measured and fitted value. Typical disagreements are within a few bits of digitizer; $1 - 2$ bits for flux loops, $2 - 4$ bits for pickup coils, and $5 - 10$ bits for saddle loops.

There are several possible sources of errors in the obtained global parameters. The discretization errors of digitizers are $2 - 5\,\text{gauss}$, $0.5\,\text{mWb}$, and
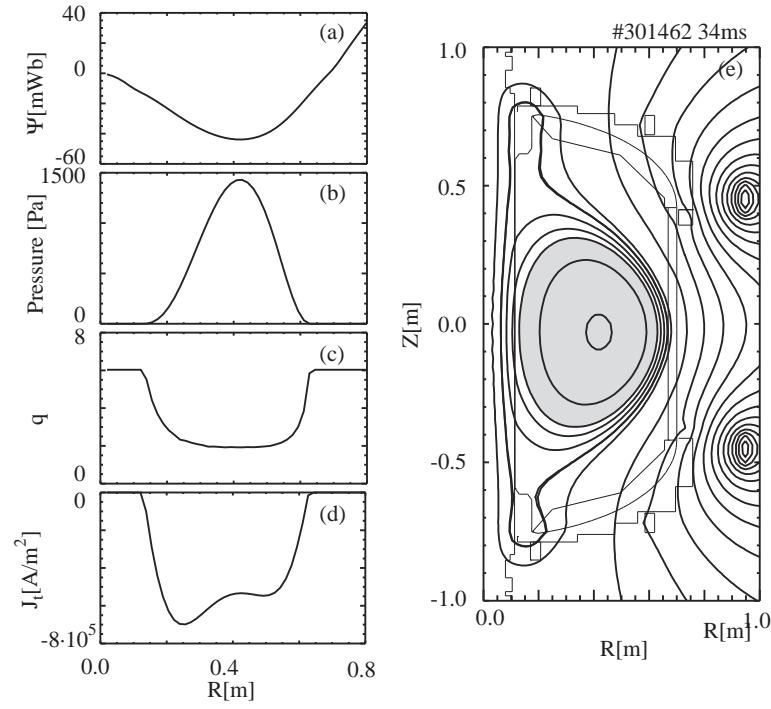
Figure 5.7: Reconstruction of #301462 at t = 35 [ms]. Profiles of (a) poloidal flux, (b) pressure, (c) safety factor and (d) toroidal current density, and (e) contour of the poloidal flux. The hatched region indicates the plasma.
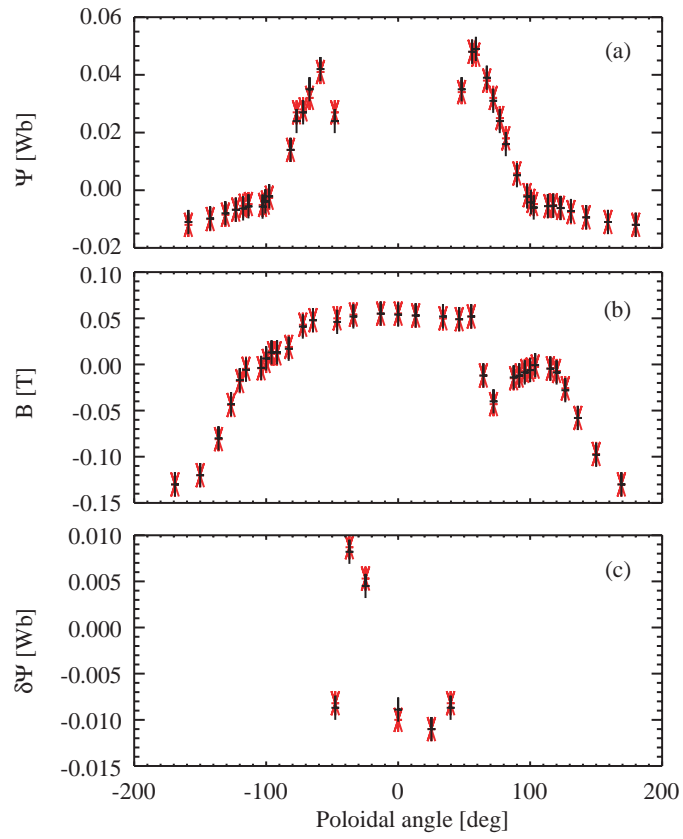
Figure 5.8: Comparisons between measured (black) and fitted (red) value of (a) flux loops, (b) pickup coils, and (c) saddle loops.

Table 5.2: Fluctuating error caused by discretization.

	R[m]	z[m]	$a[m]$	β_p	β_t	β_N	ℓ_i	E_k[J]	E_m[J]
Average	0.42	-0.029	0.25	0.19	0.017	0.98	0.64	420	920
$\sigma[\%]$[1]	0.17	3.3	1.5	6.8	5.5	7.1	1.7	6.2	1.5

[1] the standard deviation divided by the average.

Table 5.3: Error caused by misalignment of pickup coils.

	R[m]	z[m]	$a[m]$	β_p	β_t	β_N	ℓ_i	E_k[J]	E_m[J]
Average	0.42	-0.029	0.25	0.19	0.016	0.93	0.64	402	920
$\sigma[\%]$	0.29	3.0	2.4	11.5	9.5	12.1	3.0	11.	2.3

$60\,\mu$Wb for pickup coils, flux loops, and saddle loops, respectively. This kind of error results in random fluctuations of the global parameters obtained by a reconstruction. To evaluate the fluctuation, reconstructions were performed using the signals that were added artificial error, whose standard deviation corresponded to one bit. Table. 5.2 summarized the evaluated fluctuations. The fluctuation of geometrical parameters, such as R, z, and a are small, confirming the considerable accuracy of the boundary determination by the reconstruction. Since we averaged 10 digitization points in daily reconstruction analysis, resultant fluctuations would be decrease by a factor of 3 from the tabled value, leading the fluctuation in E_k of about 2 %.

Another possibility is misalignment of the magnetic sensors. The misalignment, presumably, would not cause fluctuations in the global parameters but results in either always smaller or always larger evaluation of them. Hence, this error may be more serious than the previous one for the absolute value evaluation. But its effects on the evaluation of EBW heating efficiency would be limited. Table 5.3 shows the change of global parameters, when we assums random misalignment of 3 mm for the pickup coils. Because of their design, the misalignment of the flux loops and the saddle loops is expected to be smaller and is ignored in the present consideration. Evaluation was performed in a similar manner as Table 5.2. Again geometrical parameters shows good stability. The evaluation of E_k turns out to decrease by about 5 % in average and its standard deviation is about 11 % of average E_k.

A few flux loops shows exceptionally high disagreement corresponding ~ 4 bits. This flux loops are either near the top and bottom of center stack or the flange connecting the upper dome and the cylinder part of the vacuum vessel and compensating conductor. Hence, the bigger errors are probably caused by the eddy currents induced on the near-by conductors. However, the exclusion of such sensors from the fitting results in only $\sim 1\%$ change in
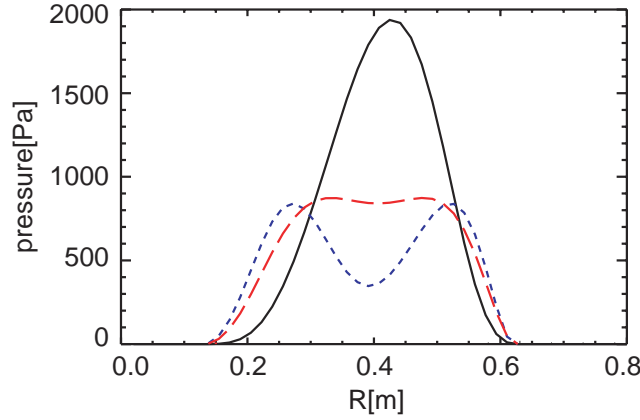
Figure 5.9: Pressure profiles of equilibria with (black line) $q_0 = 1.66$, (red dashed line) $q_0 = 2.02$, and (blue dotted line) $q_0 = 2.52$.

E_k. Disagreement in I_p is about 5%, which is always observed and probably because of an error in the calibration of the I_p Rogowski coil sensitivity.

Approximating $p(\psi)$ and $f(\psi)$ in a certain functional form is also source of error. In fact, the reconstruction of a very early phase of discharge usually fails to converge. It is probably because the current profile in such period is too hollow to be represented by the assume functional form. We added the restriction on the central safety factors q_0 and saw how estimated global parameters change. Table 5.4 lists the cases when we change q_0 by about ± 0.5. Figure 5.9 shows the pressure profiles for two extreme cases in this range. In $q_0 = 2.02$ case, the central pressure becomes nearly flat and it become even hollow when $q_0 = 2.52$, while the profile is rather peaky for q $= 1.66$ case, as shown in Fig. 5.9. By further decreasing q_0, it was observed that pressure in the outer half radius negative, indicating $p(\psi)$ is too peaky to be represented by the assumed functional form. Hence, excluding the hollow pressure profile case, it is inferred that global parameters including E_k are mostly unaffected by changing q_0. In slightly higher I_p discharges, we observed n=1, m=1 MHD mode activities. The occurrence of mode activity means $q_0 \leq 1$. q_0 of reconstructed equilibria at the onset of the activity is $1.1 \sim 1.4$, which is consistent with the possible range of q_0 variation shown here.

Table 5.4: Equilibria obtained by changing $q_0 (n_{\mathrm{p}} = 2, n_{\mathrm{ff}} = 2)$.

q_0	R[cm][1]	z[cm]	$a[cm]$	β_{p}	$\beta_{\mathrm{t}}[\%]$	β_{N}	ℓ_{i}	E_{k}[J]	E_{m}[J]
1.66	43.0	-2.88	26.2	0.198	1.63	0.979	0.676	424	964
1.92	41.9	-2.92	26.2	0.197	1.62	0.974	0.675	421	963
1.99	41.5	-2.92	26.2	0.197	1.63	0.978	0.674	422	959
2.08	41.1	-2.94	26.2	0.199	1.64	0.984	0.672	423	954
2.20	40.6	-2.94	25.3	0.200	1.65	0.980	0.669	424	948
2.52	39.3	-2.95	25.3	0.205	1.70	1.001	0.654	435	927

[1] Major radius of magnetic axis.

5.2   Langmuire probe

Langmuir probe [132] is a simple diagnostic that measures the dependence of the current flowing in the metal probe inserted into a plasma on the potential applied to the probe. In the potential range where electrons are being repelled, the electron current i_{e} and the ion saturation current i_{is} taken by a Langmuir probe are expressed by

$$i_{\mathrm{e}} = A n_{\mathrm{e}} e \sqrt{\frac{kT_{\mathrm{e}}}{2\pi m_{\mathrm{e}}}} \exp\left(\frac{e(V - V_{\mathrm{s}})}{kT_{\mathrm{e}}}\right), \tag{5.7}$$

$$i_{\mathrm{is}} = 0.61 A n_{\mathrm{e}} e \sqrt{\frac{kT_{\mathrm{e}}}{m_{\mathrm{i}}}}, \tag{5.8}$$

where A is the surface area of the probe, n_{e} is the electron density, m_{e} is the mass of electron, kT_{e} is the electron temperature in eV, V is the probe potential, and V_{s} is the plasma (space) potential. The electron temperature is measured from the slope of the characteristic curve, and the electron density is measured from the ion saturation current and the obtained electron temperature.

On TST-2@K, a movable Langmuir probe is installed that measured i_{is} profiles in the peripheral region in a shot by shot manner. In order to measure how the local limiter (Sec. 5.5) steepen the density profiles in front of the RF antennas, an array of Langmuir probes is also installed. Figure 5.10 shows a photo of the local limiter and expanded illustration of the Langmuir probe inside the local limiter. The array consists of 13 Langmuir probes that arranged to measure at the different distance from the edge of the local limiter. However, because of the limitation of the circuits, only three probes were simultaneously measured.
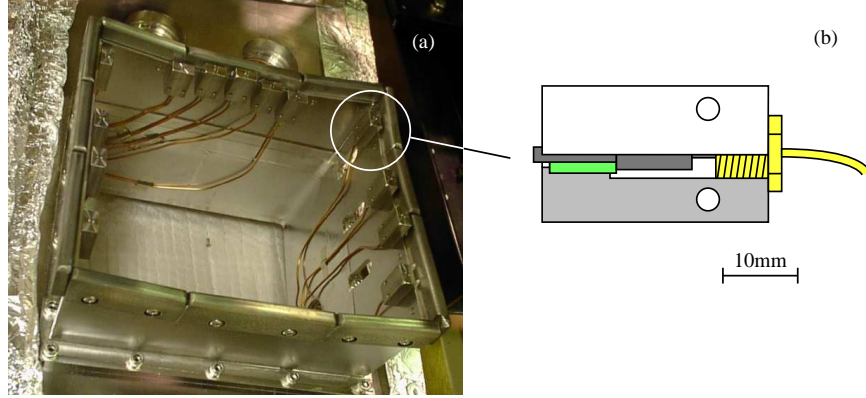
Figure 5.10: A photo of Langmuir probes located inside the local limiter and a closed picture of a probe head.

5.3 Microwave diagnostics

Though the probe diagnostic is convenient, it can only be applied to the plasmas that the probe can survive. This means the probe diagnostic is limited to the edge of TST-2 plasmas and one must rely on other techniques to diagnose the core region of plasma. In TST-2, two microwave diagnostics, namely an interferometer and a combined instruments of radiometer and reflectometer (radio-reflectometer), are used to measure the line averaged density and the electron temperature profile, respectively.

5.3.1 Interferometer

Figure 5.11 shows schematic of an heterodyne interferometer used in TST-2. Interferometer makes use of the phase delay of the wave that have propagated through a plasma. Using $\theta = \pi/2$ in Eq. 3.34, a refractive index for a perpendicularly propagating O-mode is given by

$$n^2 = 1 - \frac{\omega^2}{\omega_{\mathrm{pe}}^2}.$$

$$(5.9)$$

When the wave frequency is sufficiently high ($\omega \gg \omega_{\mathrm{pe}}$), the total phase delay φ that appears between the probe and the reference signals is expressed by

$$\varphi = \int \omega/c(n^2 - 1)dr \simeq \int \frac{1}{2} \frac{e^2}{\epsilon_0 m_{\mathrm{e}} \omega c} n_{\mathrm{e}}(r) dr$$
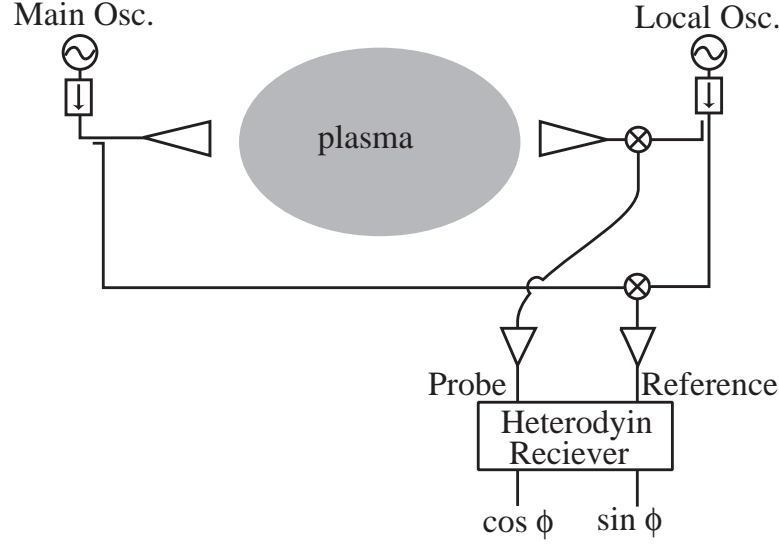
$$(5.10)$$

Figure 5.11: Schematic diagram of an interferometer

where the integration is taken along the microwave chord through a plasma. The heterodyne receiver is a I/Q demodulator, which convert the phase delay into $\sin\varphi$ and $\cos\varphi$.

In TST-2, the microwave chord is the vertical line crossing the plasma at R = 0.38m. Several choice of frequency and phase detection scheme was tested at Hongo campus, including 50GHz amplitude modulation (AM) interferometer and 104GHz heterodyne interferometer. At TST2@K, 150GHz heterodyne interferometer was used.

5.3.2 Radio-reflectometer

When a wave is absorbed by a plasma sufficiently, the thermal emission of such a wave from the plasma is considered as black body. The intensity of black body emission power per unit area per unit solid angle per unit angular frequency, $I(\omega)$, is given by Planck's radiation formula, and, at sufficiently high temperature ($\hbar\omega \ll T$), can be approximated as follows (Rayleigh-Jeans approximation),

$$I(\omega) = B(\omega) = \frac{\hbar\omega^3}{8\pi^3 c^2} \frac{1}{e^{\hbar\omega/T} - 1} \simeq \frac{\omega^2 T}{8\pi^3 c^2}. \tag{5.11}$$

Electron cyclotron emission from fusion plasma is in the range of microwave frequency and Rayleigh-Jeans is an excellent approximation. Since Eq. 5.11
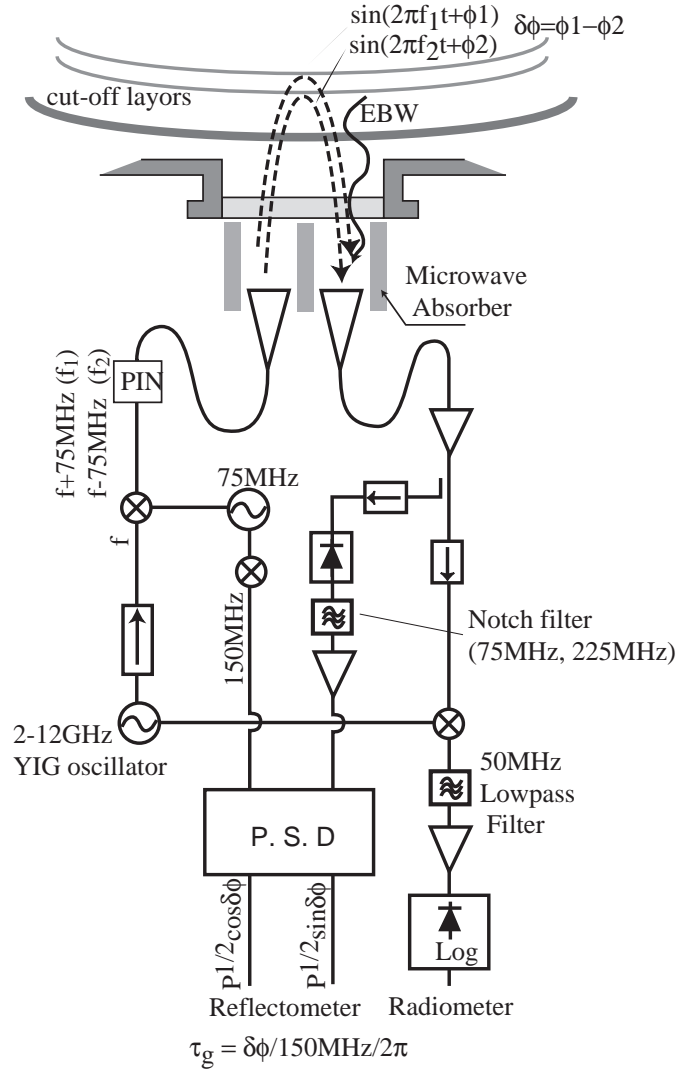
Figure 5.12: Block diagram of the radio-reflectometer. The frequency coverage is from $5 - 12\,\mathrm{GHz}$ corresponding a part of the fundamental, the 2nd and the 3rd harmonic emission from TST-2.

depends only on the temperature, measurement of electron cyclotron emission (ECE) by an absolutely calibrated radiometer become one of standard temperature diagnostics in fusion plasma experiments. The theoretical investigations of ECE are found in Ref. [133, 134] and the first experiment was carried out by Costley [4].

Similarly, since the optical thickness of EBW emission is sufficiently high, its emission can be considered as black body, providing a possibility of a electron temperature measurement [11]. However, in ST like TST-2, the cyclotron emission first propagates as a an EBW and need to be mode-convered to an electromagnetic wave before leaving a plasma. Hence, it is necessary to know the efficiency of the MC in order to estimate the EBW emission intensity from the measured intensity. As described in Sec. 3.5.4, the MC efficiency of the X-B MC scenario is determined by the density scale length at the upper hybrid resonance layer. A radio-reflectometer is a combined instrument of the radiometer that measures the emission intensity and the reflectometer that measures the density profile. In order to measure the density gradient of the region where the wave received by the radiometer is mode-converted, both radiometer and reflectometer should share the same receiving antenna. The difficulty of sharing is that the probing wave of the reflectometer may be detected by the radiometer. Using a different wave polarization for the radiometer and the reflectometer may offer a solution. However, the reflected wave from the plasma was found to contain a nearly 10% cross-polarized component. A better way is to use two frequencies and to make the frequency difference greater than the radiometer bandwidth. Hence, we employ the amplitude modulated reflectometry. This combined instrument was first developed by the author and was named "radio-reflectometer" [18].

A block diagram of the radio-reflectometer is shown in Fig. 5.12. It has a single microwave YIG oscillator (Micro Lambda, MLOB-0212PA) that is fed to two mixers (Mugnum, MM93PG-40). The first one is used to generate probing waves that are amplified to power levels of about 15 dBm and fed to the ridged horn antenna (A. R. A., DRG-5018/A). The reflected waves and the EBW emission are received by the second ridged horn antenna, amplified by 33 dB and fed to the second mixer and the diode detector (Agilent 8473C). The second mixer is used to detect the EBW emission. Since the bandwidth of the mixer IF port is 300 MHz, the mixer output contains the intense reflected wave components at DC, 75 MHz and its harmonics, besides the EBW emission. A 50 MHz low pass filter and a 3MHz high pass filter at the input stage of the logarithmic amplifier are used to eliminate the reflected wave components and reduce the radiometer bandwidth to 100 MHz (Double Side Band detection). Finally, the filtered signals are detected by the logarithmic amplifier (Analog Devices AD8307). The radiometer is absolutely calibrated

using liquid nitrogen [135].

The diode detector is used to detect the beat signal between two probing waves at 150 MHz. Contributions from mixing other harmonics generated at the first mixer such as $f + 150$ MHz and f are less than -30 dB in power and are negligible, where f is the frequency of the YIG oscillator. Notch filters are used to eliminate other harmonics such as 75 MHz and 225 MHz. With the local signal generated by the frequency doubler, the phase sensitive detector (P. S. D. : R&K, PSD-2C) performs a quadrature phase detection and the phase delay of the beat wave is obtained.

The antenna needs to be located about $60 - 90$ cm away from the vacuum window, because of the following two reasons. The first reason is to suppress the interference effect of the reflectometer. The second is to receive the emission generated only by the B-X-FX scenario. Using a mock-up vacuum vessel shows, 60 cm was found to be sufficient to restrict $n_\parallel$ less than 0.2, where no optimum $n_\parallel$ exists for the B-X-O which generates the elliptically polarized O-mode emission.

5.4 Radiation diagnositcs

Radiation from a plasma is caused by acceleration of electrons by ions (free-free), recombination of free electrons and ions (free-bound), and transitions between various electronic energy levels in atoms. The former two processes contribute to continuum in the energy spectrum, while the last process produces narrow spectral lines. The continuum covers a wide range of energy from the plasma frequency to frequencies corresponding to the electron temperature. On TST-2, soft X-ray emission is used for diagnosis.

5.4.1 Continuum spectra

Radiation by free-free transitions per unit volume per unit solid angle per unit angular frequnecy from an isotropic Maxwellian plasma of temperature T_e is expressed as

$$P(\omega) = n_e n_i Z^2 \Big(\frac{e^3}{4\pi\epsilon_0}\Big)^3 \frac{16\pi}{3\sqrt{3}m^2c^3}\Big(\frac{2m_e}{\pi k_b T_e}\Big)^{1/2} e^{-\hbar\omega/k_b T_e}\bar{g}, \qquad (5.12)$$

where $e^{-\hbar\omega/k_b T_e}\bar{g}$ is the Maxwellian-averaged Gaunt factor. In the high energy range ($\hbar\omega \geq k_b T$), the continuum (both free-free and free-bound radiations) has a strong exponential dependence on ω, and this dependence is used for T_e measurement. In TST-2, a pulse height analysis of photons over 1 keV was performed using a Si(Li) detector. Figure 5.13 shows an example of energy
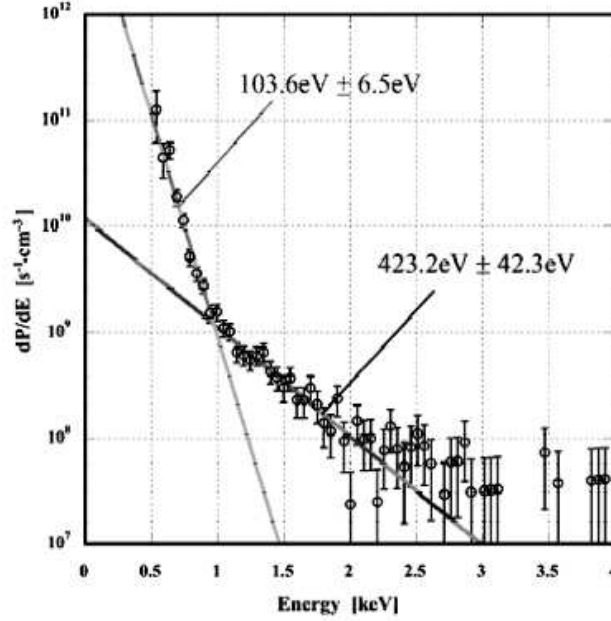
Figure 5.13: Energy spectrum of soft X-ray emission from TST-2 [136].

spectrum obtained from a discharge with $I_\mathrm{p} = 80\,\mathrm{kA}$ and $\bar{n}_\mathrm{e}L = 5 \times 10^{18}\,\mathrm{m}^{-2}$. Not only the slope of the spectrum but also the entire shape of the spectrum was used in the analysis, and T_e was estimated to be 300–400 eV [136].

5.4.2   AXUV and SBD monitors

In order to detect photons in various energy ranges, an AXUV detector and four SBD diodes were installed on the midplane of TST-2. These detectors view the entire plasma core region. The AXUV detector [137] developed by International Radiation Detectors, Inc. is a silicon p-n junction photodiode. The AXUV diode detects photons over a wide range of energy from vacuum ultraviolet to soft X-ray spectral regions. Since it has nearly constant conversion efficiencies of $0.2 - 0.25\,\mathrm{A/W}$ in the energy range of $1 - 6000\,\mathrm{eV}$ and high temporal resolution in the microsecond range, it is widely used for bolometry and impurity line observation [138, 139, 140]. The SBD detector used in TST-2 is Ortec model CR-017-050-100 partially depleted surface barrier diode, previously used for soft X-ray measurements on the REPUTE-1 reversed field pinch [141].

Either a 10 μm Be filter or a polypropylene filter with two different thicknesses is placed in front of SBD diodes. The AXUV detector and one SBD de-
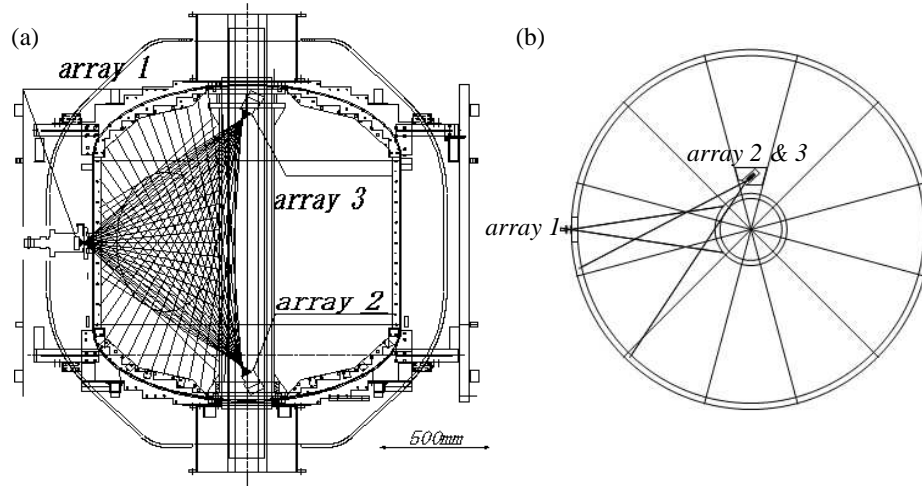
Figure 5.14: Locations of PIN photodiode arrays; (a) poloidal cross-sectional view, and (b) view from the top of the vacuum vessel.

tector was used without a filter. The Be filter cuts photons with the energies of less than 1 keV, while polypropylene filters cut vacuum ultra violet photons. Electron-hole pairs generated in these detectors are converted to a voltage signal using current-voltage converters and are recorded by AURORA-14 CAMAC transient recorders.

5.4.3 PIN diode array

Four sets of 20-channel positive-intrinsic-negative (PIN) photodiode arrays were installed. These arrays view the plasma through pin holes (pin hole camera) and measure profiles of soft X-ray emission. These diode arrays were absolutely calibrated using a storage ring at the KEK Photon Factory. The quantum efficiency of nearly 100% was obtained in the energy range 400–1000 eV [142, 143].

Figure 5.14 shows schematically the locations of arrays and their lines of sight. Three arrays were arranged to view nearly the same poloidal cross section of the plasma. The fourth array (not shown in the figure) was located on the midplane port which is 120° away toroidally from the midplane array shown in the figure. In order to obtain a large viewing angle, the arrays viewing the plasma from the top and the bottom of the torus were not mounted directly on vacuum port flanges. Instead, they were located very close to the ends of the center stack as shown in Fig. 5.15. These arrays were mounted on I-V converter boards and output photon currents were converted to voltage
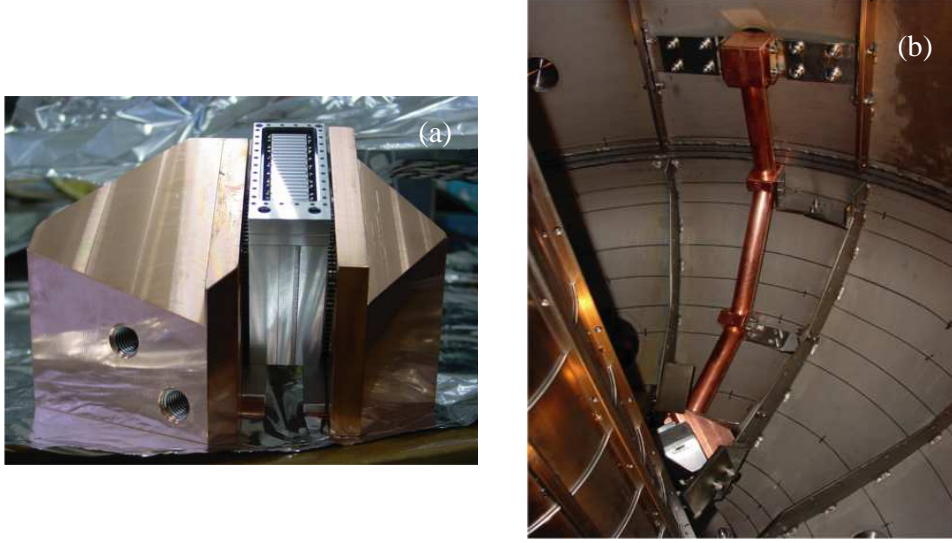
Figure 5.15: Photos of PIN photodiode array (a) mounted on an heat sink, and (b) installed in the vacuum vessel with an in-vessel cable cover tube.

signals immediately in order to reduce electromagnetic noise. In-vessel cable assembly was covered by a copper tubing for the same purpose.

5.5   EBW heating system

The microwave power source used for EBW heating experiments was the lower hybrid (LH) current drive system for TRIAM-1M, shown in Fig. 5.16. An RF oscillator generates a low power RF signal at 8.2 GHz, which is divided into 8 lines. After regulating phases and power levels, these signals are fed to eight klystrons (CPI VA-876S) and are amplified to 25 kW each. The total output power is 200 kW. To avoid arcing in the waveguides, they are pressurized by SF_6. Mechanical waveguide switches were installed at the output of VA-876S, and microwave power was delivered to TST-2 through eight vacuum windows. To ensure good transmission of high power microwave through the window, the window was designed carefully. A circular 99.9% purity alumina (Al_2O_3) window with a thickness of 2.5 mm and a diameter of 44 mm was used. The window was fitted into a metal O-ring that accomplished vacuum sealing, by a shrink fitting technique, and was placed in a pillbox cavity. Prototype windows with cavity lengths of 6.5 mm and 7 mm using 99.5% purity alumina showed voltage standing wave ratios (VSWR) of 1.2 and 1.18, respectively. In the final production, a cavity length of 6.8 mm
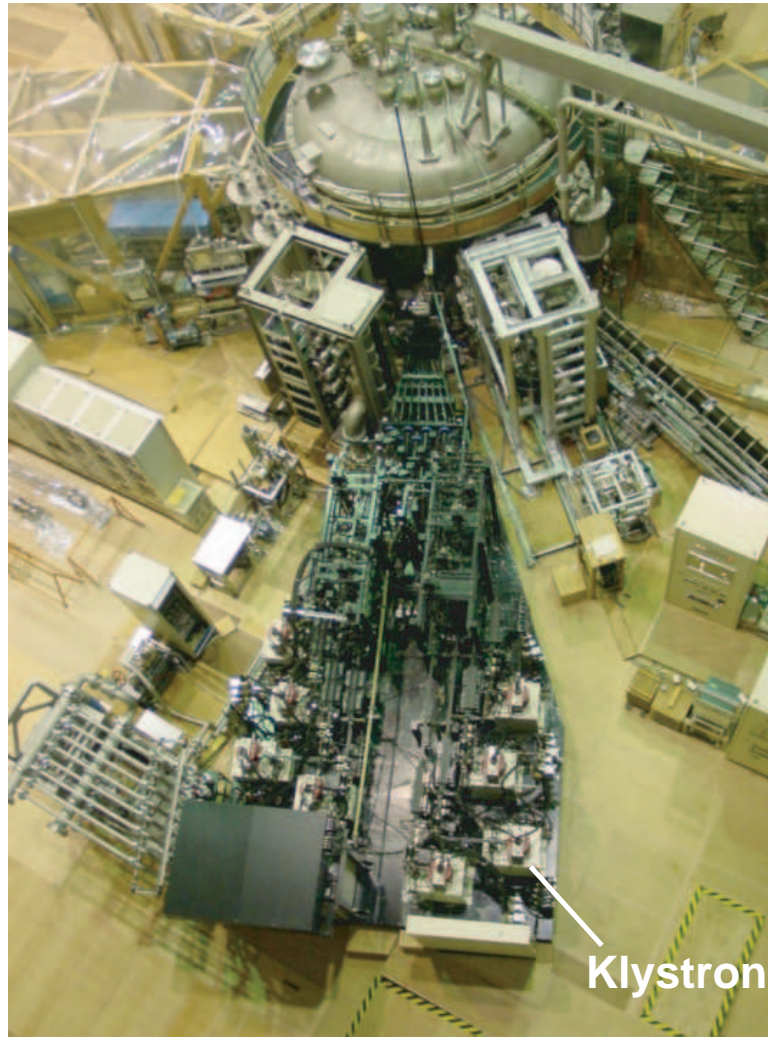
Figure 5.16: Top view of the TRIAM-1M LHCD system. Eight klystrons and complicated waveguides can be seen. The cryostat of TRIAM-1M can also be seen at the top of the photo. Connection to TST-2 located to the left of the photo is not installed yet.
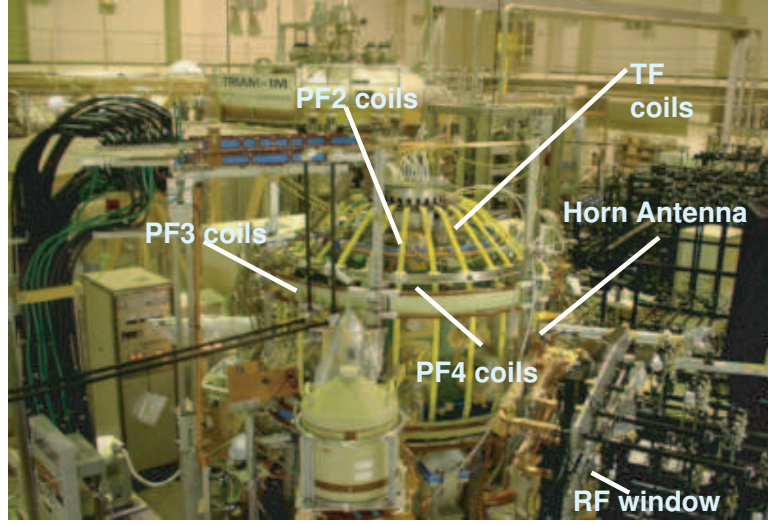
Figure 5.17: Photo of TST-2@K after completion of installation. The LH system is located right behind TST-2, from which RF power is transmitted to TST-2 through black waveguides and RF windows.

was chosen based of simulation, and VSWR of $1.03 \sim 1.07$ was confirmed. Figure 5.17 is a photograph of TST-2@K after completing connection of the LH system and installation of diagnositcs.

Figure 5.18 shows the location of the RF antenna, key diagnostics used in heating experiments, and the locations of resonance and cut-off layers. Microwave was launched from antennas located on the low field side of the torus, slightly below the midplane. The antenna array was surrounded by a CDX-U like local limiter made of molybdenum. The local limiter could be moved from $-15\,\text{mm}$ to $25\,\text{mm}$ relative to the fixed limiter located at $R = 0.64\,\text{m}$, where the negative direction is defined to be in the direction approaching the plasma. Langmuir probes were installed inside the local limiter to measure the density profile. The RF leakage monitor was used as an indicator of RF power that goes neither to the plasma nor back to the launcher. Typical ray trajectories calculated by a ray-tracing code are also shown in Fig. 5.18. The code calculates trajectories of the EBW generated at the edge MC layer until $99\,\%$ of the wave power is absorbed. The wave power is absorbed by electrons in the plasma core region by fundamental cyclotron damping.
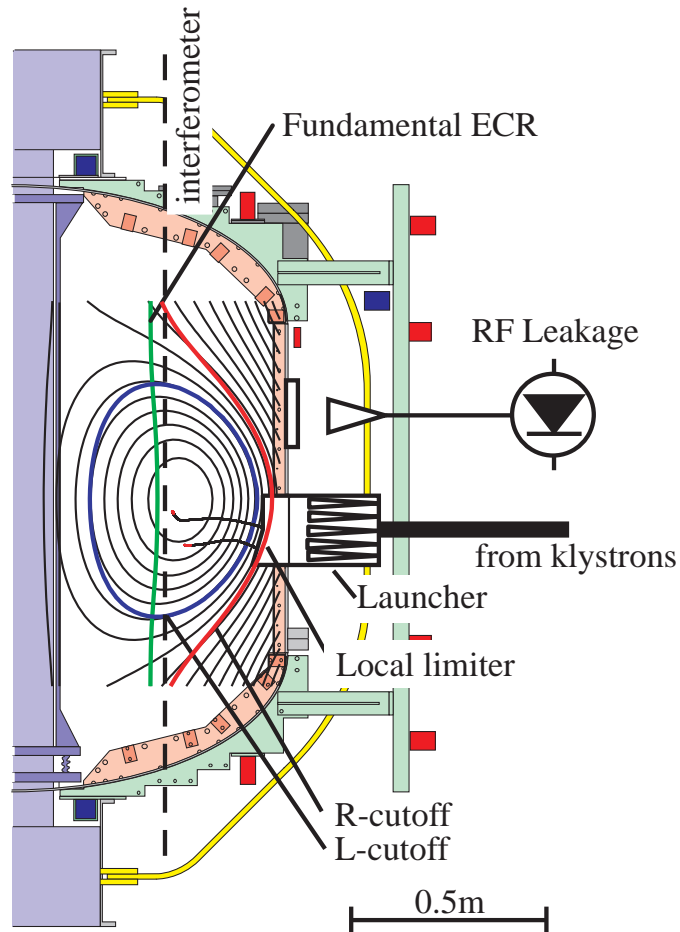
Figure 5.18: Schematic of the heating experiment. Typical equilibrium flux surfaces and locations of critical layers are shown. RF leakage monitor is installed 120° away toroidally from the launcher. Fundamental ECR (electron cyclotron resonance) is located slightly to the high field side of the magnetic axis.

Chapter 6

Experimental results

6.1 EBW receiving experiment

6.1.1 T_e from 3rd harmonic emisson

EBW receiving experiments were performed at Hongo Campus before EBW heating experiments. The radio-reflectometer described in Sec. 5.3.2 was installed at the low field side mid-plane of TST-2. The radio-reflectometer measures the intensity of radiation and the density profile near the mode-conversion (MC) layer. The radiation intensity is characterized by the radiation temperature (T_{rad}), which is the temperature of a black body that produces the same radiation intensity.Ohmic plasmas at toroidal fields of 0.15 to 0.2 T had plasma currents of 80–100 kA, discharge durations of $\sim$ 20 ms, and ion temperatures of 50–100 eV.

Typical example of the plasma current, 3rd harmonic EBW emission from the core region, and the phase delay of the reflectometer are shown in Fig. 6.1. There are several factors determining the evolution of T_{rad}. The first one is, needless to say, the evolution of T_e in the plasma core region. The second one is the evolution of the MC efficiency, which is determined by the edge density profile. For example, several sudden drops of emission coincided with reconnection events (indicated by gray hatch), but the reflectometer signal showed no obvious change. It is inferred that the emission drop represents the core temperature drop. The third effect contributing to the T_{rad} evolution is the plasma shape evolution. Fast CCD camera observed that the plasma was small at the beginning, grown up so large that it contacted both the high and low field side limiters, and then shrank towards the center stack. Because the equilibrium reconstruction used for later heating experiments was not available in the receiving experiment, we concentrate the T_{rad} around the plasma current maximum (18 ms), when the plasma shape is most certainly
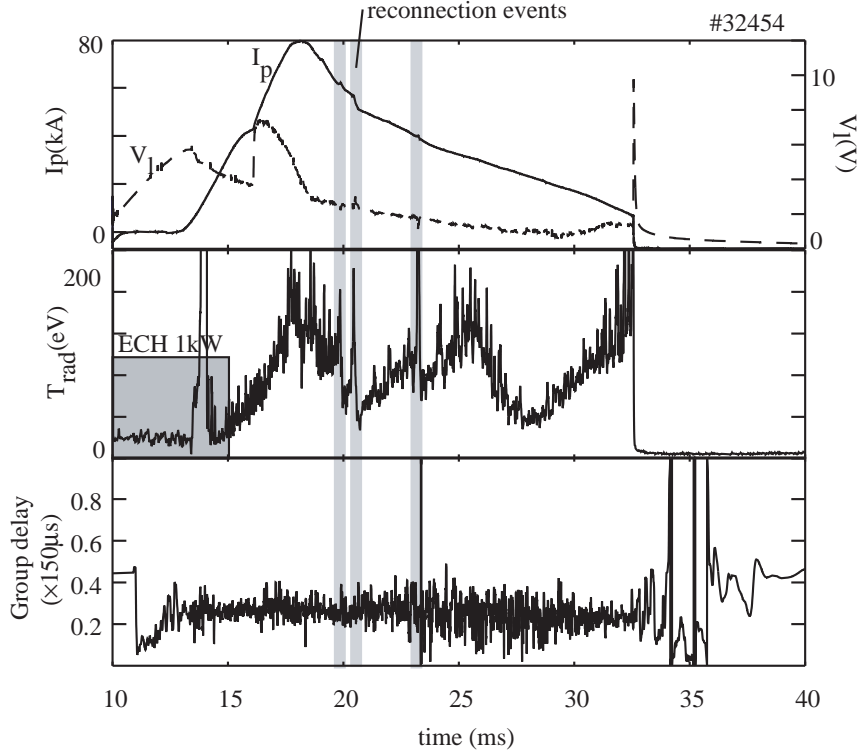
Figure 6.1: Temporal evolutions of the radiometer signal (radiation temperature) and the phase (group delay) measured by the reflectometer. The frequency of the radio-reflectometer is 11 GHz.

known, and the frequency was mapped to the radial position using a simple magnetic field profile inside the plasma.

Besides the reconnection events, the obtained T_{rad} and the group delay had continuous large fluctuations. It is known that there is a large density fluctuation at the plasma edge region where the EBW emission mode-converts to the X-mode. The fluctuation in the group delay represents directly such a density fluctuation. Since the density fluctuation fluctuates the MC efficiency, both the fluctuation of the MC efficiency and the core T_{rad} fluctuation could contribute to the T_{rad} fluctuation. Present diagnosis has no mean to separate these two effects. However, assuming the observed edge density fluctuation fluctuates the L_n in the theoretical MC efficiency curve (Fig. 3.7) in the same magnitude, the MC efficiency fluctuation alone is large enough to explain the observed T_{rad} fluctuation. Hence, in the following analyses, T_{rad} is averaged over a time interval of $0.6\,\text{ms}$, in order to reduce the effect of the MC efficiency fluctuation.
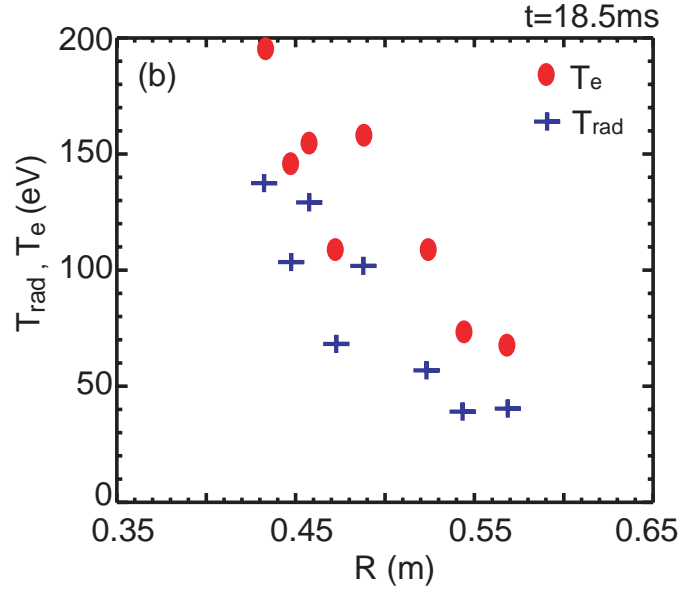
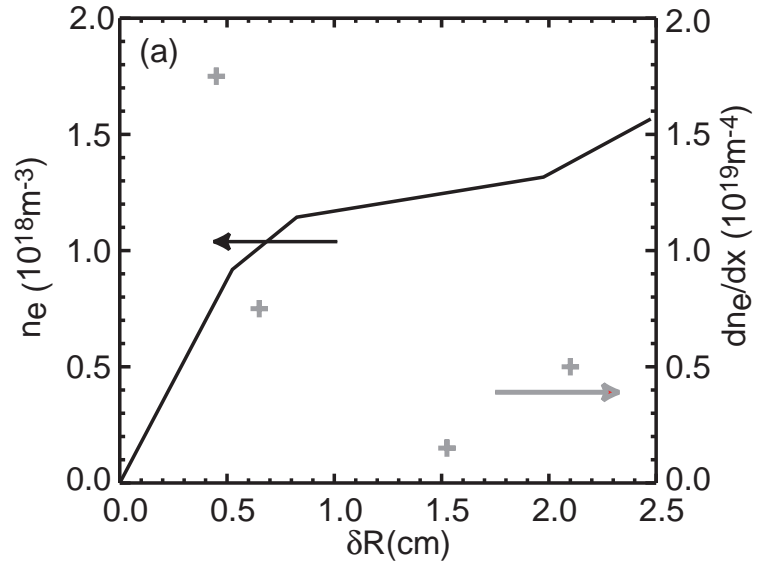Figure 6.2: T_{rad} and T_{e} profiles derived from 3rd harmonic emission.

Figure 6.3: Density profile around the UHR. δR represents the distance from the zero density.

The T_{rad} profile and the density profile around the UHR were measured by sweeping the YIG oscillator frequency on a shot by shot basis. The experiment was first carried out using the frequency range of 8–12 GHz, which corresponds to the 3rd harmonic emission. The results are shown in Figs. 6.2 and 6.3. It is shown that the radiation temperature from the core plasma is 100 to 150 eV, and decreases monotonically with minor radius. The density profile shows that the MC layer is, as expected, quite narrow (~ 2 cm) compared to the size of plasma. The MC efficiency was calculated using a 1-D cold plasma resonance absorption model. The calculated MC conversion efficiency is in the range $0.5 - 0.8$, leading to T_{e} in the core region of approximately 200 eV. The estimated T_{e} profile is overlaid on Fig. 6.2.

6.1.2   Fundamental and 2nd harmonic emisson

An interesting finding is the relationship between the reflectivity at the cutoff layer and the mode-conversion efficiency. In the resonant absorption model, the incident power is either reflected or absorbed and the absorbed power is consider to be the power that is mode-converted to the EBW. In Fig. 6.4, the reflectivity and the MC efficiency are compared, where the reflectivity is defined as the ratio between the reflected power with the plasma and that obtained when an aluminum plate covers the vacuum window. There is a clear relationship that the reflectivity is equal to $1 - C$, where C is the MC efficiency. This property can be used to evaluate the mode-conversion efficiency directly. Assuming this relationship, the estimated electron temperature profile obtained for the frequency range 5–8 GHz is shown in Fig. 6.5. Although the discharge condition such as the limiter major radius is not exactly the same between the discharges shown in Fig. 6.2, the magnitude of T_{e} is essentially same. In addition, the fundamental emission which is emitted from the other side of the magnetic axis was symmetric to the 2nd harmonic emission from low field side.

Though the T_{e} profiles measured by three harmonics look consistent with each other, it is clearly better to compare with a T_{e} measurement based on a different principle. Soft X-ray pulse height analysis (PHA) measures the energy spectrum of X-ray photons from the plasma, and T_{e} can be obtained from the slope of the continuum part of the spectrum. In TST-2, energy spectrum in the $1 - 20$ keV range was measured using a Si(Li) detector, and PHA indicated an electron temperature of $300 - 400$ eV. This is consistent with the EBW emission result, considering that T_{e} is estimated by averaging over a highly fluctuating T_{rad}.
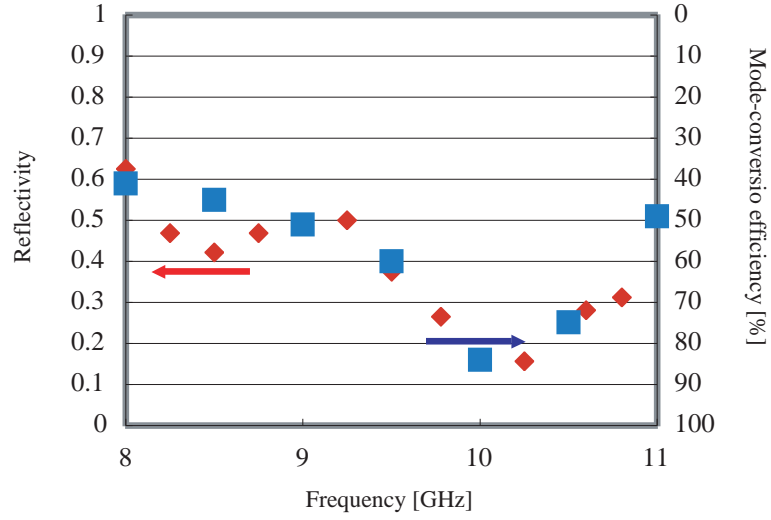
Figure 6.4: Comparison between the reflectivity and the calculated mode-conversion efficiency.
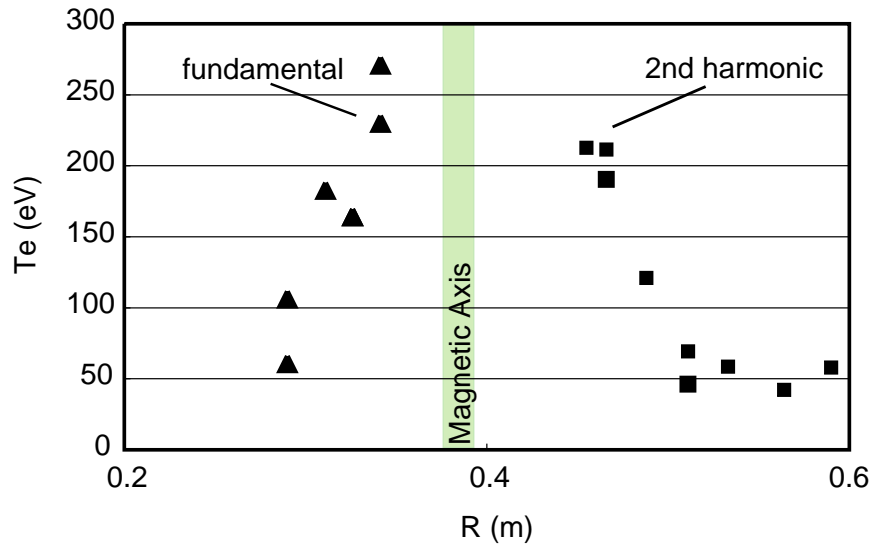

Figure 6.5: T_e profile evaluated from fundamental emission (high field side) and 2nd harmonic emission (low field side).

6.2   EBW heating experiment

6.2.1   Target plasma

The plasma discharge operation used in TST-2@K was largely different from those used in other TST-2 experiments including the EBW receiving experiment. Figure 6.6 shows a typical discharge sequence used in TST-2@K. The sequence is started with a gas puff at -100 ms and the vessel is filled to $1 - 2 \times 10^{-5}$ Torr. At this moment, magnets are electronically disconnected from power supplies by a mechanical switch because of safety. The connection is done from -90 to -70 ms. Exactly speaking, after this time, small voltages are applied to magnets, resulting in very small currents in the magnets and very small signals on the magnetic sensors. These do not affect the analysis of discharges discussed in this thesis. However, it seriously complicates the equilibrium analysis of low plasma current discharges, such as those discussed in [124]. The TF coil current starts rising from -63 ms to $20.5 - 21.5$ kA. The corresponding toroidal field is $0.26 - 0.27$ T at the geometrical center ($R = 0.38$ m). The TF coil current is kept constant till the end of plasma discharge.

The OH solenoid is used in series with the PF4 coil to reduce the stray field. It is precharged to 19 kA by 0 ms and is kept at a constant current until 15 ms ($\sim 4 \times \tau_{\text{eddy}}$), long enough for eddy currents induced in the vacuum vessel wall to die out. The PF3 coil (16 turns) current is precharged to about 200 A in order to cancel the remaining stray field that the PF4 coil cannot compensate. At 16 ms, the OH coil current begins to ramp down, producing a loop voltage of 5 V on average with ~ 3 $V_{\text{p}-\text{p}}$ fluctuations. Plasma break down takes place at around 18 ms, when the loop voltage becomes sufficiently high. At almost the same time (~ 16 ms), the currents in PF3 and PF2 (6 turns in series with PF5 coil) begin to increase, which provides a vertical field that balances the hoop force acting on the plasma.

At this time, the shot sequence was "pre-programmed", so waveforms of coil currents were predetermined. For EBW MC, the distance between the plasma outer boundary and the leading edge of the local limiter is a key parameter. Since the plasma outer boundary position is determined by the balance between the expanding force of the plasma itself and the repelling force from the PF coils, it changes as the plasma current evolves. It goes without saying that the evolution of the plasma current and a suitable PF coil currents cannot be predicted satisfactorily precisely before making a plasma discharge. Hence, when the plasma current has become sufficiently high, say 50 kA, the PF3 coil current is switched to the feedback control mode. Using a PID algorithm, a VME realtime controller regulates the PF3 coil current
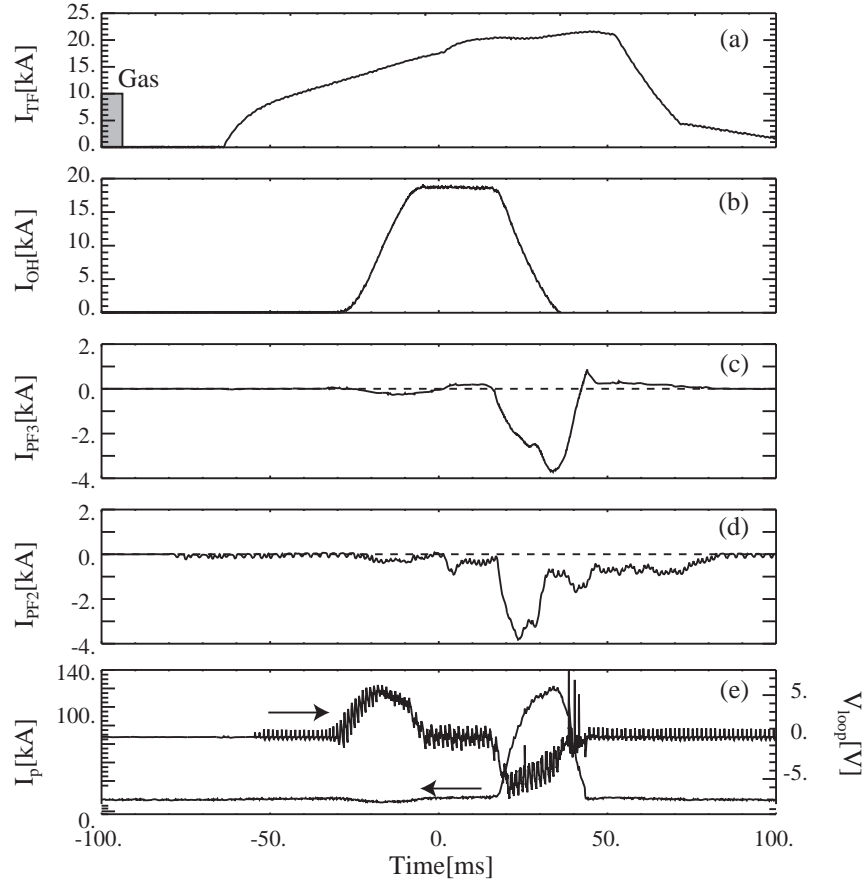
Figure 6.6: Shot sequence used for target plasma of heating experiment. (a) Toroidal field coil current, (b) Ohmic heating (OH) solenoid (in series with PF4) current, (c) PF3 coil current, (d) PF2 (in series with PF5) coil current, and (e) plasma current and loop voltage.
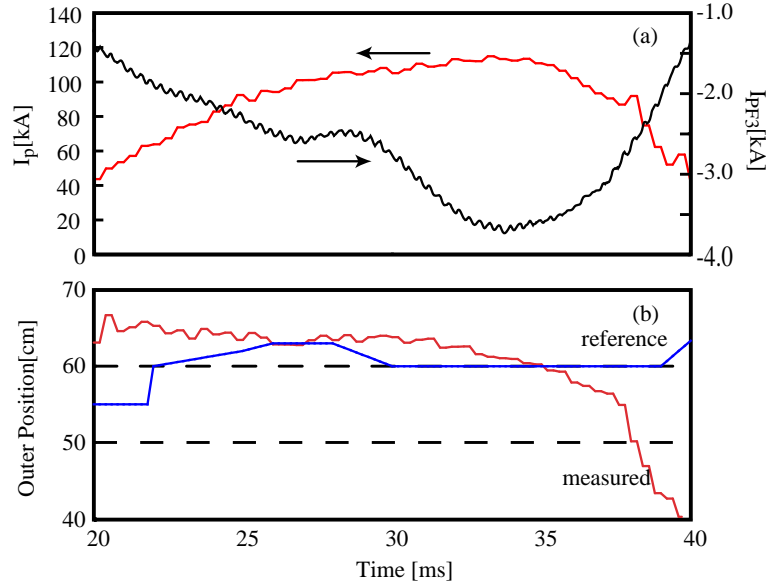
Figure 6.7: Temporal evolutions of (a) the plasma current and the PF3 coil current, and (b) the measured plasma outer radius and the reference position of the plasma outer radius.

so that the plasma outer boundary follows the reference position. To keep within a cycle of the VME controller, a very simplified formula based on only 6 magnetic sensors was used to calculate the plasma outer boundary position. Figure 6.7 shows an example of how the PF3 feedback works. Handing off to the feedback control is done at 22 ms. The PF3 current is increased (more negative) when the calculated outer boundary is outside the reference position (22 – 25 ms and 28 – 34 ms) and vice versa (after 35 ms). Since the loop voltage becomes nearly zero after 37 ms, the outer boundary could not be controlled even though the PF3 coil current was reduced at the maximum rate, and finally, the discharge is terminated. Accordingly, the period from when the feedback catches the plasma to when it loses it, 25–35 ms, was used for the heating experiment.

6.2.2   Antenna-plasma coupling

Good antenna-plasma coupling is important for safe operation of the RF system, since the reflected wave will increase the electric field in the launcher and waveguides, and may result in breakdown inside a waveguide or at a vacuum window. In addition, by changing the location of the local limiter,

Figure 6.8: Schematic of geometrical relation between plasma, antennas, and the local limiter.
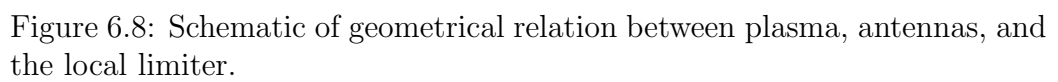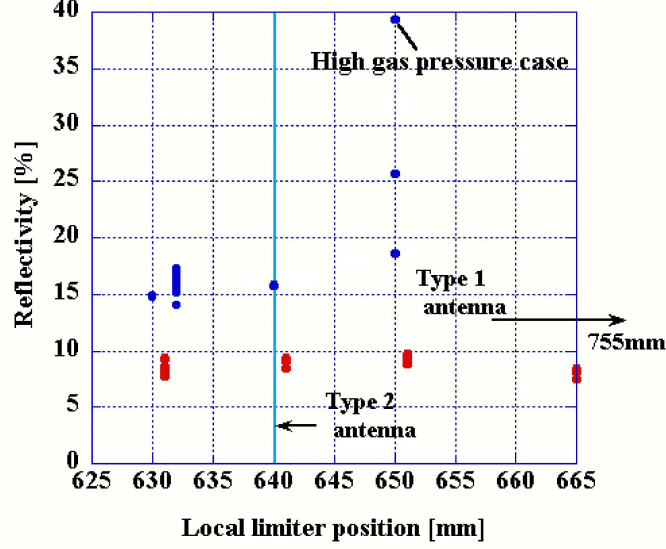
Figure 6.9: Dependence of antenna-plasma coupling on the location of the local limiter surface and the type of antenna.

the MC efficiency is expected to change. If the power that is not mode converted to EBW is reflected back to the antenna, such power must be detected as increased reflection at the antenna, which motivated us to the survey of antenna-plasma coupling.

The antenna-plasma coupling was studied with a variety of local limiter positions. Two types of antennas, horn antennas and straight WG antennas, were used to see the effect of antenna aperture. The geometry of the antennas and the local limiter is illustrated schematically in Fig. 6.8, and the results are shown in Fig. 6.9. Generally, good antenna-plasma coupling was observed for various local limiter positions. The straight WG antenna showed approximately 17% power reflection, while the horn type antenna showed about 10% reflection. Better coupling of the horn antenna is presumably attributed to its larger aperture. The increased reflection in discharges with exceptionally high fueling is most likely caused by breakdown just in front of the antenna.

It is noted that, in many discharges shown in Fig. 6.9, no effect of plasma heating such as the increase of the plasma stored energy was observed. The reflectivity is almost the same even in discharge with clear heating as discussed in the next subsection. This means that the MC efficiency cannot be evaluated from the antenna-plasma coupling, in clear contrast to the

radio-reflectometer result. This point will be discussed in a later subsection. Thanks to good antenna-plasma coupling, up to $140\,\mathrm{kW}$ of net (forward $-$ reflected) RF power was injected successfully.

6.2.3 EBW heating results

Figure 6.10 shows a plasma discharge in which a significant increase of the plasma stored energy was observed. The net RF power of $70\,\mathrm{kW}$ was injected from $31.5\,\mathrm{ms}$ to the end of the discharge. An outboard limited plasma with a plasma current of about $100\,\mathrm{kA}$ was maintained for several milliseconds. The line-averaged density $(\overline{n}_\mathrm{e})$, defined as the line-integrated density divided by the path length of the interferometer chord through the plasma, was $1 \times 10^{19}\,\mathrm{m}^{-3}$ at RF turn-on ($31.5\,\mathrm{ms}$), which is an order of magnitude above the cut-off density. At RF turn-on, a clear increase of the plasma stored energy (W_K) by 15–20 % was observed as shown in Fig. 6.10 (c). Since the ohmic heating power input is approximately $300\,\mathrm{kW}$ on average from $30\,\mathrm{ms}$ to $35\,\mathrm{ms}$, the increase of W_K corresponds to $45 - 60\,\mathrm{kW}$ of additional heating, assuming no degradation of energy confinement with power. The absorbed power can also be estimated from a break-in-slope analysis, which indicates that the heating power increased by $35 - 45\,\mathrm{kW}$ at RF turn-on. In addition, W_K saturated after about $1\,\mathrm{ms}$ after RF turn-on. Fitting the W_K time evolution after RF turn-on by an exponential function gives a time constant of $0.8 - 1.2\,\mathrm{ms}$.This time scale is similar to the energy confinement time of $1\,\mathrm{ms}$ just before RF turn-on. An increase of the line-averaged density was also observed, suggesting an increased particle source. According to the empirical scaling laws of the energy confinement time, such as Eq. 4.1 and 4.2, the increase of density tends to improve the energy confinement time. However, the time scale of the density increase is much longer than that of W_K and cannot be considered as the main cause of W_K increase. These results consistently indicate that the RF power heated the plasma with over 50% efficiency.

The electron densities measured by Langmuir probes installed inside the local limiter are shown in Fig. 6.10 (d). Probe (1), which is the closest to the plasma, is not completely shadowed by the local limiter, while probes (2) and (3) are completely shadowed by the local limiter. An electron temperature of $30\,\mathrm{eV}$ was obtained in a similar discharge by sweeping the voltage applied to probe (1) and this temperature was used to calculate the electron density from the ion saturation current I_s. The density scale length L_n inside the local limiter is shown in Fig. 6.10 (e). The measured L_n was about $6\,\mathrm{mm}$. Noting that the scale length naturally created outside the local limiter was about $30\,\mathrm{mm}$, the local limiter indeed shortened L_n, and $70 - 80\%$ MC is expected
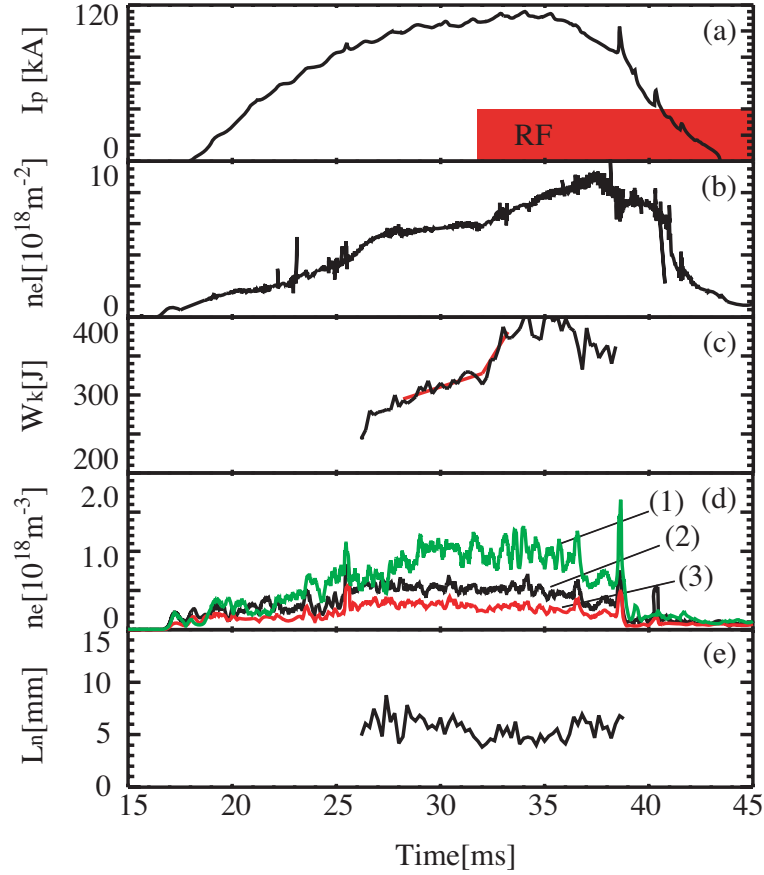
Figure 6.10: Plasma discharge with $70\,\mathrm{kW}$ of net RF power (#301462). (a) Plasma current, (b) line-integrated density $\overline{n}_{\mathrm{e}}l$ at $R = 0.38\,\mathrm{m}$ ($l \simeq 0.6\,\mathrm{m}$), (c) plasma stored energy, (d) densities measured at three locations inside the local limiter, and (e) density scale length.

from Fig. 3.7. Assuming the same T_e for all three probes introduces an uncertainty in the estimation of L_n. However, even if the temperature scale length (L_{T_e}) were assumed to be equal to L_n, L_n would only be 1.5 times larger than L_{I_s} and 30 – 40% MC is still expected. The observed increase of W_K is consistent with L_n between these two cases.

An indication of high energy electron generation was also observed. In the discharge shown in Fig. 6.11, RF power was injected from 31.5 ms to 41.5 ms into a target plasma with approximately 30% lower line-averaged density ($\overline{n}_e \sim 0.7 \times 10^{19}\,\mathrm{m}^{-3}$). A more complete set of diagnostics was operating. Shown in the figure are $n_e l$, H_α emission, radiated power P_{rad} (measured by an absolute extreme ultraviolet detector), and soft X-ray (SX, 1-10 keV) emission measured by a surface barrier diode with a beryllium filter, and the plasma stored energy W_K, all of which increased at RF turn-on. The increase of SX emission indicates that high energy (higher than the thermal energy) electrons are generated by EBW injection at the beginning of RF injection, although a direct electron temperature measurement was not available in this experiment. During the RF pulse, SX turned over at around 37 ms, while P_{rad} continued to increase, suggesting that the loss of heating may be caused by increased radiation. A step-function like response observed in H_α emission (0.6 ms rise time) indicates that some power is deposited directly in the plasma edge. The timing of the stored energy turn-over was approximately the same as the SX signal turn-over, indicating that heating is effective while high energy electrons are generated.

6.3 Discussion

6.3.1 Density dependence

The heating efficiency was lower in the lower discharge shown in Fig. 6.11. As shown in Fig. 6.11 (g), W_K increased from 150 to 170 J, by 13%, and the additional heating power estimated from the break-in-slope analysis is 6–15 kW, which is only 7–17% of the injected RF power. The degradation of heating efficiency can be explained by considering the effect of the shallow density gradient region outside the local limiter. Fig. 6.12 shows such an effect schematically. When the density at the front edge of the local limiter (limiter edge density, n_{edge}) is higher than the left hand cutoff density, the cutoff-resonance-cutoff triplet is located in the shadow of the local limiter as shown in Fig. 6.12 (a), in which the distance between two cutoffs is narrow. As the limiter edge density decreases, the left hand cutoff moves out of the shadow of the local limiter (Fig. 6.12 (b)). The distance between two cutoffs

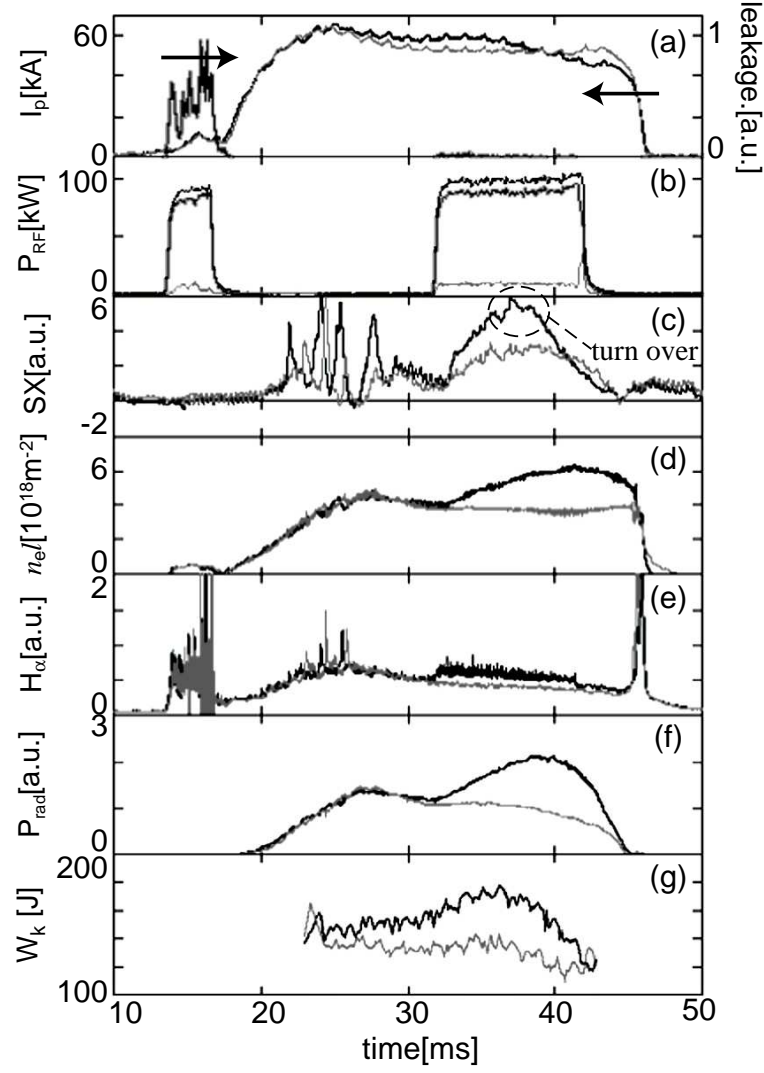Figure 6.11: Time evolutions of a discharge with 90 kW net RF injection (#302787 in black) and a similar discharge without RF power (#302788 in gray). (a) Plasma current and RF leakage power, (b) forward, reflected, and net RF powers, (c) SX (1–10 keV) emission, (d) line-integrated density at $R = 0.38$ m ($l \simeq 0.55$ m), (e) H_α, (f) P_{rad} (broadband radiation over the range 0.01–7 keV), and (g) plasma stored energy.
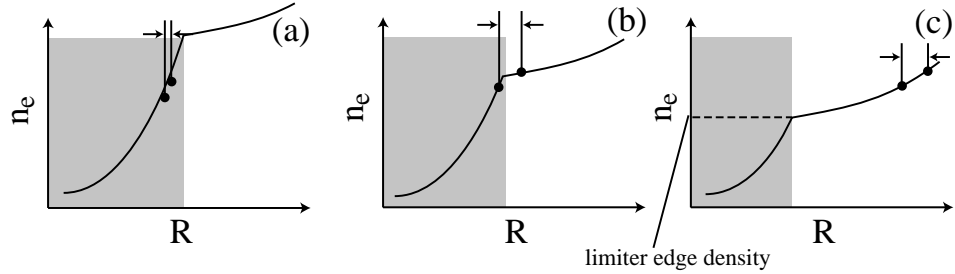
Figure 6.12: Density profile consisting of two regions with different density sclae lengths for different limiter edge densities. Two circles indicates the location of the cutoff layers, when the density at the front edge of local limiter is higher than the density of left hand cutoff (a), lower than the density of right hand cutoff (c), and between two cases (b).

Figure 6.13: Comparison between the calculated MC efficiency for a density profile shown in Fig. 6.12 and the observed heating efficinecy. The upper and lower bounds of the measured limiter edge density are based on the measured density at probe (1) and the density extrapolated to the limiter edge from probe (2).

increases, indicating that the triplet is radially stretched. In Fig. 6.12 (c), the limiter edge density become lower than the right hand cutoff density, and the triplet moves completely outside the shadow of the local limiter.

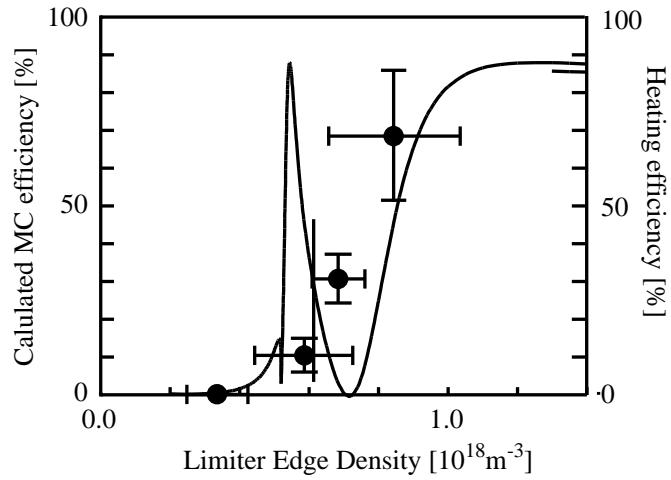In order to compare the radial stretch of the triplet and observed heating efficiency, the MC efficiency is calculated using L_n inside the local limiter ($L_{n-\mathrm{limiter}}$) chosen to be the optimum for MC and L_n outside the local limiter chosen to be $5 \times L_{n-\mathrm{limiter}}$, which is L_n measured by a Langmuire probe located outside the local limiter. Figure 6.13 shows the calculated MC efficiency as a function of the limiter edge density Note that the left hand and right hand cutoff density under the experimental condition (8.2 GHz and 0.18 T) is $1.3 \times 10^{18}\,\mathrm{m}^{-3}$ and $0.4 \times 10^{18}\,\mathrm{m}^{-3}$, respectively. When the limiter edge density is high enough, the efficiency shown in Fig. 3.7 is reproduced. As the limiter edge density decreases, the degradation of the MC efficiency occurs. The MC efficiency become negligible eventually, when the limiter edge density become lower the right hand cutoff density.

The experimentally observed heating efficiencies including the two discharges discussed in the previous section are overplotted in Fig. 6.13. (In a discharge with similar $n_e l$ to #302787, it was confirmed that n_{edge} was about 70% of #301462) The heating efficiency increases as the local limiter density increases, which is found to be consistent with the transition from the bad MC case (Fig. 6.12 (c)) to the good MC case (Fig. 6.12 (a)). The narrow peak at $n_{\mathrm{edge}} \sim 0.6 \times 10^{18}\,\mathrm{m}^{-3}$, which is caused by the resonance of the wave reflected by the two cutoff layers, was not observed experimentally. However, this peak is considered to be rather artificial and is not believed to be found in a real plasma. The position of the peak was observed to move sensitively by a slight change of L_n in numerical calculation. Because of large amplitude density fluctuations existing around the MC region, the MC curve in a real plasma is expected to be an ensemble average of the MC curves for different L_ns. Although the present data set lucks the information to predict the MC curve under the effect of the density fluctuations, such an averaging is expected to smear out the narrow peak, and the observed dependence of the heating efficiency on density is plausible.

6.3.2 Power deposition profile

Another evidence supporting the picture that the EBW generated by MC at the plasma edge travels to the plasma core and is absorbed by electrons comes from the SX emission profile measurement. As described in Sec. 5.4.3, three 20-channel PIN (positive-intrinsic-negative) diode arrays, viewing the plasma from the top, the bottom, and the low field side, are installed in TST-2@K. These arrays have no filter that limits the energy range, and
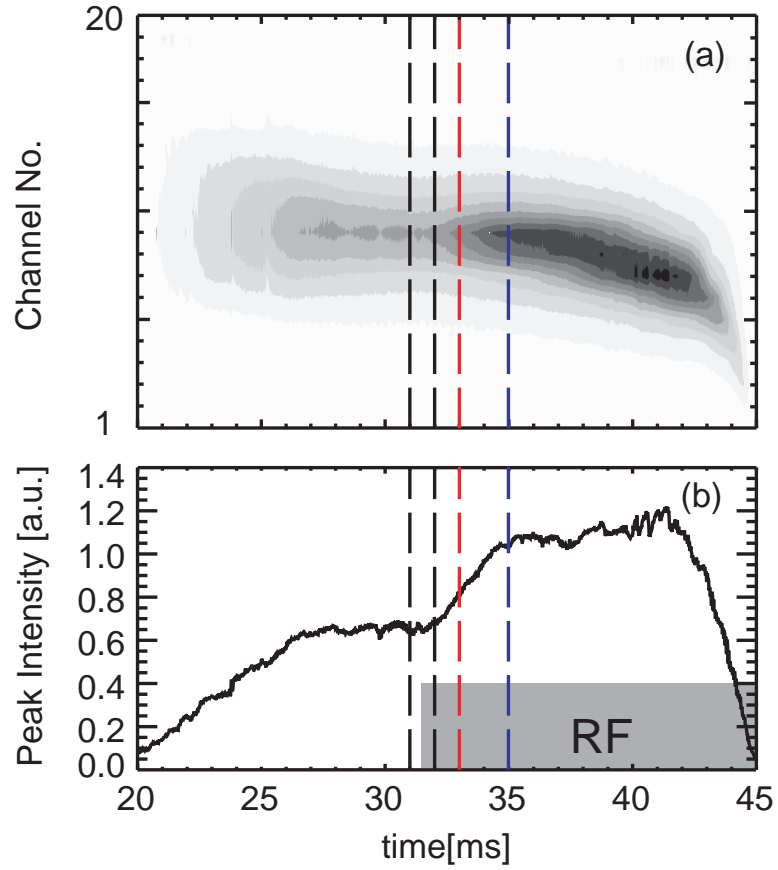
Figure 6.14: Evolution of mid-plane PIN diode array signal with RF. (a) Contour plot of PIN diode array signals, and (b) evolution of the peak intensity. Profiles at the times denoted by four dashed lines are compared in Fig. 6.16.
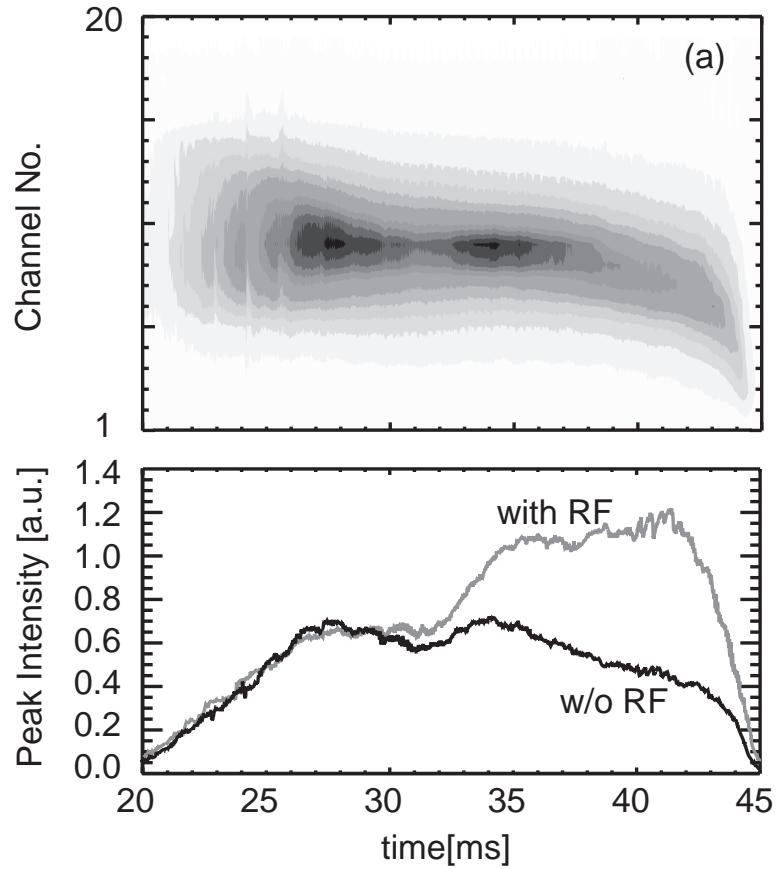
Figure 6.15: Evolution of the mid-plane PIN diode array signals w/o RF. (a) Contour plot of PIN diode array signals, and (b) evolution of the peak intensity, having the peak intensity with RF over-plotted for comparison.
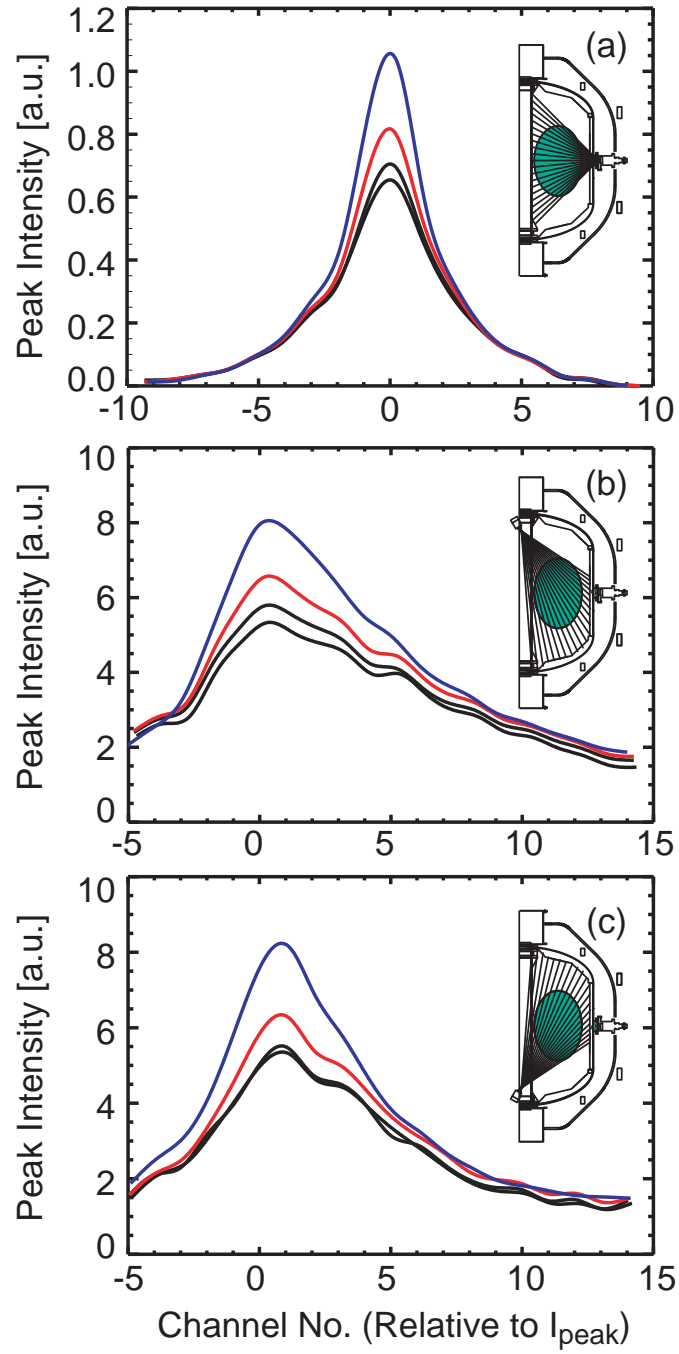
Figure 6.16: Evolutions of SX profiles measured by the PIN diode cameras viewing the plasma from mid-plane (a), top (b), and bottom (c) after the RF turn-on. Profiles at times indicated by the four dashed lines in Fig. 6.14 are compared. The horizontal axis are channel numbers relative to the peak of intensity.

are sensitive to a wide range of photon energies. Since multiple processes contribute to photon generation in a plasma, its output is not considered to represent some physical parameter, say T_e, directly. However, extracting the geometrical information of the change occurring in the plasma is still possible, and that is what we need here.

Figures 6.14 and 6.15 show the evolutions of the SX emission profile viewed from the low field side for #302787 and #302788, respectively. The movement of the intensity peak towards lower channels after 37 ms is in good agreement with the motion of the magnetic axis calculated by equilibrium reconstruction. In (b), evolution of the peak intensity is shown. The peak intensity becomes steady before RF injection, but starts increasing at RF turn-on in Fig. 6.14, while it stays at the same level in Fig. 6.15. In addition, the rise time is about 3 ms, which is similar in magnitude to the energy confinement time. In Fig. 6.14 (a), it is noted that a clear increase of emission takes place in channels viewing the plasma core region.

Two other PIN diode arrays viewing the plasma from the top and the bottom also show similar behaviors. Figure 6.16 shows the profiles at 4 time slices indicated by dashed lines in Fig. 6.14, showing significant increases of the signal only in central several channels. The major radius of lines of sight of these channels are calibrated using the data when plasma vertically moves, and it is confirmed that the channels view the plasma core region. Hence, the emission increase is localized in the plasma core region ($r/a \leq 0.4$), where the EBW is expected to be absorbed via electron cyclotron damping (Fig. 6.17). Exactly speaking, the lines of sight of the top and the bottom cameras draw curved lines on a poloidal cross section, since they view plasmas at an oblique angle in the toroidal direction (schematics on the figure do not reflect this effect), and determination of the major radius of the edge channel chords are not straightforward. Reconstruction of SX emission profile using computer tomography technique are currently underway.

An increase of the electron density observed after RF turn-on may change the EBW trajectory and move the power deposition towards the plasma edge. However, according to ray-tracing calculations, the effect of the increased density is not significant. Figure 6.17 compares RF deposition for the case with $n_e\ell = 4 \times 10^{18} \text{m}^{-2}$ (similar to the beginning of EBW heating, shown in red) and for the case with three times larger density (shown in green). The RF power deposition remains in the plasma core region for both cases. Absorption does move towards the plasma edge for the high density case, but the shift is small.
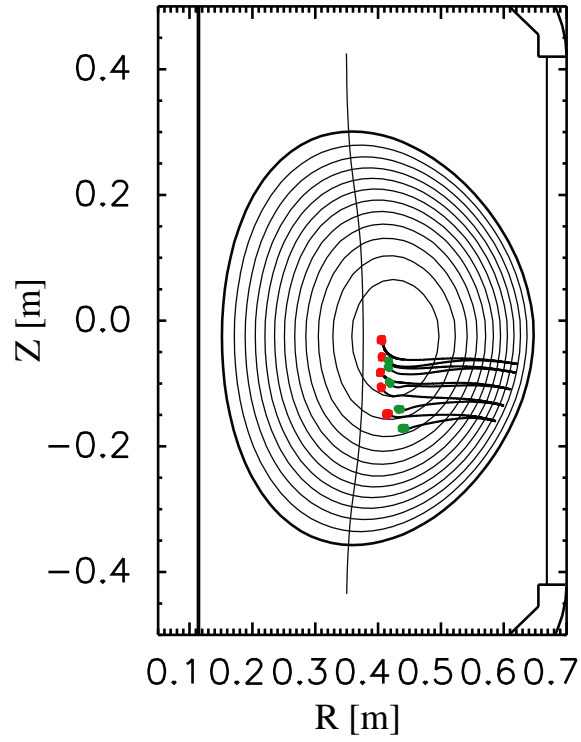
Figure 6.17: Comparison of ray trajectories for $n_e\ell = 4 \times 10^{18} \text{m}^{-2}$ and $n_e\ell = 1.2 \times 10^{19} \text{m}^{-2}$. The locations where absorption takes place for the two cases are indicated by red and green symbols, respectively.
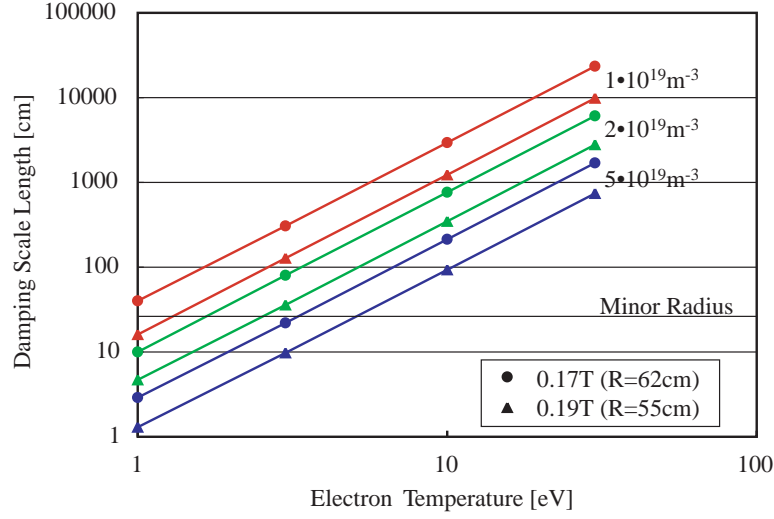
Figure 6.18: Scale lengths of collisional damping for arious densities and magnetic fields.

6.3.3   Missing power

A remaining question is where the power goes in the lower density case with poor core absorption. The power reflected back to the launcher was always small even when heating was poor. The fact that the area occupied by antenna surface was only 30% (for the type 1 antenna) or 6% (for the type 2 antenna) of the area inside the local limiter may be one reason. Because a reflected wave is scattered by density fluctuations, it may not come back to the launcher directly. However, it does not give a complete explanation. Since the surface inside the local limiter is mostly metal, a good reflector of microwave, there must be another mechanism that consumes the launched power.

The RF leakage monitor shown in Fig. 6.11 indicates that the RF power did not leak through the vacuum window during the plasma heating pulse. The monitor measured the leakage power at several vacuum windows installed at different poloidal angles relative to the RF launcher on a shot by shot basis, confirming that the RF power leaking through vacuum windows was negligibly small.

Hence, the launched power must be consumed somewhere inside the vacuum vessel. The H_α signal response indicates that some power is absorbed in the plasma edge region directly. By what process was the RF power absorbed at the plasma edge? One possibility is collisional damping. Figure 6.18 shows

calculations of the scale length of power absorption by collisional damping. In this calculation, $\text{Im}(k)$ is obtained from the dispersion relation, assuming a small imaginary part in frequency ($\text{Im}(f) = 1/\tau_{i-e}$, where τ_{i-e} is the electron-ion collision time). It is shown that collisional damping during a single pass through the plasma edge is not significant. However, multiple reflections between the plasma and the vacuum vessel wall may enhance edge absorption by this process significantly.

Parametric decay instability (PDI) is another possible cause of power absorption. If the incident wave (pump wave) electric field exceeds a certain threshold, the pump wave can nonlinearly excites two waves satisfying the matching condition: $\omega_p = \omega_1 + \omega_2$ and $\vec{k}_p = \vec{k}_1 + \vec{k}_2$, where the subscript p denotes the pump wave, while subscripts 1 and 2 denote the nonlinearly excited waves. In ionosphere heating experiments, a secondary electromagnetic wave generation called "stimulated electromagnetic emission spectrum" are observed [107, 108, 109]. A theoretical explanation of such a phenomenon is parametric excitation of a side band EBW [112] or electromagnetic wave [110] and a lower-hybrid decay wave by the EBW. Although PDI was observed in previous EBW heating experiments [84], the pump wave frequency was eight times higher than that used in this experiment and the MC scenario was also different, which should result in a different threshold power. Since the need for experimental observation of PDI was recognized, two Langmuir probes installed inside the local limiter used coaxial semi-rigid cables to transmit the high frequency signal. However, the measurement of high frequency components of the edge density fluctuation, tried in some discharges, did not give positive results. Although the experimental data to date cannot give definite conclusion, PDI is widely recognized as a possible RF power loss mechanism at the plasma edge, and should be investigated further in future research.

Chapter 7

Summary

7.1 Conclusion

In this thesis, the electron Bernstein wave was studied in ST plasmas, focused on its application to radiation temperature diagnostic and plasma heating. To conduct a series of experiments, a completely new spherical tokamak, TST-2, was designed and constructed. Significant improvements in plasma performance were achieved. Major achievements are:

- A new center stack extended operational regime up to $B_\mathrm{t} = 0.3\,\mathrm{T}$ (raised from $0.15\,\mathrm{T}$) and $\Psi_\mathrm{OH} = 130\,\mathrm{mVs}$ (increased from $25\,\mathrm{mVs}$).

- To cope with eddy currents induced on the new electrically continuous vacuum vessel, a suite of codes was developed to predict and diagnose the behavior of eddy currents, and was used to develop operational scenarios.

- A large number of magnetic sensors was installed for equilibrium reconstruction, which was used for the evaluation of the EBW heating efficiency. Magnetic diagnostics were also used for eddy current analysis.

- Plasmas with $I_\mathrm{p} \sim 100\,\mathrm{kA}$, $T_\mathrm{e} = 200\text{--}400\,\mathrm{eV}$, $T_\mathrm{i} \sim 100\,\mathrm{eV}$, $\bar{n}_\mathrm{e} \sim 1 \times 10^{19}\,\mathrm{m}^{-3}$, and $\tau_\mathrm{e} = 1.5\text{--}3\,\mathrm{ms}$ were routinely produced.

A more complete comparison is given in Table. 4.1. Besides EBW research, the improved plasma performance enabled exploration of new regime in experimental topics such as MHD activities like the internal reconnection event [144] and high harmonic fast wave physics [145] that were unreachable before.

The study of EBW was performed in two stages. In the first stage, low power EBW receiving experiments were carried out. A new instruments, named radio-reflectometer, was constructed. It is a stand-alone diagnostic that relies only on microwave techniques to estimate the electron temperature from the radiation intensity of EBW, and does not require assistance of other expensive diagnostics. Key points of the radio-reflectometer experiment are: [18, 146]

- Operation in the range of 5–16 GHz, corresponding to the measurement of the fundamental to the 3rd harmonic EBW emission.

- Measurement of the X-mode perpendicular emission.

- The core electron temperature of 200–300 eV and a monotonic T_e profile was obtained. The measured core T_e was consistent with the results of other diagnostics.

- A possibility of determining the MC efficiency from the reflectivity was shown.

In the second stage, EBW heating experiments were carried out. Encouraged by the promising results of the radio-reflectometer experiments, high power plasma heating experiments were performed in collaboration with the TRIAM-1M group at Kyushu university (TST-2@K). TST-2 was temporarily moved to Kyushu university, where 200 kW of microwave power at 8.2 GHz, which is one half of the lower hybrid current drive system of the TRIAM-1M supper conducting tokamak, was available. The same MC scenario, the perpendicular X-mode injection from the low magnetic field side, was employed. A local limiter similar to that used in CDX-U was used to control the density profile near the upper hybrid resonance layer and the density profile was measured by Langumuir probes installed inside the local limiter in order to evaluate the theoretical MC efficiency. This experiment provided the world's first demonstration of plasma heating by EBW on an ST plasma [20]. Main achievements are:

- fairly good antenna-plasma coupling was observed, and up to 140 kW of microwave power was injected successfully (the injected power was limited by the microwave generator, not by the plasma).

- A clear increase of the stored energy at RF turn-on is observed. In a high density discharge, a heating efficiency of over 50 % was achieved.

- A clear increase of X-ray radiation in the energy range of $h\nu \geq 1\,\text{keV}$ was observed, indicating high energy electron generation by the EBW.

- PIN diode array cameras showed that the increase in soft X-ray emission profile that occurred at RF turn-on was localized in the plasma core region.

- In lower density discharges, the heating efficiency was lower, indicating poorer MC efficiency. According to a 1-D full-wave calculation of MC, it is shown that the decrease of the MC efficiency can be explained by the radial stretch of the cutoff-resonance-cutoff triplet.

7.2 Future perspectives

This last section addresses perspectives for future research following the present work. Since the EBW has been attracting increasing attention both as a plasma physics research subject and as a promising tool, more research results are expected to be published in the coming decades. In research that requires a long term support from the fusion community such as EBW heating, experimental plans are often formulated many years before the experiments actually begins. Some of these plans are discussed in this discussion.

Before discussing what is likely to happen, what is necessary to happen should be mentioned. The author admits that follow-up experiments are necessary to make the results given in this thesis to develop into routine tools for diagnostic and heating. In the radio-reflectometer experiment, the analysis focused on a single time slice. This is mainly because TST-2 plasmas made at Hongo Campus were not sufficiently stationary, and suffered from a chain of IREs after the plasma current reached its peak level. In addition, equilibrium reconstruction was not so reliable at that time. It goes without saying that future receiving experiments must cover the whole time evolution of discharge. In the plasma heating experiment, heating was observed only in a high density discharge. Since the edge density is not controlled independently from the core density, such a discharge had high edge density that pushed the triplet into the shadow of the local limiter, resulting in a high MC efficiency. An independent control of the edge density must be demonstrated for EBW to be used as a reliable and widely used tool in fusion experiments.

An advantage of the electron temperature measurement based on EBW emission over other T_e diagnostics such as Thomson scattering and PHA is the possibility of achieving a very high temporal resolution. In fact, the ordinary electron cyclotron emission (ECE) [147] diagnostic is used to observe fast small-scale structures such as magnetic islands, transport barriers, and turbulent fluctuation. Unfortunately, all EBW emission measurements currently reported, including results from TST-2, CDX-U, MAST, and NSTX,

show large fluctuations. This is partly because MC takes place in the plasma edge region where the density is highly fluctuating. The reduction of such a noise is a difficult task. Hence, repetitive behaviors such as MHD mode activities are likely to be more suitable for observation by EBW emission.

Another extension of the EBW radiometer is to locate receiving antennas in an array in the poloidal cross section. According to ray-tracing calculations (Fig. 3.8), the emission measured off the mid-plane is expected to come from a radial location different from that measured on the midplane. In terms of reducing the bandwidth of the radiometer, off mid-plane receiving is beneficial. It may also be helpful to avoid certain frequency at which high power microwave is injected.

As for high power experiments, a demonstration of current drive is important. High power heating experiments are planned on NSTX and MAST. On MAST, proof-of-principle EBW heating experiments with the existing 60 GHz gyrotrons and EBW-assisted plasma start-up using a new 28 GHz system are planned. Initial results of such experiments are found in Ref. [148] On NSTX, an experiment using 28 GHz gyrotrons is currently considered [88].

As discussed in the introduction, an important application of EBW heating is plasma start-up. It is widely recognized that a fusion reactor based on the ST concept cannot have an OH solenoid, so the development of an alternative technique is essential. The advantage of plasma start-up by EBW includes production of a clean plasma, only a small number of in-vessel components, and no requirement for a special vacuum vessel structure such as for helicity injection. The goal of plasma start-up by EBW is the production of plasma with sufficient plasma current and density for further heating and current drive by neutral bean injection. Such a scenario has already been demonstrated on a conventional aspect ratio tokamak using the swing of the vertical field coil and LHCD [149]. Demonstration of such a scenario in ST is highly desired. So far, plasma currents achieved in STs by RF start-up are limited to the level of old RF tokamak experiments ($I_\mathrm{p} \sim 15\,\mathrm{kA}$ obtained in LATE is the highest I_p achieved in STs).After moving TST-2 back to the University of Tokyo, a small ST device, CPD, was constructed at Kyushu University, and the construction of another medium-sized ST, QUEST, is currently underway. These devices are suitable platforms for such experiments.

Next, possible improvements to TST-2, including magnets, power supplues, and diagnostics, are suggested, based on experience from TST-2 experiments at Hongo Campus and at Kyushu University (referred to as TST-2 and TST-2@K in this section). Benefits to EBW research are discussed in particular, but these improvements should be beneficial to a wide variety of physics experiments. TST-2 was moved to Kashiwa Campus of the Univer-

sity of Tokyo after completion of the TST-2@K experiment, and resumed operation recently. The total energy capability of capacitor banks has been increased significantly, taking advantage of the greatly improved space availability. The principal control scheme and diagnostic sets are quite similar to those used at Hongo campus.

In TST-2@K experiments, a toroidal field of 0.28 T and an OH solenoid flux swing of 120 mVs (single swing operation) were achieved. These are near the maximum ratings. TST-2@K used a very different set of power supplies which enabled feed back control of the plasma position, which is of great importance in RF experiments. The limiter edge density, to which the EBW MC efficiency was found to be sensitive, can be optimized by controlling the distance between the local limiter and the outer most flux surface. It may also useful for controlling parametric instabilities in HHFW experiments which are reported to depend strongly on the plasma-antenna distance. The power supply used for horizontal position control on TST-2@K had the pulse width modulation (PWM) frequency of 3 kHz, which enabled control of the plasma position by adjusting the feed back reference position, as shown in Fig. 6.7. The position control of TST-2 should be possible by the existing power supply which consists of a capacitor bank and an IGBT chopper switch operated at 5 kHz. Feed back control of the vertical position was also demonstrated on TST-2@K using a low cost RT (real time) Linux computer. On TST-2@K, the horizontal and vertical control were independently carried out by two different computers. It is preferable to integrate these to a single RT Linux system. Another difference between TST-2 and TST-2@K is the I_p ramp-up rate. The ramp-up rate of TST-2 plasmas with $I_\mathrm{p} \sim 100$ kA was typically 15 – 20 MA/s, while it was ~ 10,MA/s on TST-2@K. On TST-2, MHD activities that caused I_p saturation were sometimes observed, and IREs occured around the peak of I_p. A slower ramp-up rate might be preferable to suppress such activities. A slower ramp-up rate is also preferable from the view point of plasma position control, since it reduces power supply requirements for equilibrium field coils.

The following enhancements of diagnostic capability should be helpful, too. Equilibrium reconstruction provided the most convincing evidence of plasma heating and the evaluation of the heating efficiency. However, reconstruction is currently restricted to a period after the plasma current has ramped up sufficiently. Reconstruction of the very beginning of the discharges did not give successful results, probably because the internal inductance is extremely small during the early phase of the discharge. Plasmas with such low internal inductances have a hollow current profile, which cannot be represented well by polynomial functions used in the present analysis. The modeling of start-up plasmas is not well established, but considering the

importance of start-up research in ST, a reconstruction technique suitable for the start-up phase should be developed.

In order to improve the reliability of T_e measurement by EBW emission, further comparisons with direct measurements of T_e are necessary. The most suitable diagnostic for such a purpose is Thomson scattering, which measures the electron temperature and density from Doppler broadening and the total number of scattered photons, respectively. Although Thomson scattering cannot measure continuous temporal evolution, it has a clear advantage over T_e measurement by soft X-ray emission or EBW emission. Soft X-ray emission measurements have difficulty in isolating the contribution of impurity line emission, and EBW emission has uncertainty in the MC efficiency. Hence, an ideal T_e measurement will use Thomson scattering as an absolutely calibrated T_e reference and the temporal evolution is obtained from EBW emission and edge density profile.

TST-2 presently uses a 100 GHz microwave interferometer and a 50 GHz amplitude-modulation (AM) interferometer. The upper limit of measurable range of density is 1–2×10^{19} m^{-3}. AM interferometer was developed to overcome the disadvantages of a standard interferometer using a relatively low frequency microwave source. In fact, it is reported that the highest density measurable by the 50 GHz AM interferometer is comparative to the standard 100 GHz interferometer in Ref. [150]. However, positive results were not obtained when the same technique was tested using a 100 GHz source on TST-2, Improvement towards such direction is desired since the measurement of densities beyond the above limit are sometimes required. For example, the absorption of HHFW is predicted be better at higher density, and correspondingly, higher beta. In addition, a density scan over a wide range will change the edge density profile greatly, providing a further test of the EBW radiometer.

It goes without saying that any experimental schedule should be determined considering various aspects, including funding and manpower, and a suitable modification depends on the planned research. The improvements suggested here may not be realized so easily. In the final part of this section, a specific phenomenon is introduced to point out the possibility that TST-2 can make a great contribution using the EBW radiometer and improvements mentioned above.

The possibility of high temporal resolution and observation of MHD mode activity by EBW emission was noted above. In TST-2, a possible target of such research is already identified. Figure 7.1 shows the soft X-ray emission profile measured by the mid-plane PIN diode camera. Two distinct repetitive activities during the periods denoted by (A) and (B) are noted. During period (A), central chords show repetitions of abrupt drop and gradual recovery.

Figure 7.2 shows an expanded view comparing signals from different channels, from central to peripheral sight-lines. Peripheral chords show increases of emission coincident with abrupt drops in the central chord. Interestingly, as denotes by the arrows, the channel that shows the most increase moves gradually to outer channels. For example, channel 7 initially shows increases at core drops, but later on the behavior resembles that of the central channel. During period (B), a different kind of mode activity with a frequency of 10 kHz is observed. Using the measurements from other PIN diode cameras and magnetics, this mode was confirmed to have the $m/n = 1/1$ structure. It is also known from equilibrium analysis that the central safety factor becomes nearly one. This 10 kHz mode continues to exist till a large fraction of the stored energy is lost by the internal reconnection events at 37 ms. The
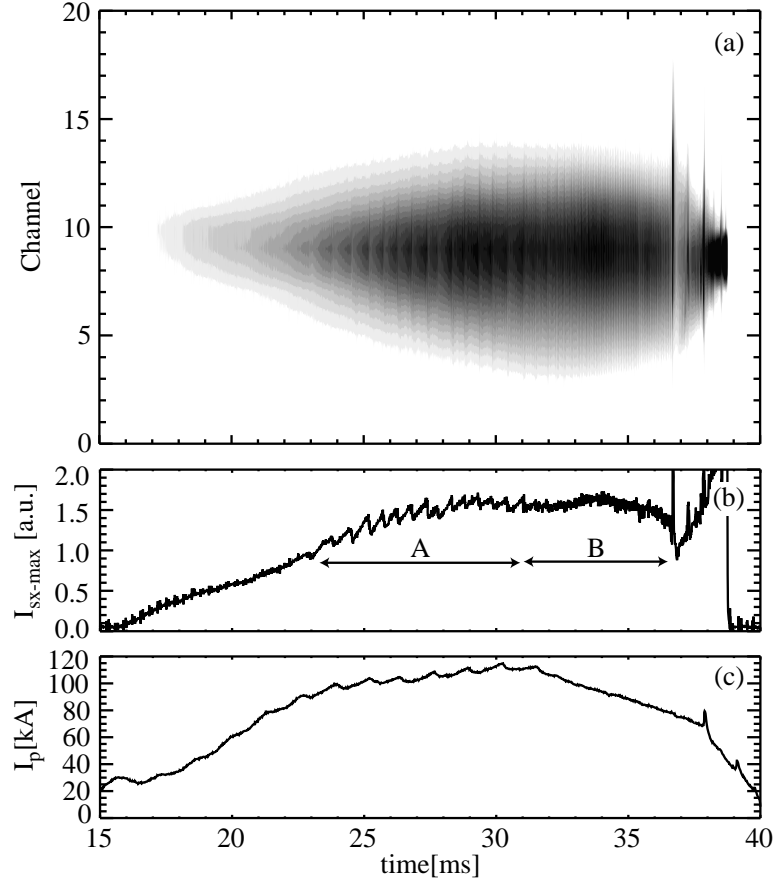

Figure 7.1: (a) Contour plot of SX emission (a), and evolutions of (b) the peak intensity and (c) the plasma current in #303432.
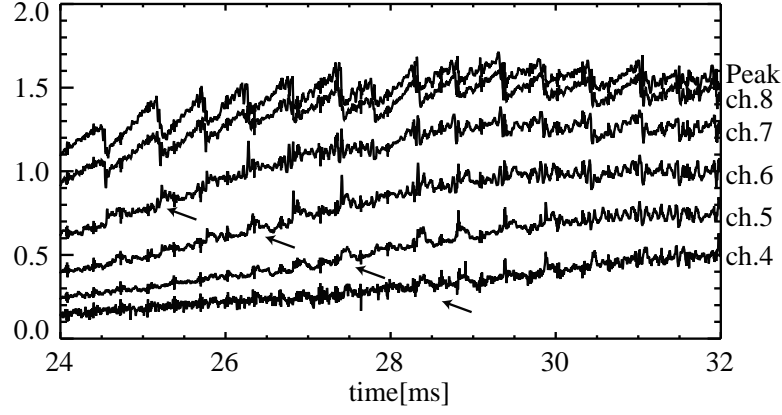
Figure 7.2: Expanded view comparing signals from different channels of the mid-plane PIN diode camera, from central to peripheral sight-lines. The signal denoted as peak corresponds to the peak of intensity in the emission profile. The arrows denote increases corresponding to core signal drops.

result of analysis of SX emission during period (B) is reported in Ref. [144]. Compared to the X-ray emission measurement, a change of blackbody emission in the electron cyclotron frequency range is directly interpreted as a change in T_e. Therefore, an EBW radiometer will certainly contribute to understanding of such phenomena.

Bibliography

[1] Y-K. M. Peng and D J Strickler, "Feastures of spherical torus plasmas", Nucl. Fusion **26**, 769 (1986).

[2] I. B. Bernstein, "Waves in a Plasma in a Magnetic Field", Phys. Rev. **109**, 10 (1958).

[3] M. Ono, "High harmonic fast waves in high beta plasmas", Phys. Plasmas **2**, 4075 (1995).

[4] A. E. Costley et al., "Electron cyclotron emission from a tokamak plasma: experiment and theory", Phys. Rev. Lett. **33**, 758 (1974).

[5] V. V. Alikaev et al., *in Proc. of 10th Int. Conf. on Plasma Phys. and Controlled Nuclear Fusion Res.*, London, (1984) vol. 1, p. 419.

[6] D. F. H. Start et al., "Observation of a plasma current driven by rf waves at the electron cyclotron resonance in the Culham Levitron", Phys. Rev. Lett. **48**, 624 (1982).

[7] V. Shevchenko et al., "Generation of noninductive current by electron-Bernstein waves on the COMPASS-D tokamak", Phys. Rev. Lett. **89**, 265005 (2002).

[8] T. Maekawa et al., "Doppler-shifted cyclotron absorption of electron Bernstein waves via $N_\parallel$-Upshift in a tokamak plasma", Phys. Rev. Lett. **86**, 003783 (2001).

[9] H. P. Laqua et al., "Electron-Bernstein-Wave current drive in an overdense plasma at the Wendelstein 7-AS stellarator", Phys. Rev. Lett. **90**, 075003 (2003).

[10] H. P. Laqua et al., "Electron Bernstein wave emission from an overdense plasma at the W7-AS stellarator", Phys. Rev. Lett. **81**, 2060 (1998).

[11] P. C. Efthimion et al., "New electron cyclotron emission diagnostic for measurement of temperature based upon the electron Bernstein wave", Rev. Sci. Instrum. **70**, 1018 (1999).

[12] S. Nakajima and H. Abe, "Mode-conversion process and overdense-plasma heating in the electron cyclotron range of frequencies", Phys. Rev. A **38**, 4373 (1988).

[13] H. Sugai, "Mode conversion and local heating below the second electron cyclotron harmonics", Phys. Rev. Lett. **47**, 1899 (1981).

[14] A. K. Ram, A. Bers, S. D. Schultz, and V. Fuchs, "Mode conversion of fast Alfvèn waves at the ion-ion hybrid resonance", Phys. Plasmas **3**, 1976 (1996).

[15] K. Hanada et al., "Low aspect ratio tokamak experiment in university of tokyo", Transactions of Fusion Technology **27**, 440 (1995).

[16] S. Shiraiwa et al., "Construction, operational scenarios, and research plan of TST-2", *in Proc. of 26th EPS Conf. on Contr. Fusion and Plasma Physics*, Maastricht, (1999), ECA vol. 23J, p. 441.

[17] Y. Takase et al., "Initial results from the TST-2 spherical tokamak", Nucl. Fusion **41**, 1543 (2001).

[18] S. Shiraiwa et al., "Electron Bernstein wave emission diagnostic assisted by reflectometry on TST-2 spherical tokamak", Rev. Sci. Instrum. **74**, 1453 (2003).

[19] B. Jones et al., "Controlled optimization of mode conversion from electron Bernstein waves to extraordinary mode in magnetized plasma", Phys. Rev. Lett. **90**, 165001 (2003).

[20] S. Shiraiwa et al., "Heating by an electron Bernstein wave in a spherical tokamak plasma via mode conversion", Phys. Rev. Lett. **96**, 185003 (2006).

[21] S. Shiraiwa et al., "Evidence of electron Bernstein wave heating on the TST-2 spherical tokamak", J. Plasma Fusion Res. **81**, 3 (2005).

[22] J. Wesson, *Tokamaks*, Oxford University Press., Walton street, Oxford, (1987).

[23] Z. Chang et al., "Observation of nonlinear neoclassical pressure-gradient–driven tearing modes in TFTR", Phys. Rev. Lett. **74**, 4663 (1995).

[24] S. A. Sabbagh et al., "Resistive wall stabilized operation in rotating high beta NSTX plasmas", Nucl. Fusion **46**, 635 (2006).

[25] F. Troyon, R. Gruber, H. Saurenmann, S. Semenzato, and S. Succi, "MHD-limits to plasma confinement", Plasma Phys. Controlled Fusion **26**, 209 (1984).

[26] E. J. Strait et al., "Wall stabilization of high beta tokamak discharges in DIII-D", prl **74**, 2483 (1995).

[27] S.M. Kaye et al., "Progress towards high performance plasmas in the National Spherical Torus Experiment (NSTX)", Nucl. Fusion **45**, S168 (2005).

[28] A. A. Galeev and R. Z. Sagdeev, "Transport phenomena in a collisionless plasma in a toroidal magnetic system", Sov. Phys. JETP **26**, 233 (1967).

[29] P. H. Rutherford, "Collisional diffusion in an axisymmetic torus", Phys. Fluids **13**, 482 (1970).

[30] B. B. Kadomtsev, *Plasma turbulence*, Academic Press, London, (1965).

[31] F. Wagner et al., "Regime of improved confinement and high beta in neutral-beam-heated divertor discharges of the ASDEX tokamak", Phys. Rev. Lett. **49**, 1408 (1982).

[32] Y. Koide et al., "Internal transport barrier on q=3 surface and poloidal plasma spin up in JT-60U high-p discharges", Phys. Rev. Lett. **72**, 3662 (1994).

[33] K. H. Burrell, "Effects of E × B velocity shear and magnetic shear on turbulence and transport in magnetic confinement devices", Phys. Plasmas **4**, 1449 (1997).

[34] H. Shirai, "Recent experimental and analytic progress in the Japan Atomic Energy Research Institute Tokamak-60 Upgrade with W-shaped divertor configuration", Phys. Plasmas **5**, 1712 (1998).

[35] S.M. Kaye et al., "ITER L mode confinement database", Nucl. Fusion **37**, 1303 (1997).

[36] ITER Physics Expert Group on Confinement, ITER Physics Expert Group on Confinement Modelling Transport, Database, and ITER Physics Basis Editors, "Chapter 2: Plasma confinement and transport", Nucl. Fusion **39**, 2175 (1999).

[37] M. C. Zarnstorff et al., "Bootstrap current in TFTR", Phys. Rev. Lett. **60**, 1306 (1988).

[38] A. C. Darke et al., "MAST: A mega amp spherical tokamak", Fusion Technol. **1**, 799 (1995).

[39] M. Ono et al., "Exploration of spherical torus physics in the NSTX device", Nucl. Fusion **40**, 557 (2000).

[40] J. A. Holmes et al., "Maximum beta for a small-aspcet-ratio tokamak", Phys. Fluids B **1**, 358 (1989).

[41] G. Rewoldt et al., "Microinstability properties of small-aspect-ratio tokamaks", Phys. Plasmas **3**, 1667 (1996).

[42] M. Gryaznevich et al., "Achievement of record β in the START spherical tokamak", Phys. Rev. Lett. **80**, 3972 (1998).

[43] Kardaun et al., *in ITER Confinement Workshop*, NJ, (1998), Plasma Physics Lab., Princeton Univ.

[44] A. Sykes et al., "The spherical tokamak programme at Culham", Nucl. Fusion **39**, 1271 (1999).

[45] J. E. Menard et al., "Ideal MHD stability limits of low aspect ratio tokamak plasmas", Nucl. Fusion **37**, 595 (1997).

[46] M . Ono, "Ion bernstein wave heating experiments", Phys. Fluids B **5**, 241 (1993).

[47] D. Stutman et al., "Spectroscopic evidence for high harmonic fast wave heating in the CDX-U spherical torus", Plasma Phys. Controlled Fusion **41**, 867 (1999).

[48] A. Sykes et al., "First results from the START experiment", Nucl. Fusion **32**, 694 (1992).

[49] Y. Ono and M. Inomoto, "Ultra-high-beta spherical tokamak formation by use of an oblate field-reversed configuration", Phys. Plasmas **7**, 1863 (2000).

[50] T. H. Jensen and M. S. Chu, "Current drive and helicity injection", Phys. Fluids **27**, 2881 (1984).

[51] B. A. Nelson et al., "Formation and sustainment of a 150 kA tokamak by coaxial helicity injection", Phys. Rev. Lett. **72**, 3666 (1994).

[52] O. Mitarai, "Inductive plasma current start-up by the outer vertical field coil in a spherical tokamak", Plasma Phys. Controlled Fusion **41**, 1469 (1999).

[53] S Kubo et al., "Toroidal plasma current startup and sustainment by rf in the WT-2 tokamak", Phys. Rev. Lett. **50**, 1994 (1983).

[54] K Toi et al., "Startup and quasistationary drive of plasma current by lower hybrid waves in a tokamak", Phys. Rev. Lett. **52**, 2144 (1984).

[55] F Jobes et al., "Formation of a 100-kA tokamak discharge in the Princeton Large Torus by lower hybrid waves", Phys. Rev. Lett. **52**, 1005 (1984).

[56] K Ogura et al., "Toroidal plasma current startup and sustainment by lower hybrid waves in the WT-3 tokamak", Nucl. Fusion **30**, 611 (1990).

[57] C. B. Forest, Y. S. Hwang, M. Ono, and D. S. Darrow, "Internally generated currents in a small-aspect-ratio tokamak geometry", Phys. Rev. Lett. **68**, 3559 (1992).

[58] T. Yoshinaga et al., "Spontaneous formation of closed-field torus equilibrium via current jump observed in an electron-cyclotron-heated plasma", Phys. Rev. Lett. **96**, 125005 (2006).

[59] V. K. Gusev et al., "Plasma formation and first OH experiments in the Globus-M tokamak", Nucl. Fusion **41**, 919 (2001).

[60] M. Nagata et al., "Self-reversal phenomena of toroidal current by reversing the external toroidal field in Helicity-driven toroidal plasmas", Phys. Rev. Lett. **90**, 225001 (2003).

[61] T. Maekawa et al., "Formation of spherical tokamak equilibria by ECH in the LATE device", Nucl. Fusion **45**, 1439 (2005).

[62] G. D. Garstka et al., "The upgraded Pegasus Toroidal Experiment", Nucl. Fusion **46**, S603 (2006).

[63] W. H. Wang et al., "Edge plasma electrostatic fluctuation and anomalous transport characteristics in the Sino-united spherical tokamak", Plasma Phys. Controlled Fusion **47**, 1 (2005).

[64] Y. One et al., "Spontaneous and artificial generation of sheared-flow in oblate FRCs in TS-3 and 4 FRC Experiments", Nucl. Fusion **43**, 649 (2003).

[65] Y. Takase et al., "Plasma current start-up experiments without the central solenoid in the TST-2 spherical tokamak", Nucl. Fusion **46**, S598 (2006).

[66] S. A. Sabbagh et al., "Beta-limiting instabilities and global modes stabilization in the National Spherical Torus Experiment", Phys. Plasmas **9**, 2085 (2002).

[67] J. R. Wilson et al., "Exploration of high harmonic fast wave heating on the National Spherical Torus Experimen", Phys. Plasmas **10**, 1733 (2003).

[68] T. M. Biewer et al., "Edge ion heating by launched high harmonic fast waves in the National Spherical Torus Experiment", Phys. Plasmas **12**, 056108 (2005).

[69] G. D. Garstka et al., "Performance and stability of near-unity aspect ratio plasmas in the Pegasus Toroidal Experiment", Phys. Plasmas **10**, 1705 (2003).

[70] H. Toyama et al., "Helicity injection experiments and turbulence measurements on the Tokyo Spherical Tokamak", *in Proc. of 16th IAEA Fusion Energy Conference*, Montreal, (1996) vol. 2, p. 223.

[71] T. R. Jarboe et al., "Results from current drive experiments on the Helicity Injected Torus", Phys. Plasmas **5**, 1807 (1998).

[72] R. Raman et al., "Demonstration of plasma startup by coaxial helicity injection", Phys. Rev. Lett. **90**, 075005 (2003).

[73] E. Kawamori et al., "Ion kinetic effect on bifurcated relaxation to a field-reversed configuration in TS-4 CT experiment", Nucl. Fusion **45**, 843 (2005).

[74] O. N. Shcherbinin et al., "Numerical modelling and experimental study of ICR heating in the spherical tokamak Globus-M", Nucl. Fusion **46**, S592 (2006).

[75] R. Majeski et al., "Enhanced Energy Confinement and Performance in a Low-Recycling Tokamak", Phys. Rev. Lett. **97**, 075002 (2006).

[76] R. Majeski et al., "Status of the Lithium Tokamak eXperiment (LTX)", *in Proc. of 48th Annual Meeting of the Division of Plasma Physics*, Philadelphia, (2006).

[77] Y. M. Peng, "Progress toward Fusion Component Test Facility (CTF), an integrated test facility", *in Proc. of 12th International ST Workshop*, Chengdu, PRC, (2006).

[78] T. H. Stix, *Waves in Plasmas*, Springer-Verlag New York inc., 175 Fifth Avenue, New York, NY 10010, (1992).

[79] K. G. Budden, *Radio Waves in the Ionosphere*, Cambridge Univ. Press, Cambridge, U.K., (1966).

[80] E. Lazzaro et al., "Relativistic dispersion relation for electron Bernsten waves", Phys. Fluids **23**, 2330 (1980).

[81] V. Shevchenko et al., "EBW Experiments on MAST", *in Proc. of 12th International ST Workshop*, Chengdu, PRC, (2006).

[82] J. Preinhaelter and V. Kopeckỳ, "Penetration of high-frequency waves into a weakly inhomogeneous magnetized plasma at oblique incidence and their trasnformation to Bernstein modes", J. Plasma Phys. **10**, 1 (1973).

[83] R. B. White, *The theory of toroidally confined plasmas*, Imperial college press, 2001, ch. 9.

[84] H. P. Laqua et al., "Resonant and nonresonant electron cyclotron heating at densities above the plasma cutoff by O-X-B mode conversion at the W7-AS stellarator", Phys. Rev. Lett. **78**, 3467 (1997).

[85] R. A. Cairns et al., "The prospects for electron Bernstein wave heating of spherical tokamaks", Phys. Plasmas **7**, 4126 (2000).

[86] B. Jones et al., "Measurement of the magnetic field in a spherical torus plasma via electron Bernstein wave emission harmonic overlap", Phys. Plasmas **11**, 1028 (2004).

[87] R. J. Akers et al., "L-H transition in the Mega-Amp Spherical Tokamak", Phys. Rev. Lett. **88**, 035002 (2002).

[88] G. Taylor et al., "Efficient coupling of thermal electron Bernstein waves to the ordinary electromagnetic mode on the National Spherical Torus Experiment", Phys. Plasmas **12**, 052511 (2005).

[89] S. J. Diem et al., "Electron Bernstein wave mode conversion physics on NSTX", *in Workshops on Physics and Technology of RF Heating of Fusion Plasmas 2006*, Nara, (2006).

[90] H. P. Laqua et al., "Electron Bernstein wave heating and emission via the OXB process at W7-AS", Plasma Phys. Controlled Fusion **41**, A273 (1999).

[91] C. B. Forest et al., "Off-midplane launch of electron Bernstein waves for current drive in overdense plasmas", Phys. Plasmas **7**, 1352 (2000).

[92] P. K. Chattopadhyay et al., "Electron Bernstein wave emission from an overdense reversed field pinch plasma", Phys. Plasmas **9**, 752 (2002).

[93] J. K. Anderson et al., "Electron Bernstein wave experiments in the MST reversed field pinch", *in Radio frequency power in plasmas, C. B. Forest, ed.*, New York, (2003), AIP p. 341.

[94] M. Cengher et al., "Coupling to the electron Bernstein wave using a phased array of waveguides in MST reversed field pinch", Nucl. Fusion **46**, 521 (2006).

[95] J. K. Anderson et al., "EBW experiments in the Madison Symmetric Torus", *in Radio frequency power in plasmas, S. J. Wukitch and P. T.Bonoli, eds.*, New York, (2005), AIP p. 341.

[96] A. K. Ram and S. D. Schultz, "Excitation, propagation, and damping of electron Bernstein waves in tokamaks", Phys. Plasmas **7**, 4084 (2000).

[97] H. Igami et al., "A survey of mode-conversion transparency windows between external electromagnetic waves and electron Bernstein waves for various plasma slab boundaries", Plasma Phys. Controlled Fusion **46**, 261 (2004).

[98] R. I. Pinsker et al., "Calculation of direct coupling to the electron Bernstein wave with a waveguide antenna", Tech. Rep. GA-A23752, GA, 2001.

[99] R. I. Pinsker et al., "Calculation of coupling to the electron Bernstein wave with a phased waveguide array", Plasma Phys. Controlled Fusion **47**, 335 (2005).

[100] A. D. Piliya et al., "Electron Bernstein waves in a shperical toka-mak with a magnetic well", Plasma Phys. Controlled Fusion **47**, 2029 (2005).

[101] J. Decker and A. K. Ram, "Relativistic description of electron Bern-stein waves", Phys. Plasmas **13**, 112503 (2006).

[102] A. D. Piliya et al., "Electron Bernstein wave in the mid-plane region pf a sphercial tokamak", Plasma Phys. Controlled Fusion **2005**, 379 (47).

[103] A. N. Saveliev, "Approximate relativistic dispersion relation for elec-tron Bernstein waves in a Maxwellian plasma", Plasma Phys. Con-trolled Fusion **47**, 2003 (2005).

[104] S. C. Jardin, "Dynamic modeling of transport and positional control of tokamaks", Journal of Computational Physics **66**, 481 (1986).

[105] C. E. Kessel et al., "Long pulse high performance plasma scenario devel-opment for the National Spherical Torus Experiment", Phys. Plasmas **13**, 56108 (2006).

[106] T. Haruki and J. I. Sakai, "Electromagnetic wave emission from a dy-namic current sheed with pinching and the coalescence of magnetic islands in solar flare plasmas", The Astrophysical Journal **552**, L175 (2001).

[107] B. Thidé, H. Kopka, and P. Stubbe, "Observations of stimulated scat-tering of a strong high-frequency radio wave in the ionosphere", Phys. Rev. Lett. **49**, 1561 (1982).

[108] P. Stubbe and H. Kopka, "Stimulated electromagnetic emission in a magnetized plasma: a new symmetric spectral feature", Phys. Rev. Lett. **65**, 183 (1990).

[109] T. B. Leyser et al., "Stimulated electromagnetic emission near elec-tron cyclotron harmonics in the ionosphere", Phys. Rev. Lett. **63**, 1145 (1989).

[110] S. P. Kuo, "Parametric excitation of electromagnetic waves by electron Bernstein waves", Phys. Fluids B **4**, 4094 (1992).

[111] S. P. Kuo, "Parametric instability producing broad symmetric struc-ture in the spectrum of ionospheric heating-induced radiation", Phys. Plasmas **4**, 3194 (1997).

[112] H. L. Zhou, J. Huang, and S. P. Kuo, "Cascading of the upper hybrid/electron Bernstein wave in ionospheric heating experiments", Phys. Plasmas **1**, 3044 (1994).

[113] S. Ejima et al., "Volt-second consumption in Double III plasmas", Nucl. Fusion **22**, 1313 (1982).

[114] S. P. Hirshman and G. H. Neilson, "External inductance of an axisymmetric plasma", Phys. Fluids **29**, 790 (1986).

[115] T. G. Jones, *Low-aspect-ratio tokamak start-up and operational current limit in CDX-U*, PhD thesis, Princeto University, (1995).

[116] H. Totsuka, "Design and construction of the TST spherical tokamak", Master's thesis, Faculty of Science, University of Tokyo, (1995). [in Japanese].

[117] "16-bit MCUs & DSCs", in http://www.microchip.com/, MICROCHIP TECHNOLOGY INC.

[118] I. H. Hutchinson, *Principles of plasma diagnostics*, Cambridge Univ. Press, Cambridge, U.K., 1987, ch. 2, 10.

[119] D. W. Swain and G. H. Neison, "An efficient technique for magnetic analysis of non-circular, high-beta tokamak equilibria", Nucl. Fusion **8**, 1015 (1982).

[120] L. L. Lao et al., "Sepation of $\bar{\beta}_\mathrm{p}$ and ℓ_i in tokamaks of non-circular cross-section", Nucl. Fusion **25**, 1421 (1985).

[121] M. Abe et al., "Magnetic analysis of ohmic discharges in the superconducting tokamak TRIAM-1M", Nucl. Fusion **36**, 405 (1996).

[122] F. Hofmann and G. Tonetti, "Fast identification of plasma boundary and X-points in elongated tokamaks", Nucl. Fusion **28**, 519 (1988).

[123] Yu. K. Kuznetsov et al., "Plasma boundary determination in ITER by the optimized current filament method", Nucl. Fusion **38**, 182 (1998).

[124] O. Mitarai et al., "Plasma current start-up by ECW and vertical field in the TST-2 spherical tokamak", J. Plasma Fusion Res. **80**, 549 (2004).

[125] V. D. Shafranov, "The theory of hydromagnetic stability of toroidal plasma configurations", Sov. Phys. JETP **26**, 400 (1968).

[126] H. Grad and H. Rubin, "Hydromagnetic equilibrium and force-free fields", *in United Nations Conference on the Peacefull Uses of Atomic Energy*, Geneva, (1958) vol. 31, p. 190.

[127] B. J. Akers et al., "Neutral beam heating in the START spherical tokamak", Nucl. Fusion **42**, 122 (2002).

[128] J. L. Johnson et al., "Numerical determination of axisymmetric toroidal magnetohydrodynamic equilibria", Journal of Computational Physics **32**, 212 (1979).

[129] B. J. Braams et al., "Magnetohydrodynamic equilibrium calculations using multigrid", Tech. Rep. IPP 5/6, Max-Planck-Institute for Plasma Physics, 1985.

[130] L. L. Lao et al., "Reconstruction of current profile parameters and plasma shape in tokamaks", Nucl. Fusion **25**, 1611 (1985).

[131] T. Takeda and S. Tokuda, "Computation of MHD equilibrium of tokamak plasmas", Journal of Computational Physics **93**, 1 (1991).

[132] H. Mott-Smith and I. Langmuir, "The theory of collectors in gaseous discharges", Phys. Rev. **28**, 727 (1926).

[133] C. M. Celata and D. A. Boyd, "Cyclotron radiation as a diagnostic tool for tokamak plasmas", Nucl. Fusion **17**, 735 (1977).

[134] F. Engelmann and M. Curatolo, "Cyclotron radiation from a rarefied inhomogeneous magnetoplasma", Nucl. Fusion **13**, 497 (1973).

[135] R. H. Dicke, "The measurement of thermal radiation at microwave frequencies", Rev. Sci. Instrum. **17**, 268 (1946).

[136] D. Iijima, "The study of the soft X-ray emission spectrum on the TST-2 spherical tokamak", Master's thesis, Graduate School of Frontier Sciences, the University of Tokyo, (2003). [in Japanese].

[137] "UV Photodiodes, UV Detectors, Vacuum Ultravaiolet Detectors", in http://www.ird-inc.com/axuv.html, International Radiation Detectors inc.

[138] R. L. Boivin et al., "High resolution bolometry on the Alcator C-Mod tokamak", Rev. Sci. Instrum. **70**, 260 (1999).

[139] D. S. Gray et al., "Time resolved radiated power during tokamak disruptions and spectral averaging of AXUV photodiode response in DIII-D", Rev. Sci. Instrum. **75**, 376 (2004).

[140] C. Suzuk et al., "Measurement of impurity emission profiles in CHS Plasma using AXUV photodiode arrays and VUV bandpass filters", Rev. Sci. Instrum. **75**, 4142 (2004).

[141] Y. Shimazu, *Experimental study of fluctuations on soft X-ray emission and magnetic field in the REPUTE-1 reversed field pinch plasma*, PhD thesis, Department of Physics, Faculty of Science, University of Tokyo, (1980?).

[142] E. Ishiyama, "Study of plasma radiation on TST spherical tokamak", Master's thesis, Department of Physics, Faculty of Science, University of Tokyo, (1996). [in Japanese].

[143] S. Duorah, *Soft X-ray spectroscopy using a multi layer mirror on the Compact Helical Device*, PhD thesis, Department of Physics, Faculty of Science, University of Tokyo, (2000).

[144] K. Sasaki et al., "Soft X-ray measurement in IRE on the TST-2 spherical tokamak", *in Proc. of 33rd EPS Conf. on Contr. Fusion and Plasma Physics*, Roma, Italy, (2006), ECA.

[145] H. Kasahara, *Electron heating experiments using the high harmonic fast wave in high dielectric constant plasmas*, PhD thesis, Faculty of Frontier Sciences, University of Tokyo, (2006).

[146] S. Shiraiwa et al., "Study of electron Bernstein wave emission on TST-2", J. Plasma and Fusion Res. SERIES **5**, 189 (2002).

[147] V. S. Udintsev et al., "New ECE diagnostics for the TEXTOR-94 tokamak", Rev. Sci. Instrum. **72**, 359 (2001).

[148] V. Shevchenko et al., "Electron Bernstein Wave Heating Experiments on MAST", *in Proc. of 21th IAEA Fusion Energy Conference*, Chengdu, (2006). EX/P6-22.

[149] S. Shiraiwa et al., "Formation of advanced tokamak plasmas without the use of an Ohmic-heating solenoid", Phys. Rev. Lett. **92**, 035001 (2004).

[150] T. Yamada et al., "Application of differential phase method to interferometry". to be published in Rev. Sci. Instrum.